Modeling upper ocean dynamics in the Southern Ocean:

Interaction of physics and biogeochemistry

By

Xiujun (Wendy) Wang

Submitted in fulfilment of the requirement for
the Degree of Doctor of Philosophy

Antarctic CRC and the Institute of Antarctic and Southern Ocean Studies
University of Tasmania

January, 2002

For my children: Nicholas, Caterina and Tatiana

Declaration

This is to certify that the material composing this thesis has never been accepted for any other degree or award in any tertiary institution and, to best of my knowledge and belief, is solely the work of the author, and contains no material previously published or written by another person, except where reference is made in the text.

Xiujun (Wendy) Wang

Authority of Access

This thesis may be made available for loan and limited copying in accordance with the Copyright Act 1968.

Xiujun (Wendy) Wang

Acknowledgements

I would like to acknowledge the following people for their help in this study:

Dr. Tom Trull (supervisor), for his time and effort in helping me to collect all the information needed for the modeling work, for his scientific inputs and encouragement over the past three years.

Dr. Richard Matear (research supervisor), for his time in providing me all kinds of support, and for his encouragement in discussing about science.

Prof. Bill Budd (associated supervisor), for his time and effort in helping me to finish this project.

Dr. Steve Rintoul, for his discussions and comments on some of the study.

Dr. Xingren Wu (my husband), for his support and encouragement over the past three years.

The NCEP Reanalysis data were provided by the NOAA-CIRES Climate Diagnostics Center, Boulder, Colorado, from their Web site at http://www.cdc.noaa.gov. The SeaWiFS *Chl a* data were provided by NASA at http://SeaWiFS.gsfc.nasa.gov/SEAWIFS.html and the Hobart local receiving station (John Parslow and Chris Rathbone, CSIRO). The XBT data from the ongoing Australia/French/USA collaboration repeat section were provided by Steve Rintoul and Ann Gronell.

Table of Contents

Table of Acronyms

AABW	Antarctic Bottom Water
AAIW	Antarctic Intermediate Water
ACC	Antarctic Circumpolar Current
AZ	Antarctic Zone
CZ	Continental Zone
DIC	Dissolved inorganic carbon
DOC	Dissolved organic carbon
DOM	Dissolved organic material
DON	Dissolved organic nitrogen
DOP	Dissolved organic phosphate
IPFZ	Inter-Polar Frontal Zone
LCDW	Lower Circumpolar Deep Water
MLD	Mixed layer depth
PF	Polar Front
PFZ	Polar Frontal Zone
POC	Particulate organic carbon
POM	Particulate organic material
PON	Particulate organic nitrogen
POP	Particulate organic phosphate
SACCF	Southern ACC Front
SAF	Subantarctic Front
SAMW	Subantarctic Mode Water
SAZ	Subantarctic Zone
SST	Sea surface temperature
STF	Subtropical Front
UCDW	Upper Circumpolar Deep Water

Abstract

A one-dimensional biophysical model was developed to simulate upper ocean dynamics and seasonal nutrient (N, P, Si) export from the euphotic zone to the depths in the Southern Ocean. Simulations were made in the Subantarctic Zone (SAZ) and the Polar Frontal Zone (PFZ). The physical part of model was forced with the heat fluxes, freshwater fluxes and wind stresses provided by the National Centers for Environmental Prediction. In both the SAZ and PFZ, the model was capable of reproducing the amplitude of the seasonal sea surface temperature (SST) and the seasonality of the mixed layer depth (MLD). The MLD was deepest in August-October (600 m in the SAZ, 160 m in the PFZ) and shallowest in January-Februry (20m in the SAZ, 35m in the PFZ). The shallower summer MLD in the SAZ was due to lower wind stress. However, the shallower winter MLD in the PFZ was due to strong stratification in the water below the mixed layer.

The biological component of the model used incident light, temperature, nutrient availability and estimates of phytoplankton biomass from satellite data recorded by the Sea-viewing Wide Field-of-view Sensor to determine production. The model was tuned to reproduce the observed seasonal cycle of nutrients. A series of sensitivity studies, taking into account uncertainties in both physical fields and biological formulations, led to several robust conclusions. The simulated annual export production was significantly higher in the PFZ (~65 mol P m^{-2}) than in the SAZ (~55 mol P m^{-2}) despite the PFZ having lower seasonal nutrient depletion in the euphotic zone. The higher export production in the PFZ was accomplished by

having larger resupply of phosphate to the upper ocean during the September to March period (27 – 37 mol P m^{-2}) than in the SAZ (8 – 15 mol P m^{-2}).

In the PFZ, it was assumed that nutrient utilization ratio followed the Redfield ratio in the non-diatoms and the N/P/Si utilization ratios were determined in the diatoms in a steady state ocean. The estimated annual export production is ~65 mmol P m^{-2}, ~820 mmol N m^{-2} and 1826 mmol Si m^{-2} in the euphotic zone for phosphate, nitrate and silicate respectively. The diatoms contribute 85% and 80% of the annual phosphate and nitrate export production. In the euphotic zone, the annual N/P utilization ratio is 11.5 – 12.9 in the diatoms and 12.1 – 13.6 in the community. The seasonal Si/N utilization ratio is 3 – 6 in the diatoms and 1 – 4 in the community, with the lowest found in the late summer. The annual Si/N utilization ratio is 2.5 – 3 in the diatoms and 2 – 2.5 in the community. The low N/P depletion ratio is associated with the preferential recycling of phosphate below the euphotic zone, the low N/P ratio in the labile dissolved organic material in the euphotic zone and the low N/P utilization ratio in the diatoms. The low N/P and high Si/N utilization ratio reflect the low iron availability in the PFZ waters.

Chapter 1. Introduction

1.1 The Southern Ocean and its role in the global carbon cycle

The Southern Ocean refers to the vast area between Antarctica continent and Subtropical Convergence. The ocean circulation in this region is dominated by the continuous eastward-flowing Antarctic Circumpolar Current (ACC) which causes the horizontal distribution of water properties in the Southern Ocean to be relatively uniform in the zonal direction (Pickard and Emery, 1990). The surface flow of the ACC is driven primarily by the westerly wind. The wind stress and the Coriolis force cause a northward component to the surface current, which results in the formation of fronts. Between the fronts, there are zones with relatively uniform waters in both physical and chemical properties. From north to south, these fronts and zones are the Subtropical Front (STF), Subantarctic Zone (SAZ), Subantarctic Front (SAF), Polar Frontal Zone (PFZ), Polar Front (PF), Antarctic Zone (AZ), ACC Front, and the Continental Zone (CZ) (Patterson and Whitworth, 1990). The locations of the fronts and the dynamic height contours in the Australian sector are indicated in Figure 4.1.

The water masses in this region include Antarctic Bottom Water (AABW), Lower Circumpolar Deep Water (LCDW), Upper Circumpolar Deep Water (UCDW), Antarctic Intermediate Water (AAIW) and Subantarctic Mode Water (SAMW) (Rintoul and Bullister, 1999). The meridional circulation of these water masses in this region (Figure 1.1) plays an important role in the carbon and nutrients supply and export. The UCDW and LCDW upwell south of the SAF, bringing rich nutrients into surface water. Most of the upwelled UCDW transports to north through Ekman drift which replenishes the depleted nutrients in the surface water due to the biological uptake. While part of the northward surface water forms the AAIW and sinks in the PFZ, the reminder forms the SAMW due to the deep convection in the winter in the SAZ (Rintoul and Bullister, 1999; Trull et al., 2001).

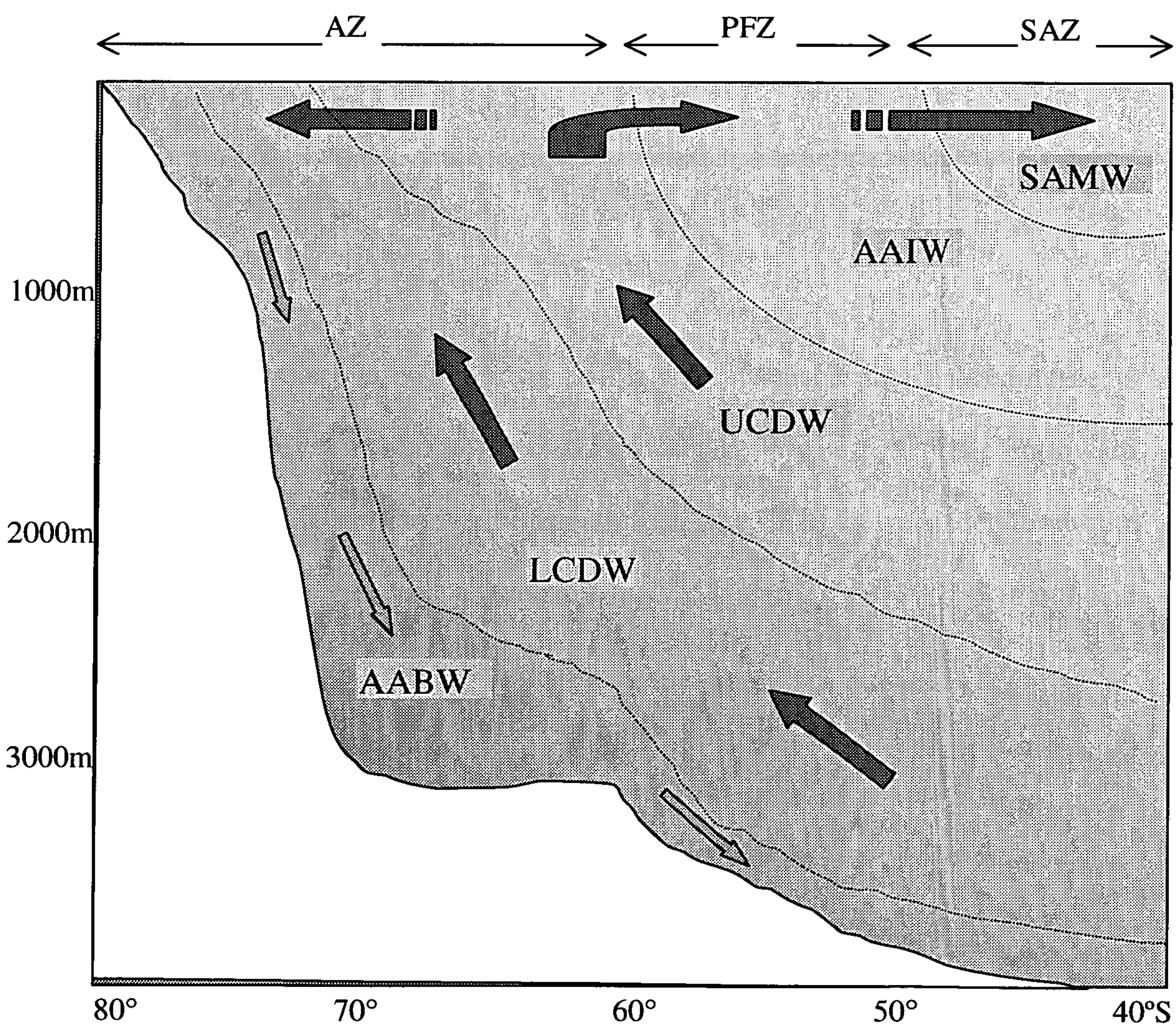

Figure 1.1. The meridional circulations in the Southern Ocean and the water masses: Antarctic Bottom Water (AABW), Lower Circumpolar Deep Water (LCDW), Upper Circumpolar Deep Water (UCDW), Antarctic Intermediate Water (AAIW) and Subantarctic Mode Water (SAMW); and the zones: Antarctic Zone (AZ), Polar Frontal Zone (PFZ) and Subantarctic Zone (SAZ).

The Southern Ocean is recognised as an important region in the oceanic contribution to global carbon flux due to its significantly contribution to atmospheric carbon dioxide (CO_2) removal (Takahashi et al., 1997; Metzl et al., 1999). This removal is partially regulated by the "biological pump" that involves the primary photosynthetic production of organic matter from carbon and nutrients in surface waters and the subsequent transport of this organic matter to deep waters (Figure 1.2). This export production lowers the concentration of total dissolved carbon in surface waters and enables more carbon to be transferred from the atmosphere and stored in the ocean.

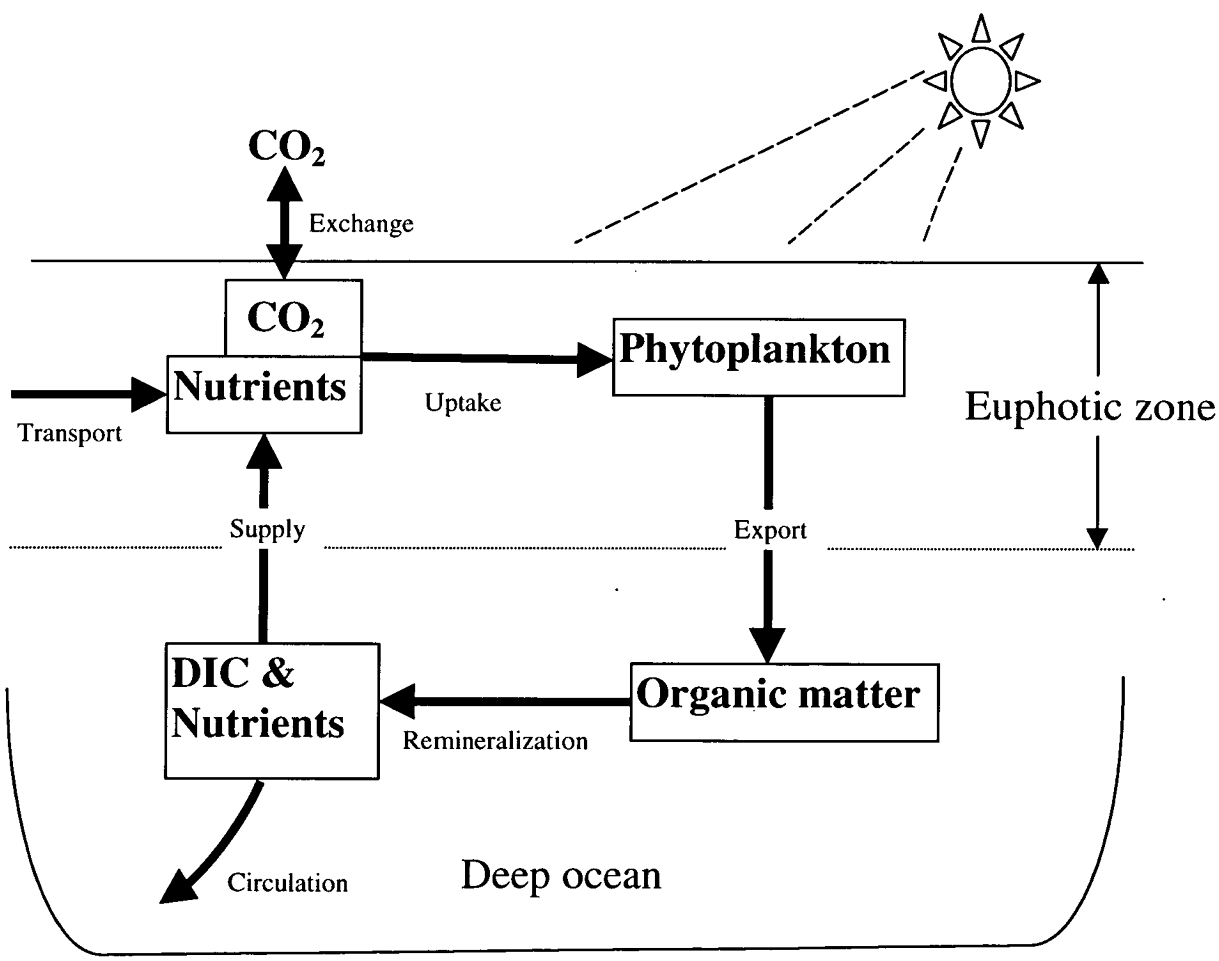

Figure 1.2. Carbon and nutrient cycle in the ocean.

1.2 The SAZ and the PFZ

The SAZ and the PFZ have been considered as carbon dioxide 'sinks' (Poisson et al., 1993; Metzl et al., 1999). In the Australian sector, the SAZ is usually located between 45-51°S, the PFZ between 52-55°S (Rintoul and Bullister, 1999). The SAZ is a region where pCO_2 in the surface water is much lower than that in the atmosphere, which results in CO_2 flux into the ocean. It is also the region where SAMW water forms and subducts. The PFZ may have less CO_2 influx in the surface (Poisson et al., 1993), but it is the region of formation of AAIW, which is transported north into deep water. Hence, it is important in transporting CO_2 from surface to deep water.

There are remarkable differences in physical, biological and chemical properties between the SAZ and the PFZ. The SAZ has a distinguishing characteristic: containing a thick nearly homogeneous layer extending from near the sea surface to a depth of 500 m or more which is formed by deep convection in winter. In contrast, the mixed layer in the PFZ is relatively shallow (about 150 m), due to the lack of deep convection in winter (Rintoul and Bullister, 1999). Phytoplankton communities differ between the SAZ and the PFZ, with diatoms dominating in the PFZ but cocolithophores dominating in the SAZ (Lourey and Trull, 2001). In both regions, nitrate and phosphate concentrations are high year-around. Silicate concentration is generally higher in the PFZ than in the SAZ, but becomes depleted in the summer in both regions. Seasonal depletion of nitrate and phosphate are larger in the SAZ relative to that in the PFZ.

1.3 Current research and results

The present magnitude of export production in the Southern Ocean has been the subject of some debate. For example, low estimates of export production were obtained when they were based on predator carbon demand (Priddle et al., 1998), but more than double the value of export production was obtained from three-dimensional assimilation of tracers (Schlitzer, 2001). The debate in export production possibly reflects different assumptions made for the different methods used in the estimations. For example, estimates of carbon utilization and export have often been obtained from extrapolation of N or P utilization using assumed Redfield C/N or C/P ratios (Jennings et al., 1984; Sarmiento and Le Quere, 1996). However, researches have shown that the classical Redfield ratios do not hold in the Southern Ocean (Jennings et al., 1984; Karl et al., 1991; DeBaar et al., 1997; Rubin et al., 1998; Arrigo et al., 2000; Sweeney et al., 2000; Lourey and Trull, 2001).

While the SAZ and the PFZ have been considered as sinks of CO_2, there is uncertainty in the relative magnitude of export production between these two regions. Using the seasonal nutrient depletion method, Lourey and Trull (2000) estimated that the export production was much greater in the SAZ (3.4 mol C m^{-2}) than the PFZ (1.4 mol C m^{-2}). However, mesopelagic suspended barium concentrations (Cardinal et al., 2001), suggested that the PFZ was the greater carbon export region. Using the sediment trap collections, Trull et al. (2001) observed that the total mass export was much greater in the PFZ than in the SAZ at 800-1000 m depth for the period of September to February, but the particulate organic carbon was less in the PFZ than in the SAZ.

1.4 The objectives of this study

In this study, I will develop a one dimensional (1-D) bio-physical model that can simulate the upper ocean dynamics. Firstly, I will identify a suitable mixed layer model which can reproduce the seasonal cycle of sea surface temperature (SST) and the mixed layer depth (MLD). Secondly, I will implement a biogeochemical model into the mixed layer model. Lastly, I will apply the bio-physical model to the SAZ and the PFZ to study the interaction of the physics and biogeochemistry.

The goal of this study is to assess more accurately, and understand better the processes controlling the export production in the SAZ and the PFZ. The three main objectives of this study are as follows:

(1) Simulate the seasonal SST and MLD in the SAZ and the PFZ in the Australian sector of the Southern Ocean.

- to assess whether the 1-D model can reproduce the upper ocean properties.
- to investigate the seasonal variability in the MLD and its response to the surface fluxes.
- to identify the factors controlling the difference in the upper ocean dynamics between the SAZ and PFZ.

(2) Simulate the seasonal phosphate export and resupply in the SAZ and the PFZ.

- To quantify the export production in the minor growing season (i.e. between March and September).
- To determine the nutrient resupply to the euphotic zone in the major growing season (i.e. between September and March).

- To compare the export production and the phosphate resupply in the SAZ with those in the PFZ.

(3) Determine the nutrient utilization ratios in the euphotic zone in the PFZ.

- To identify the possible mechanism required to reproduce the observed nutrient fields.
- To determine N/P and Si/N utilization ratios.
- To investigate the potential role of the ratio of dissolved organic nitrogen (DON) to dissolved organic phosphate (DOP) and the recycle of nitrate and phosphate on the N/P depletion ratio.

Chapter 2. Simulation of the upper ocean dynamics: The seasonal SST and MLD

1. *Poster presented at Australian Meteorology and Oceanographic Society Conference, Hobart Australia, 2001:*

Comparison of two vertical mixing schemes in both the low and the middle latitudes of the ocean

Xiujun Wang[1,2] and Richard J. Matear[1,3]

2. *Paper in press in Journal of Geophysical Research, 2001:*

Modeling the upper ocean dynamics in the Subantarctic and Polar Frontal Zones in the Australian sector of the Southern Ocean

Xiujun Wang[1,2] and Richard J. Matear[1,3]

1. Antarctic CRC, University of Tasmania, GPO Box 252-80, Hobart, 7001, Tasmania, Australia.
2. Institute of Antarctic and Southern Ocean Studies, University of Tasmania, GPO Box 252-77, Hobart, 7001, Tasmania, Australia.
3. CSIRO Division of Marine Research, GPO Box 1538, Hobart, 7001, Tasmania, Australia.

2.1 Abstract

A one-dimensional (1-D) mixed layer model (the Chen scheme) was applied in the Subantarctic Zone (SAZ) and the Polar Frontal Zone (PFZ) to simulate the upper ocean dynamics. The model was forced with four years data of the heat fluxes, freshwater fluxes and wind stresses from the National Centers for Environmental Prediction. In both the SAZ and PFZ, the 1-D model was capable of reproducing the amplitude of the seasonal sea surface temperature (SST) and the seasonality of the mixed layer depth (MLD). The shallowest MLD was found in January – February (20 m in the SAZ, 35 m in the PFZ), and the deepest MLD between August to October (600 m in the SAZ, 160 m in the PFZ). The shallower summer MLD in the SAZ than the PFZ, was due to the lower wind stress. However, the shallower winter MLD in the PFZ than the SAZ was due to the strong stratification in the water below the mixed layer. In the SAZ, variability in the wind stress was the dominant term driving the fluctuation in MLD in the summer, but variability in the heat flux was the major factor controlling the timing of the deepening and shoaling of the mixed layer in the winter. In the PFZ, both the variability in the wind stress and the heat flux dominated the variability of the MLD in both the summer and the winter.

2.2 Introduction

The behaviour of the upper ocean is crucial to determining the ocean properties and air-sea gas exchanges. For example, the dynamics of the upper ocean is a key element to carbon cycling and any attempt to simulate carbon cycling requires an adequate mixed layer model. In the ocean, mixing caused by turbulence greatly exceeds molecular diffusion. The generation of this turbulent mixing comes from the inputs of kinetic energy primarily by wind stress and potential energy by buoyancy flux caused by the air-sea exchanges of heat and freshwater (Pickard and Emery, 1990).

A number of mixed layer models have been developed to model vertical mixing in either one-dimensional (1D) or three-dimensional models (Mellor and Yamada, 1982; Schopf and Cane, 1983; Martin, 1985; Price et al., 1986; Gaspar et al., 1990; Chen et al., 1994; Large et al., 1994; Kantha and Clayson, 1994; Anderson and Weller, 1996; Godfrey and Schiller, 1997). These different models can be classified into three schemes. The first scheme is the so-called bulk mixed layer model which simulates a planetary boundary layer (a homogeneous mixed layer that exists right below the ocean surface). Entrainment is calculated either by an energy balance model which relates the entrainment velocity directly to momentum and buoyancy fluxes at the ocean surface (Niiler and Kraus, 1975; Davis et al., 1981), or by a shear instability model which allows the mixed layer to deepen until the bulk Richardson number exceeds a critical value (Pollard et al., 1973; Deardorff, 1983). The second vertical mixing scheme is a turbulence closure scheme, in which the eddy coefficient is prescribed to be a function of the gradient Richardson number (Pacanowski and Philander, 1981; Mellor and Yamada, 1982).

The third scheme combines the bulk mixed layer model and the turbulence closure model (Price et al., 1986, Chen et al., 1994, Large et al., 1994). For example, Chen and others (1994) developed a hybrid vertical mixing scheme (the Chen scheme), which combines the Kraus-Turner bulk mixed layer model (Kraus and Turner, 1967) and the Price's dynamical instability model (Price et al., 1986). Another combined mixing scheme is the 'K profile parameterization' (KPP) scheme that simulates the oceanic boundary layer physics (Large et al., 1994).

The bulk mixed layer models are computationally efficient and easy to implement. They are successful in conditions of prolonged cooling and strong winds, but underestimate the mixed layer depth in the equatorial region where weak wind conditions prevail (Chen et al., 1994). On the other hand, the turbulence closure models perform well when the surface is being warmed and/or freshened, and winds are light to moderate. But they under-predict the mixed layer depth (MLD) in middle to high latitude regions due to the lack of simulation of wind stirring (Chen et al., 1994; Godfrey and Schiller, 1997). The combined mixed layer model exploits the advantages of the bulk mixed layer scheme and the turbulence closure scheme to produce a robust scheme suitable for a variety of conditions (Chen et al., 1994). Several studies have shown that the combined mixed layer model is capable of predicting the changes of the sea surface temperature (SST) and the MLD in different regions (Chen et al., 1994; Large et al., 1994; Anderson and Weller, 1996; Doney, 1996; Godfrey and Schiller, 1997). For example, Chen et al. (1994) demonstrated that the Chen scheme behaved more realistically in both idealized experiments and realistic simulations for the Ocean Weather Station Papa and the equator (TOGA COARE), than either the bulk mixed layer model

(Kraus and Turner, 1967) or the MY2.5 model (Mellor and Yamada, 1982). Using the Chen scheme in a 1D model with the four-month mooring flux data (November 1992 – February 1993), Godfrey and Schiller (1997) successfully simulated the SST over the period, except during a prolonged wind burst when the observed SST decreased faster than predicted because of the horizontal advection. Similarly, the KPP scheme has showed capacity for reproducing the observed behaviour of the SST and MLD in the station Papa, Long-Term Upper Ocean Study (LOTUS) and the Bermuda Atlantic Time-Series Study site (BATS) (Large et al., 1994; Doney 1996).

Due to the lack of observational data sets in both the atmosphere and the ocean, there have been limited studies of the mixed layer dynamics in the open ocean water of the Southern Ocean. Using the monthly forcing data from European Centre for Medium-Range Weather Forecast (ECMWF), Häkkinen (1995) applied a second-moment closure vertical mixing scheme (Mellor and Yamada, 1982) in a coupled ice-ocean model to simulate the MLD in the Southern Ocean. Her simulation produced a maximum winter MLD of about 200 m near 47 °S in the Australian sector, based on the criterion of a temperature change of 0.3 °C. Her simulated MLD was much less than the observed value of 600 m (Rintoul and Trull, 2001). Markus (1999) used a bulk mixed layer model (Kraus and Turner, 1967) to simulate the mixed layer properties in the Southern Ocean between 50 °S and the Antarctic continent. Using the ECMWF forcing data from the year 1992, the model produced the annual SST amplitude of 2.5 °C between 50 and 55 °S in the Australian sector, which is less than the observed value of 3–4 °C (Rintoul, pers. comm.). This suggests that some of the mixing processes is probably missing from these modelling studies, and there is a need to identify a suitable mixing scheme for the Southern Ocean.

While the Chen scheme (Chen et al., 1994) and the KPP scheme (Large et al., 1994) have showed the capacity for simulating the upper ocean dynamics at various sites, neither has been tested in the Southern Ocean. Hence, the goal of this study is to investigate whether these schemes can reproduce the upper ocean dynamics in the Southern Ocean, and to identify a suitable mixed layer for the region. This study focuses on the north (SAZ) and the south (PFZ) of the SAF where the curl of the surface wind stress is small, reflecting weak upwelling and downwelling (Trull et al., 2001a). Using the 4-year (1995-1998) averaged wind stress (Kalnay, 1996), the rates of upwelling in the PFZ and downwelling in the SAZ are estimated to be 10 and 21 m/y, respectively, which are much smaller than the entrainment/detrainment rate (>300m/y) (Appendix A). These conditions make the choice of the 1D model without the term of upwelling or downwelling appropriate. Hence in the following description of the 1D model, the Ekman contribution to vertical motion and upwelling and downwelling are neglected.

2.3 Model description

The time evolution of the profiles of temperature (T), salinity (S) and velocity components (U and V) at a depth z are given by the equations:

$$\frac{dT}{dt}=\frac{d}{dz}\left(K_z\frac{dT}{dz}\right)+\text{source} \tag{2.1}$$

$$\frac{dS}{dt}=\frac{d}{dz}\left(K_z\frac{dS}{dz}\right) \tag{2.2}$$

$$\frac{dU}{dt}=\frac{d}{dz}\left(V_z\frac{dU}{dz}\right)+fV \tag{2.3}$$

$$\frac{dV}{dt}=\frac{d}{dz}\left(V_z\frac{dV}{dz}\right)-fU \tag{2.4}$$

where f is the Coriolis parameter and K_z and V_z are the diffusivity and viscosity, respectively, which are computed by the mixed layer model. The Ekman upwelling and downwelling terms have been ignored because they are small (see section 2.2), and so have the large scale circulation contributions to vertical motions because they are also small, and similar in magnitude to the Ekman terms (Bi, 2001). Thus, in these oceanographic locations we are able to focus on the development and evaluation of the 1D model.

2.3.1 The Chen scheme

The Chen scheme was described in detail by Chen et al. (1994) and Godfrey and Schiller (1997). There are three steps in the model for simulating the vertical mixing. The first step determines the Kraus depth (H_k) which is calculated from the surface friction velocity and total buoyancy flux. In this layer (0–H_k), K_z and V_z are set to 50 cm^2 s^{-1}. In the second step, K_z and V_z below the Kraus depth are calculated using a Richardson number parameterization. The K_z and V_z estimated from the first two steps are used to calculate the profiles of the T, S, U and V by integrating the equations (2.1-2.4). Finally, the density profile is checked for instabilities, and the instabilities are removed by homogenizing the T and S values with the underlying water.

2.3.1.1 Kraus depth determination

It was assumed that eddy diffusivity and viscosity was large within the Kraus depth (H_k). H_k was determined by the equation:

$$\frac{dH_k}{dt} = W_e, \tag{2.5}$$

Where W_e is the entrainment (detrainment) rate when it is positive (negative). It was calculated by the Kraus-Turner bulk turbulent model (Niiler and Kraus, 1975):

$$W_e H_k(b_1 - b_2) = 2mu_*^3 + H_k[(1+n) B_0 - (1-n)|B_0|]/2 + B_1 \quad (2.6)$$

In equation (2.6), b_1 and b_2 are the buoyancies of water in the Kraus depth and just below it, m and n are constants (m = 0.4, n = 0.18), u^* is the surface friction velocity, B_0 is the total surface buoyancy flux, and B_1 is the rate of potential energy generation due to penetration of solar radiation. B_0 and B_1 are given by:

$$B_0 = \alpha g/\rho\, Cp\, (H_t - I_0) + \beta g\, S_0 (E - Pr) \quad (2.7)$$

$$B_1 = r\, I_0[H_k (1 + exp^{-Hk/Hr}) - 2H_r (1 - exp^{-Hk/Hr})], \quad (2.8)$$

where α and β are the thermal and haline coefficients of expansion, respectively. Cp is the specific heat of water and ρ its density. H_t is the total downward heat flux at the surface, I_0 the penetrating component of the solar radiation. S_0 is a mean surface salinity, E and Pr are evaporation and precipitation rates. H_r is the e-folding depth for the penetration of solar radiation.

2.3.1.2 Richardson number formulation

Below the Kraus depth, the eddy diffusivity and viscosity are strong functions of the Richardson number (Ri). The Richardson number is a parameter used to characterize the intensity of turbulence mixing and it depends on the stratification and the vertical shear:

$$Ri = \frac{g}{\rho} \frac{\partial \rho / \partial z}{(\partial u / \partial z)^2} \quad (2.9)$$

Using Ri, the diffusivity and viscosity are calculated as follows (Pacanowski and Philander, 1981):

$$K_z = K_b + \frac{K_m}{(1+5Ri)^5} \tag{2.10}$$

$$V_z = V_b + \frac{V_m}{(1+5Ri)^5} \tag{2.11}$$

Where K_m and V_m are the maximum diffusivity and viscosity, respectively, which are set to 50 $cm^2\ s^{-1}$, K_b and V_b the background values, which are 0.1 and 1 $cm^2\ s^{-1}$, respectively.

2.3.2 The KPP scheme

The KPP scheme was described in detail by Large et al. (1994) and Doney et al. (1995). The model predicts the vertical turbulent fluxes in the oceanic planetary boundary layer (PBL) which is defined as the penetration depth for surface generated turbulence and depends upon the stratification, velocity shear and surface buoyancy forcing.

2.3.2.1 The boundary layer depth and the diffusivity in the boundary layer

The PBL depth h is determined prognostically based on a bulk Richardson number stability criteria, where the bulk Richardson number Ri_b relative to the surface is defined as:

$$Ri_b(d) = \frac{(B_r - B(d))d}{(V_r - V(d))^2 + V_t^2(d)} \tag{2.12}$$

Where B_r and V_r are the surface reference of buoyancy and velocity, and V_t accounts for unresolved shear generated by surface turbulence and is set to give the correct entrainment flux for the pure convective case (Large et al., 1994). The depth h is taken to be the smallest value of d at which Ri_b equals the critical value of 0.3.

In the PBL, the shape of the diffusivity profile $K_z(z)$ is specified as a function of the distance $d = -z$ from the surface, and determined by a turbulent velocity scale $w_r(z)$ and the depth of the boundary layer:

$$K_z(z) = hw_r\left[\frac{d}{h}\left(1-\frac{d}{h}\right)^2\right] \tag{2.13}$$

The turbulent velocity scale w_r increase with surface wind stress and unstable surface buoyancy (Large et al., 1994).

2.3.2.2 Diffusivity below the boundary layer

Mixing below the boundary layer is thought to be driven primarily by the shear instability which is described by the local gradient Richardson number,

$$Ri_g = \frac{g/\rho}{(\partial_z U)^2 + (\partial_z V)^2} \tag{2.14}$$

and the diffusivity is parameterized as a function of Ri_g:

$$K_z = K_m \qquad \mathrm{Ri_g} < 0 \tag{2.15}$$

$$K_z = K_m\left[1-\left(\frac{Ri_g}{Ri_0}\right)^2\right]^3 \qquad 0 < \mathrm{Ri_g} < 0.7 \tag{2.16}$$

$$K_z = 0 \qquad \mathrm{Ri_g} \geq 0.7 \tag{2.17}$$

where K_m is the maximum diffusivity (50 cm^{-2} s^{-1}), and Ri_0 is a critical value (0.7).

2.4 Model set-up

To run the 1D model, we need to configure the model, to prescribe the initial profiles of *T*, *S*, *U* and *V*, and to provide surface input of heat, freshwater and wind stress. The chosen simulation sites for the SAZ and PFZ are 47°S, 142°E and 54°S, 140°E, respectively. Initial profiles of temperature and salinity are extracted from CTD data from *Aurora Australis* cruise au9501 (Figure 2.1) (Rosenberg et al., 1997). Velocity profiles are initialized to zero at all depths. This may result in some transient mixing events in the initial period of the simulation (Godfrey and Schiller, 1997) hence the model is started in winter and allowed to spin up for a few months. The surface fluxes of heat, salt and momentum are applied as surface boundary conditions, and the model bottom boundary is closed so that diffusive fluxes are not allowed cross the model base. The model domain is 1000 m, with a uniform vertical grid spacing of 5 m depth. A time-step of one minute is used in the model run, and daily averaged values are displayed in the output.

The forcing data required by the model were obtained from the NCEP, and they included six-hourly averages of the components of wind stress, the precipitation, and the net short wave, long wave, latent, and sensible heat fluxes (Kalnay et al., 1996).

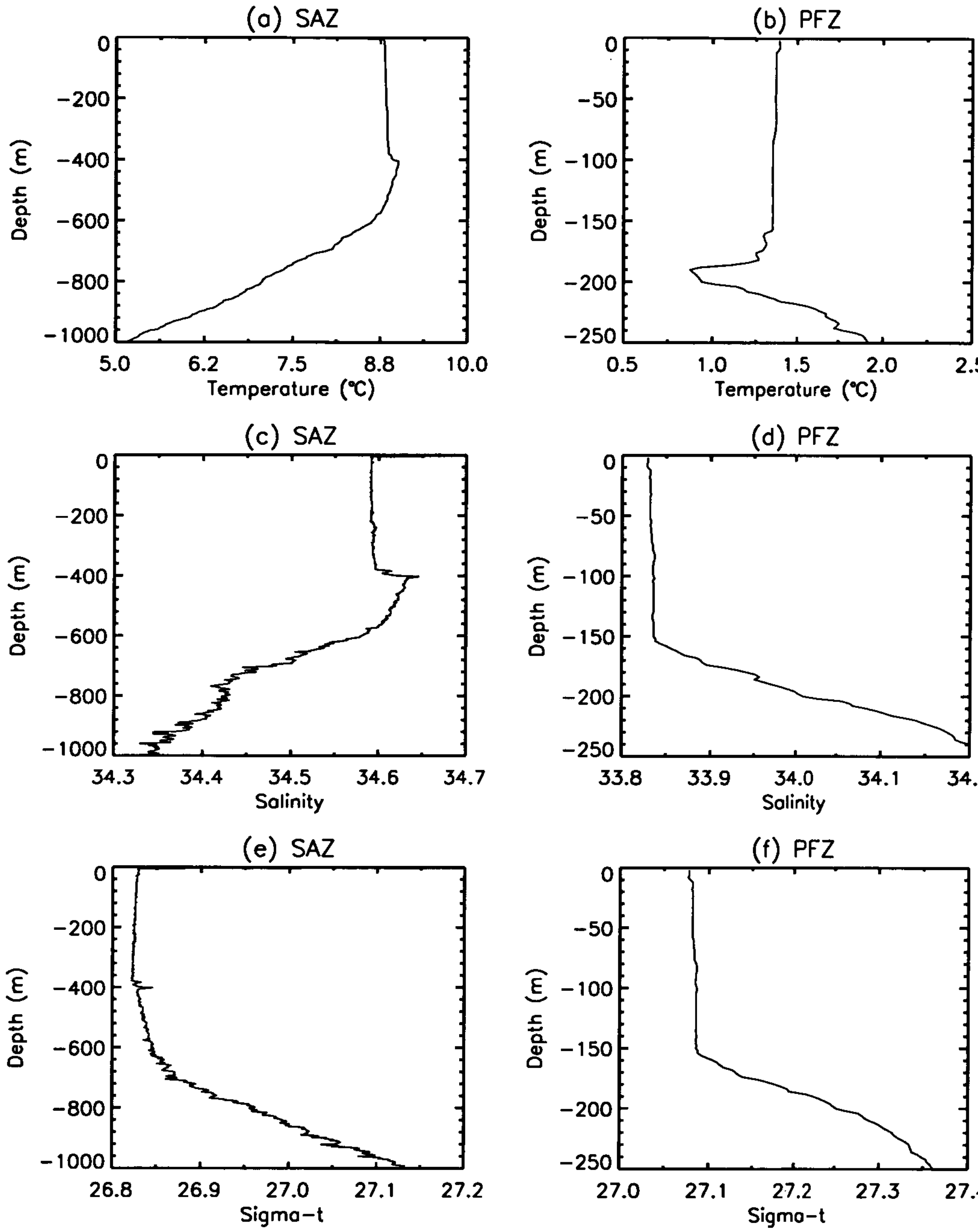

Figure 2.1 Profiles of the temperature, salinity and sigma-t used to initialize the model for the SAZ and the PFZ. The profiles come from AU9501 CTD (Station 9 for the SAZ, Station 30 for the PFZ) collected in late July 1995.

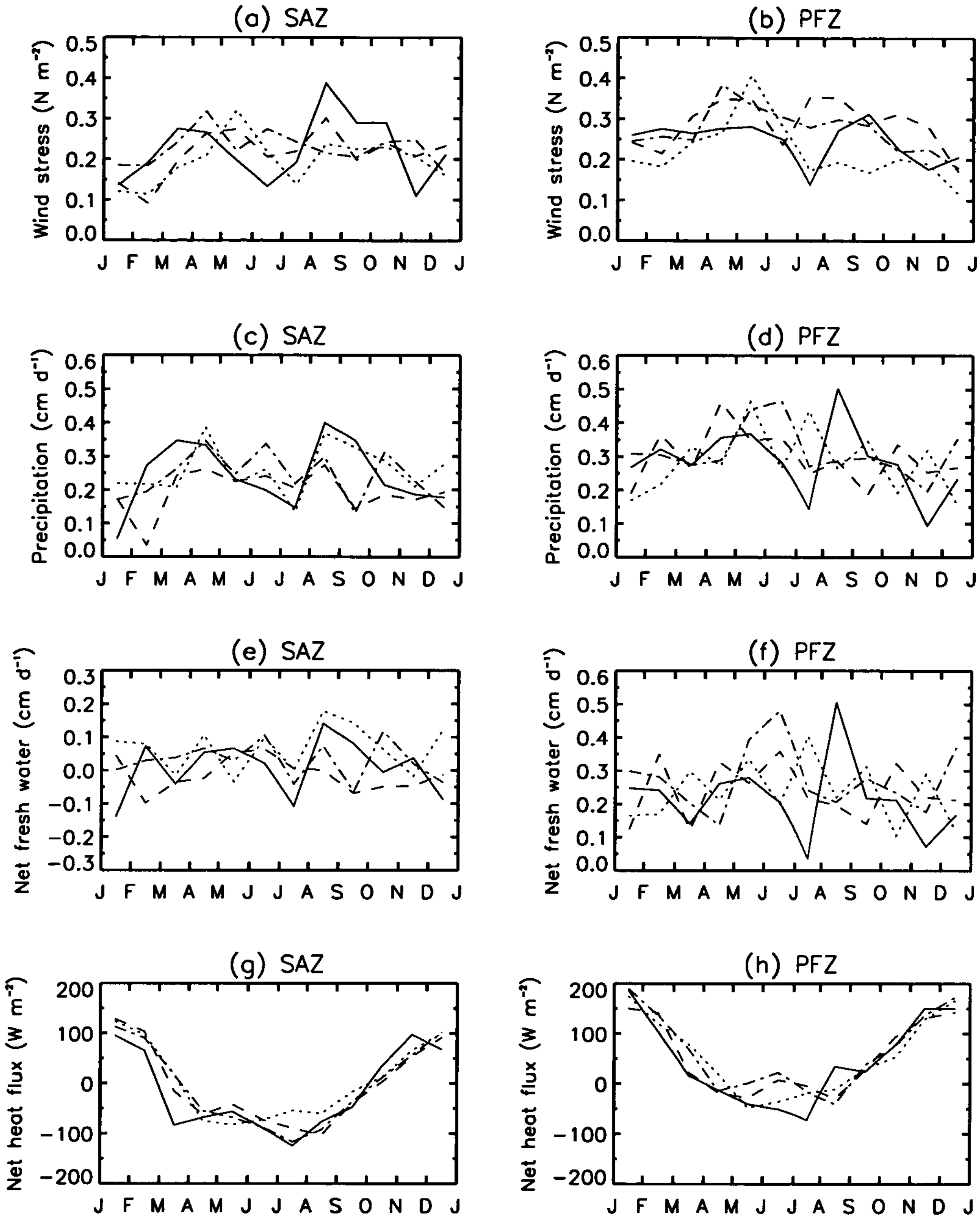

Figure 2.2 Monthly mean wind stress, precipitation, net freshwater flux, total net heat flux and its four components (net short wave, long wave, latent heat and sensible heat) in the SAZ (46.7°S 142.5°E) and the PFZ (54.3°S 140.6°E) for the year 1995 (solid), 1996 (dotted), 1997 (dashed), and 1998 (dot-dashed).

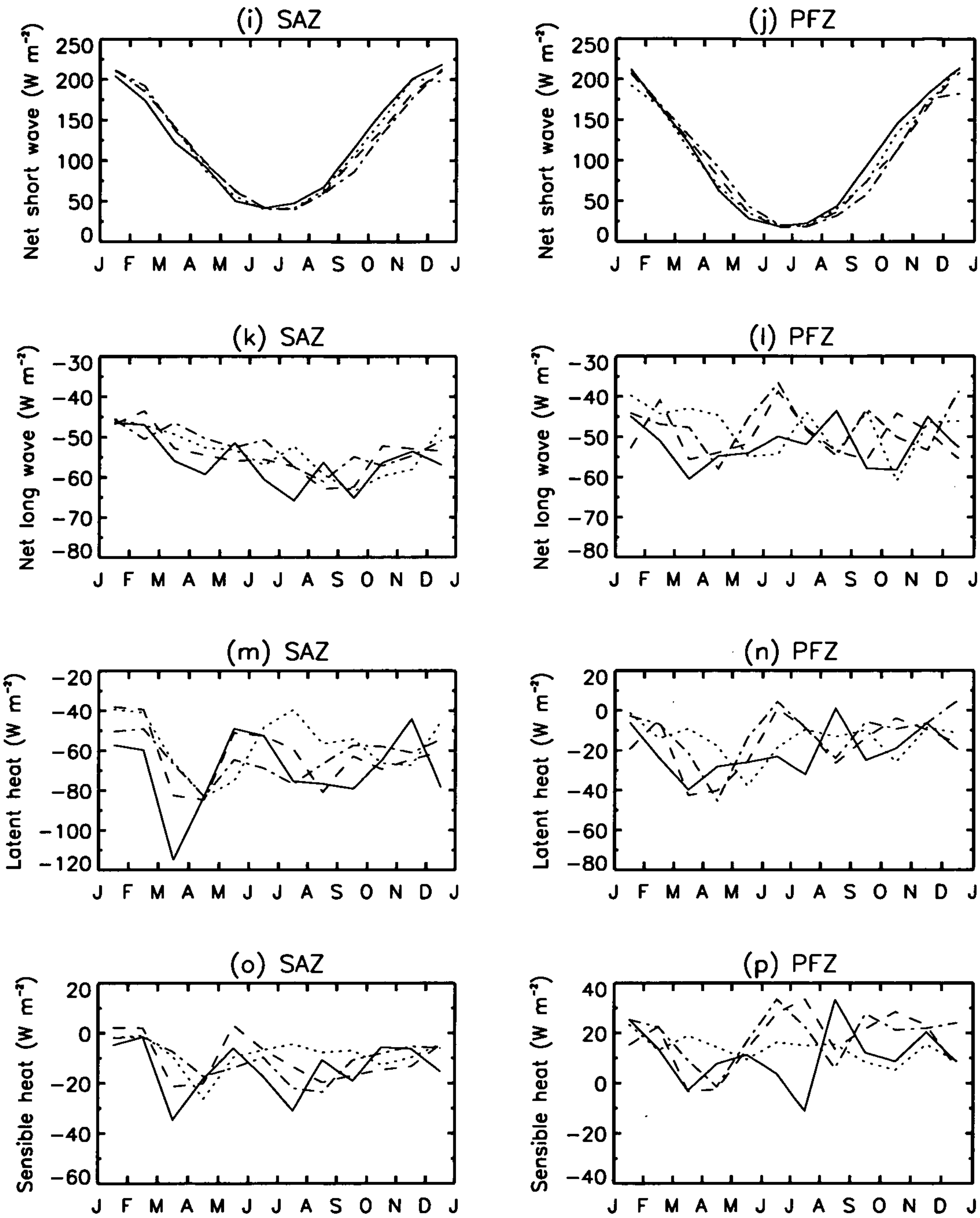

Figure 2.2. (continued)

Table 2.1. Annual wind stress, fresh water flux, and heat fluxes at the sea surface. Positive value indicates downward flux.

	SAZ					PFZ				
Surface flux	1995	1996	1997	1998	mean	1995	1996	1997	1998	mean
Wind stress (N/m^2)	0.222	0.199	0.215	0.225	0.215	0.246	0.215	0.290	0.271	0.255
Precipitation (cm/y)	87.3	96.6	71.0	84.8	84.9	103.3	103.4	109.1	113.6	107.6
P-E (cm/y)	2.08	26.46	-5.86	8.27	7.9	77.9	85.0	88.5	100.0	88.0
Net heat (w/m^2)	-13	6	-3	-2	-3	49	55	56	66	57
Short wave	126	125	124	123	125	111	105	105	105	107
Long wave	-56	-54	-54	-53	-54	-52	-48	-49	-47	-49
Latent heat	-69	-57	-63	-62	-63	-20	-15	-17	-11	-16
Sensible heat	-14	-8	-10	-10	-11	11	13	17	19	15
Advective correction										
Heat	0	-5	0	0		-54	-44	-66	-58	
Freshwater	0	-22	0	0		-85.3	-69.4	-104.8	-92.1	

Figure 2.2 shows that at both sites, there was very weak seasonality in the wind stress, increasing with time from January to April, but decreasing from October to December. On average, the wind stress was significantly higher in the PFZ (0.255 N m^{-2}) than in the SAZ (0.215 N m^{-2})(Table 2.1). Neither site displayed seasonality in the precipitation and the net freshwater flux. On average, the precipitation was 0.25 and 0.3 cm d^{-1} in the SAZ and the PFZ, respectively. However, the PFZ had a large amount of net freshwater gain by the ocean (0.24 cm d^{-1}) while the SAZ only gained about 0.02 cm d^{-1}. Both sites showed a prominent seasonal pattern in the net heat flux, but there was about 50 W m^{-2} more heat gain by the ocean surface in the PFZ than in the SAZ. The seasonality in the net heat flux was mainly due to the net short wave while the difference in the annual net heat flux between the two sites was due to the differences in the latent and the sensible heat fluxes. On average, the SAZ lost 63 W m^{-2} and 11 W m^{-2} due to the latent heat and the sensible heat, respectively. However, the PFZ only lost 16 W m^{-2} due to the latent heat but gained 15 W m^{-2} due to the sensible heat (Table 2.1). Overall, the SAZ site had negligible annual net heat loss (3 W m^{-2}) and net freshwater gain (8 cm yr^{-1}), while the PFZ site had large annual net heat gain (57 W m^{-2}) and freshwater gain (88 cm yr^{-1}). The large amount of heat and freshwater gains in the PFZ is unique to the site tested. Moving east or west, the annual net heat and freshwater gains are significantly less.

Both sites displayed interannual variability in the surface fluxes. In the SAZ site, 1996 was the only year with annual net heat (6 W m^{-2}) and fresh water (26 cm yr^{-1}) gains by the ocean. The heat gain was mainly due to the reduced heat loss by the latent and the sensible heat in the winter, compared with the other years (Figure 2.2). In addition to the heat and freshwater fluxes, the year 1996 had the lowest averaged wind stress (Table 2.1), indicating that 1996 was an anomalous year. In contrast, the year 1995 had pronounced annual net heat loss (13 W m^{-2}), with relatively high wind stresses in the winter (Figure 2.2a), which suggested that 1995 might show strong mixing in the winter. In the PFZ, the largest interannual variability was found in the wind stress, ranging from 0.215 to 0.290 N m^{-2} (Table 2.1). The variation in the wind stress in the winter was twice that in the summer (Figure 2.2b). The annual net freshwater and heat gains showed an increasing from 1995 to 1999. This trend was mainly due to the decrease in the heat loss by the latent heat and the increase in the heat gain by the sensible heat at the sea surface.

2.5 Model experiments

In this section, I first investigate the model sensitivity to the advective corrections for the heat and the freshwater fluxes and to the initial condition using the Chen scheme. Then a comparison study of the Chen scheme and the KPP scheme is carried out to identify a suitable mixed layer scheme for the region. The SST and MLD simulated by either scheme are used to evaluate whether the 1D model can successfully simulate the upper ocean dynamics in the SAZ and the PFZ. Finally, a mixed layer scheme is to be chosen based the model performance and a series of experiments are undertaken to investigate the variability in the MLD to the variability in the surface forcing.

2.5.1 Sensitivity to the fluxes correction and initial condition

To use the surface forcing data in the 1D model, the net air-sea fluxes must be balanced over the long term by the heat and freshwater fluxes (Doney, 1996). To close the heat and freshwater budgets on interannual scale, two types of advective correction were applied: (1) constant surface correction for the whole year, (2) time dependent correction, which was uniformly spread over the Kraus layer:

$$F(t) = \overline{F}\ \frac{\tau_x(t)}{\overline{\tau}_x} \tag{2.18}$$

where $F(t)$ is the advective correction for the heat or the freshwater flux at time t, $\overline{F}$ four-year averaged heat or freshwater flux required to close the heat or the salt budget, $\tau_{x(t)}$ the eastward wind stress at time t, $\overline{\tau}_x$ the four-year averaged eastward wind stress. This advective correction is based on the assumption that the heat and freshwater gains/losses at the surface were removed by the Ekman transport which was dependent on the eastward wind. The calculated annual rates for the advective heat and freshwater corrections are given in Table 2.1.

In the PFZ, the four-year averaged advective corrections were –57 W m^{-2} and –88 cm yr^{-1} for the heat flux and the freshwater fluxes, respectively. The observations along 140°E show that salinity decreases from the Antarctic Zone to the Polar Frontal Zone, but increases from the Subantarctic Front to the north (Rintoul and Bullister, 1999; Trull et al., 2001a). This indicates that Ekman transport will bring cold and salty water from further south. Using the surface flux corrections, the 1D model produced relatively small SST seasonal amplitude in the PFZ. By applying the time dependent advective corrections over the Kraus layer, the model was able to reproduce the seasonal amplitude of the observed SST.

In the SAZ, the four-year averaged advective corrections were 3 W m^{-2} and –8 cm yr^{-1} for the heat flux and the freshwater fluxes, respectively. Applying these advective corrections at the surface, the 1D model produced seasonal MLD evolution that was almost identical to that in a simulation without the advective corrections. In these two simulations (with advective corrections and without advective corrections), the model simulated realistic MLD for 1995, 1997 and 1998. Using the 1996 forcing data with advective corrections determined from four-year averaged value, the model produced a winter MLD of 150 m, much less than 440 m observed in the winter of 1996. The annual heat and freshwater fluxes for 1996 revealed that this was an anomalous year with both heat and freshwater producing a net positive buoyancy flux into the ocean (Table 2.1). Under these anomalous conditions, one would expect increased stratification of the upper ocean and a shallower mixed layer. Therefore, the second type of correction was used with the annual net heat (–6 W m^{-2}) and freshwater (–26 cm y^{-1}) closed for the year 1996. This simulation produced a more realistic winter MLD (450-600 m) and better seasonal SST in the year 1996. For the other years, no corrections were applied because the advective correction did not affect the seasonal MLD.

The initial conditions for the model simulations were based on winter profiles of temperature and salinity (July 1995), and the model was run from the winter when the water column starts to stratify and allowed for four months spin-up. To assess the sensitivity of the model to the initial conditions, two runs were performed by starting the model from two different start times – July 20 and September 1. For the January – June and October – December periods, the two runs simulated almost identical MLD. During the July – September period when the MLD averaged 600 m in the SAZ and 150 m in the PFZ, the MLD was about 50 m deeper in the SAZ (20 m in the PFZ) in the July run than the September run. Both runs simulated the deepest mixed layer in early September, and this leads to my choice of the starting time being the first September.

2.5.2 The comparison of the Chen scheme and the KPP scheme

Due to the different structure between the Chen and the KPP scheme, it is impossible to apply the same type of advective correction except the surface correction. Hence the ideal test site is a region where there is no strong horizontal transport. Since there is no need to apply the advective correction for most of years in the SAZ, this region is chosen for the purpose of this comparison study.

The models were forced with 16 months (September 1996–December1997) data of the heat fluxes, freshwater fluxes and wind stresses from the NCEP. In this region, both models reproduced seasonal SST pattern in amplitude and in the timing of the SST minimum and maximum. In general, the seasonality of the mixed layer depth (MLD) was consistent between the simulations and observation (Figure 2.3). However, during the January–March period, the model simulations underpredicted the MLD by 35 m, which could be partially attributed to the potential bias in the NCEP forcing (see Discussion section). Overall, both models produced very similar features in the SST, the SSS and the MLD, in particular during the period of late August – October both models displayed similar patterns of sharp deepening and shoaling in the MLD. The simulated MLDs were highly correlated between the Chen scheme and the KPP scheme in all the seasons, but statistic analysis indicated that the best match was in winter (Table 2.2). Despite of the overall similarity, the Chen scheme predicted slightly shallower MLD during the period of September – February but deeper MLD for the other period than the KPP scheme (Table 2.2).

Table 2.2. Comparison of the simulated MLDs between the Chen and the KPP.

	---------------- Season	-----------------			
Statistics	SON	DJF	MAM	JJA	*Ideal*
MLD_Chen (m)	247	21	65	160	
MLD_KPP (m)	291	24	62	149	
Correlation	0.96	0.91	0.87	0.98	1
Vc/Vk *	1.34	6.72	0.27	0.01	1

$$* \; Vc/Vk = \frac{\frac{1}{n}\sum_{1}^{n}(MLD_{chen}-\overline{MLD}_{chen})^2}{\frac{1}{n}\sum_{1}^{n}(MLD_{KPP}-\overline{MLD}_{KPP})^2}$$

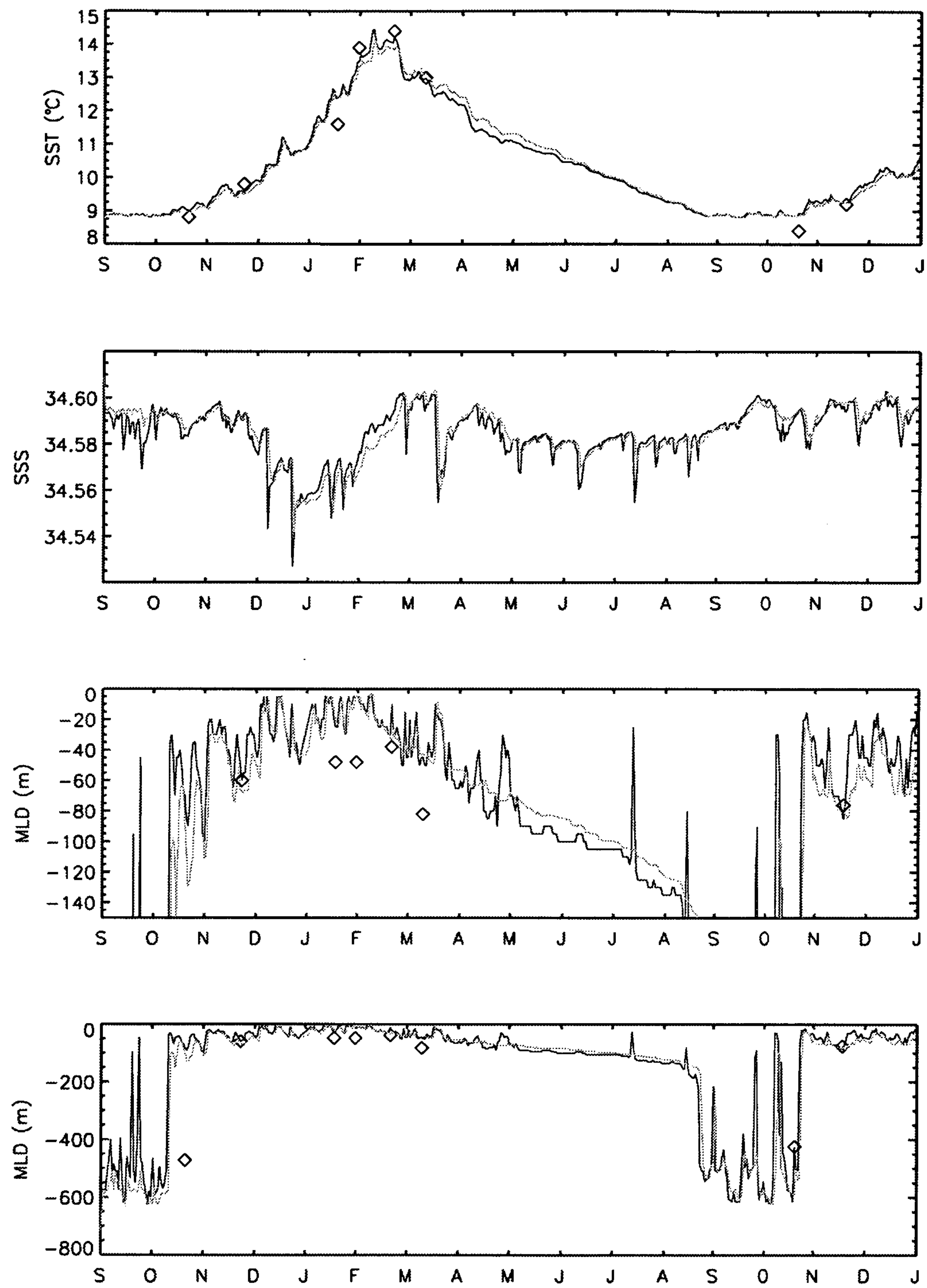

Figure 2.3 The daily sea surface temperature (SST), sea surface salinity (SSS), and mixed layer depth (MLD) from the simulations by the Chen scheme (dark line) and the KPP scheme (light line) and observation for the period of September 1996 to December 1997 in the Subantarctic Zone of the Southern Ocean.

2.5.3 The seasonal cycle of the SST and MLD in the SAZ and the PFZ

A crucial element of any successful mixed layer model is the ability to accurately predict changes in the SST and the MLD, given reliable estimates of the surface fluxes of the heat, freshwater and momentum. The problem of testing any mixed layer model in the Southern Ocean is that there are no long time series data sets of observation for atmosphere and ocean. NCEP data sets contain useful information, but the variables (such as surface heat and freshwater fluxes) should be used with caution (Kalnay et al., 1996). Given the potential errors in the forcing data, a control experiment is performed using the four different years (1995-1998) NCEP data to simulate the seasonality of the SST and the MLD. Comparison of the Chen and the KPP schemes indicated that both schemes are capable of simulating the upper ocean dynamics in the Southern Ocean. Therefore, in the following sections, the Chen scheme will be used for all the simulations.

2.5.3.1 The SAZ

Figure 2.4a shows the seasonal evolution of the SST (mean+sd, mean-sd) from the four different years of forcing data along with the Reynolds SST (mean+sd, mean-sd) from 1995 to 1998 in the SAZ. In general, the model reproduced seasonal SST pattern in amplitude and in the timing of the SST minimum and maximum. The simulated SST (mean±sd) overlapped the Reynolds SST (mean±sd) for most of the year.

Figure 2.4b and 2.4c show the simulated mean MLD from the four simulations and the observed MLD which was derived from Rintoul and Trull (2001). The MLD in the model was determined by the density difference of 0.02 between the surface and the depth. The mixed layer was shallower than 80 m during the period of November to March when wind stirring (the Kraus depth) controlled the depth of the mixed layer. A very shallow mixed layer (20 m) was found in January and lasted for less a week, which could be attributed to the large heat influx with the low wind stress (Figures 2.1a and 2.1e). A deep winter mixed layer (270–600 m) was produced in July – September but the Kraus depth only reached 80 m on average, which indicated that the deep winter mixed layer was not caused by the wind stirring but by the shear instability and deep convection. The modelled MLD was consistent with the observed MLD except in January – March and in July (Figure 2.4). During the period of January – March, the model underestimated the MLD by 15 m. In July, the modelled MLD was 270 m, which was much less than the observed MLD of 600 m in 1995 (Rintoul and Trull, 2001), but was close to the MLD of 260 m found in July 1999 from unpublished CTD data (au9901). The large difference between the two observed MLDs in July reflects large interannual variability in the MLD in early winter. This is demonstrated by the large standard deviation of the MLD in July (nearly 300 m) in this experiment (Figure 2.6).

2.5.3.2 The PFZ

In the PFZ, the simulated seasonal SST cycle using the four years of forcing data showed that the model reproduced the seasonal pattern and annual amplitude of the Reynolds SST (4.0 °C for the simulated SST and 4.1 °C for the Reynolds SST, Figure 2.5a). However, the simulated SST appeared about 0.5 °C lower than the Reynolds SST. The temperature profile used to initialize the model had a SST that was about 0.8 °C lower than the Reynolds SST, which could explain the systematic difference between the simulated SST and the Reynolds SST.

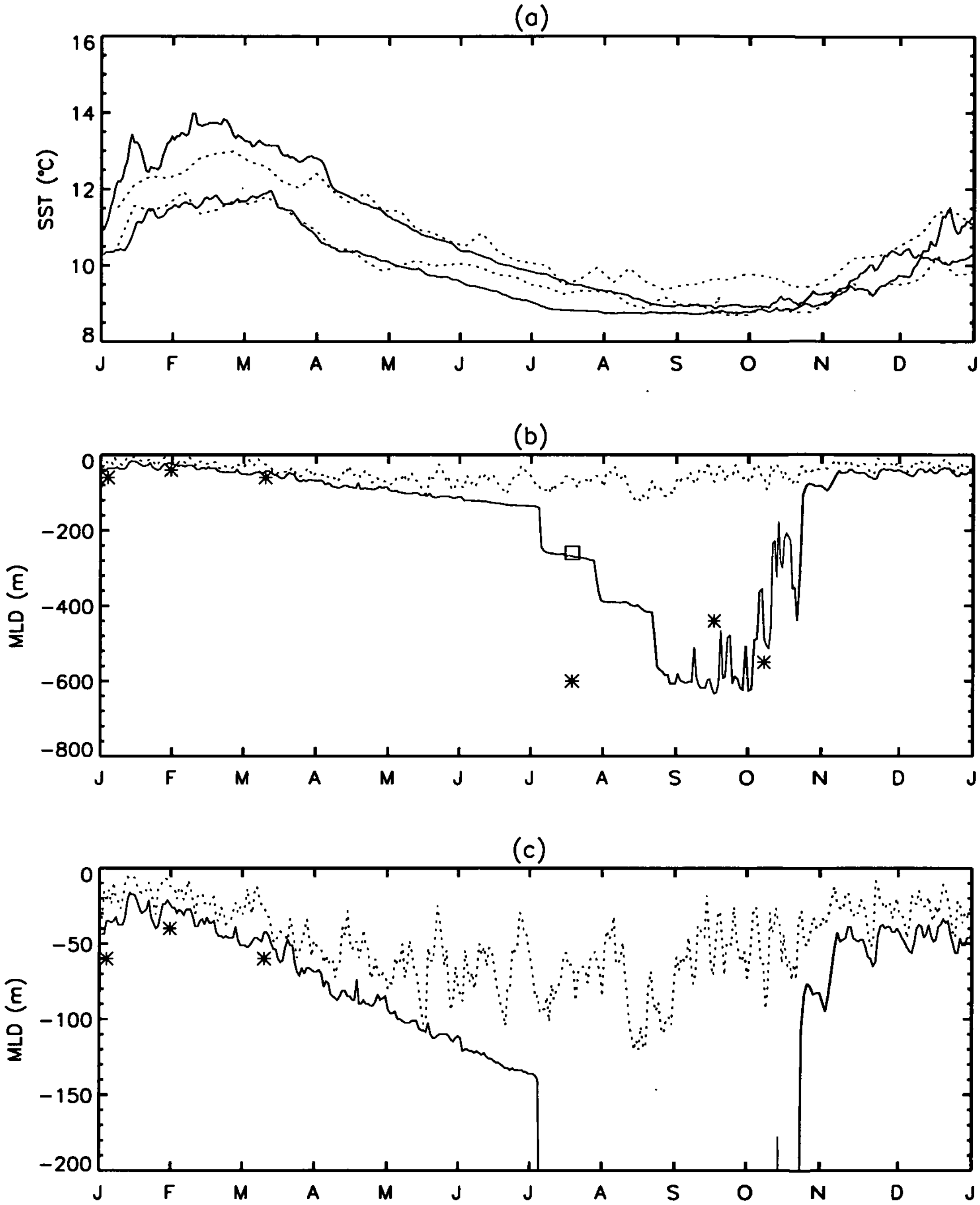

Figure 2.4. The daily SST and MLD in the SAZ. (a) Modelled SST+sd (upper solid line), SST–sd (lower solid line), the Reynolds SST+sd (upper dotted line) and the Reynolds SST–sd (lower dotted line). (b) The MLD (solid line), the Kraus depth (dotted line), and the observed MLD (✳) derived from the averaged MLD of 46–48°S from Rintoul and Trull (2001) and the MLD from unpublished AU9901 CTD data (□). (c) Same as (b) except for the upper 150 m.

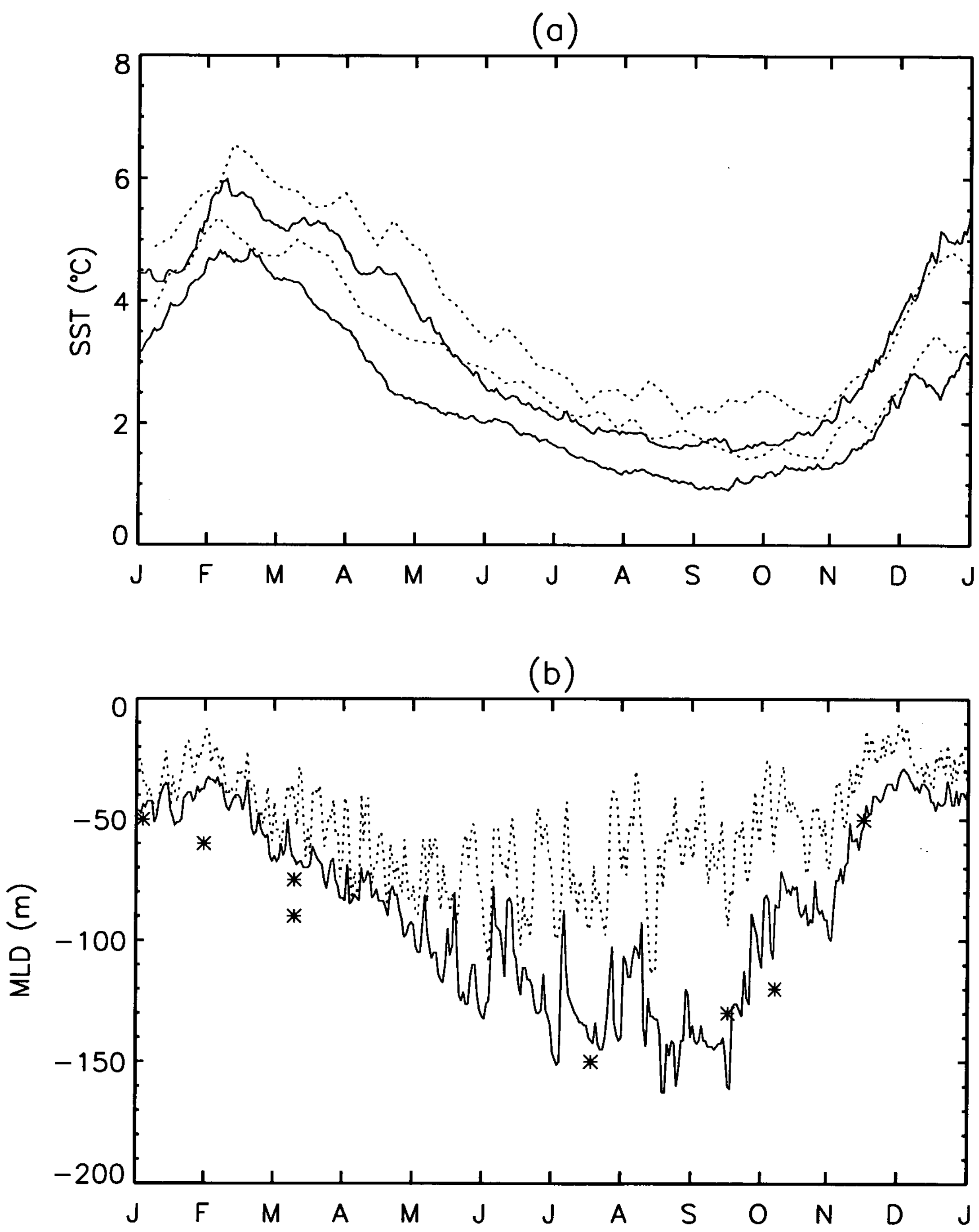

Figure 2.5. The daily SST and MLD in the PFZ. (a) Modelled SST+sd (upper solid line), SST–sd (lower solid line), the Reynolds SST+sd (upper dotted line) and the Reynolds SST–sd (lower dotted line). (b) The MLD (solid line), the Kraus depth (dotted line) and the observed MLD (✳) derived from the averaged MLD of 53–54°S from Rintoul and Trull (2001) and Parslow et al. (2001).

Figure 2.5b shows that there is clear seasonal pattern in the simulated MLD which was the shallowest in January–February (35 m) and deepest in August–September (160 m). In general, the modelled MLD was in agreement with the observation, in particular in July–January period. During the February–March period, the model simulation underpredicted the MLD by 10–20 m, which could be partially attributed to the interannual variability of 15 m in the simulation during this period (Figure 2.7). For the simulation, the Kraus depth closely tracked the MLD during the October–March period. Even during the March–November period, the Kraus depth was at least 50% of the MLD. This demonstrated that both wind stirring and shear instability played an important role in the upper ocean dynamics in the PFZ.

2.5.4 Sensitivity to the variability of the surface fluxes

To assess what surface fluxes are driving the daily to seasonal variability in the MLD, a series of experiments were carried out that used different combinations of the heat flux, freshwater flux and the wind stress from the four-year average or from the individual year of the NCEP data (Table 2.3). For each experiment, four runs were performed driven by the forcing fields described in Table 2.3. In the first three experiments, only one averaged variable was used and in the last three experiments, two averaged variables were used. The first three experiments were used to identify the variable that was dominating the variability in the MLD. The last three were used to identify the least important variable. To analyze these experiments, we compared the seasonally varying mean MLD and standard deviation (SD) from the four runs of each experiment to the corresponding mean MLD and SD from the four runs of the control experiment performed in section 2.5.3.

Statistical analyses were applied to the model output to quantify the effects of the variability in the wind stress, the heat flux and the freshwater flux on the variability of the MLD. Three periods were examined: January–February when the MLD was the shallowest, July when sharp deepening occurred and October when sudden shoaling occurred. Three criteria were used to assess the sensitivity of the variability of the MLD to the surface forcing. The first one is the bias ($\overline{SD_s}$ – $\overline{SD_c}$) which is the difference of the means of the standard deviation (SD) between an experiment (s) and the control (c). The second is the correlation (r) between the SD_s and the SD_c. The last is the ratio of the variance of the SD_s to the variance of the SD_c:

$$\mathrm{Vs/Vc} = \frac{\frac{1}{n}\sum_{1}^{n}\left(SD_s-\overline{SD}_s\right)^2}{\frac{1}{n}\sum_{1}^{n}\left(SD_c-\overline{SD}_c\right)^2} \tag{2.19}$$

where n is the number of the simulations for each experiment. A perfect match is when the bias equals zero, and both the r and the Vs/Vc ratio equal one.

2.5.4.1 The SAZ region

Figure 2.6 shows the numerical simulations of the averaged MLD and the standard deviations of the MLD for the six experiments along with the control experiment in the SAZ. In general, the mean MLD showed similar patterns during the period of November – June in all the experiments, which was a slight shoaling from November to January and a moderately constant rate of deepening from February to June. During the November – June period, the standard deviations of the MLD were less than 30 m and nearly constant in all the experiments, which indicated that the interannual variability was small. During July - October period, the MLD was very deep (270-600 m), with large differences between the patterns of the

MLD and the standard deviation. The largest standard deviations were normally found in the early winter and late winter, which were associated with the rapid deepening or shoaling in the mixed layer. Based on the patterns of the MLD and the standard deviation in the winter, the experiments separate into two groups: the $\overline{W}H\overline{F}$, $WH\overline{F}$ and $\overline{W}HF$ showing three-step deepening with large standard deviation in the early winter, while the $W\overline{HF}$, $\overline{WHF}$ and $W\overline{H}F$ showing one-step sharp deepening with small standard deviation (Figure 2.6). In each group, only the heat flux was the same, which suggested that the heat flux was the key element in determining the seasonality of the MLD. Using averaged freshwater flux which was close to zero (eg. little freshening) in late winter, the model produced relative shallower winter MLD (Figures 2.6c and 2.6g). These indicated that the heat and freshwater fluxes caused deep winter convection and determined the depth of the mixed layer in the winter.

In the summer, the $W\overline{HF}$ experiment showed the closest standard deviation to that of the control experiment (Figure 2.6f), and the $WH\overline{F}$ experiment had the highest correlation (r = 0.92) with the control experiment (Table 2.4). These suggested that the variability in the wind stress was the major term driving the variability in the MLD, but the variability in the freshwater flux was not important. In the winter, the $\overline{W}HF$ experiment displayed most of the features for the control experiment and the $\overline{W}H\overline{F}$ experiment also showed a similar pattern for the standard deviation of the MLD (Figures 2.6l and 2.6d). This indicated that the wind stress was not important in driving the variability in the MLD, but the variability in the heat flux dominated the variability in the MLD (Table 2.4).

Table 2.3. Experiments to study the sensitivity of the model solution to forcing field.

Experiments	Model runs 1	2	3	4
(1) $\overline{WH}F$	$\overline{WH}F_1$	$\overline{WH}F_2$	$\overline{WH}F_3$	$\overline{WH}F_4$
(2) $\overline{W}H\overline{F}$	$\overline{W}H_1\overline{F}$	$\overline{W}H_2\overline{F}$	$\overline{W}H_3\overline{F}$	$\overline{W}H_4\overline{F}$
(3) $W\overline{HF}$	$W_1\overline{HF}$	$W_2\overline{HF}$	$W_3\overline{HF}$	$W_4\overline{HF}$
(4) $WH\overline{F}$	$W_1H_1\overline{F}$	$W_2H_2\overline{F}$	$W_3H_3\overline{F}$	$W_4H_4\overline{F}$
(5) $W\overline{H}F$	$W_1\overline{H}F_1$	$W_2\overline{H}F_2$	$W_3\overline{H}F_3$	$W_4\overline{H}F_4$
(6) $\overline{W}HF$	$\overline{W}H_1F_1$	$\overline{W}H_2F_2$	$\overline{W}H_3F_3$	$\overline{W}H_4F_4$

W, *H* and *F* refer to the wind stress, heat flux and freshwater flux, respectively.

Xi indicates the forcing variable from one of the four years data (i=1, 2, 3 or 4, referring the year 1995, 1996, 1997 or 1998, respectively).

$\overline{X} = \frac{1}{4}\sum_{i=1}^{4} X_i$, indicating four years average.

Table 2.4. Statistics (bias, correlation and Vs/Vc) for different periods. Bold numbers are the closest to the ideal values for bias, correlation and Vs/Vc in each group.

	SAZ			PFZ		
Experiment	Bias (m)	Correlation	Vs/Vc	Bias (m)	Correlation	Vs/Vc
		January-February				
(1) $\overline{WH}F$	11	-0.01	0.12	6	0.10	0.24
(2) $\overline{W}H\overline{F}$	8	**0.75**	0.30	5	-0.06	0.39
(3) $W\overline{HF}$	**4**	0.65	**0.47**	**0**	**0.35**	**0.71**
(4) $WH\overline{F}$	**-1**	**0.93**	**1.26**	**0**	**0.84**	**1.14**
(5) $W\overline{H}F$	5	0.73	0.60	**0**	0.57	0.77
(6) $\overline{W}HF$	8	0.65	0.38	4	0.04	0.61
		July				
(1) $\overline{WH}F$	200	-0.49	0.00	36	0.07	**0.25**
(2) $\overline{W}H\overline{F}$	**-14**	**0.94**	**0.98**	**30**	0.22	0.14
(3) $W\overline{HF}$	192	0.05	0.00	32	**0.35**	0.08
(4) $WH\overline{F}$	-7	0.92	**0.87**	**19**	0.60	**0.95**
(5) $W\overline{H}F$	146	-0.21	0.00	20	**0.78**	1.10
(6) $\overline{W}HF$	**-3**	**0.93**	1.24	21	0.48	0.54
		October				
(1) $\overline{WH}F$	165	0.28	0.45	4	-0.22	**2.84**
(2) $\overline{W}H\overline{F}$	**57**	**0.55**	**1.15**	-11	0.17	0.28
(3) $W\overline{HF}$	134	0.32	0.83	**-1**	**0.29**	3.88
(4) $WH\overline{F}$	46	0.68	0.80	**-1**	**0.77**	**1.26**
(5) $W\overline{H}F$	134	0.40	0.59	**-1**	0.34	4.70
(6) $\overline{W}HF$	**-4**	**0.90**	**1.07**	-9	0.44	0.10
Ideal	*0*	*1.00*	*1.00*	*0*	*1.00*	*1.00*

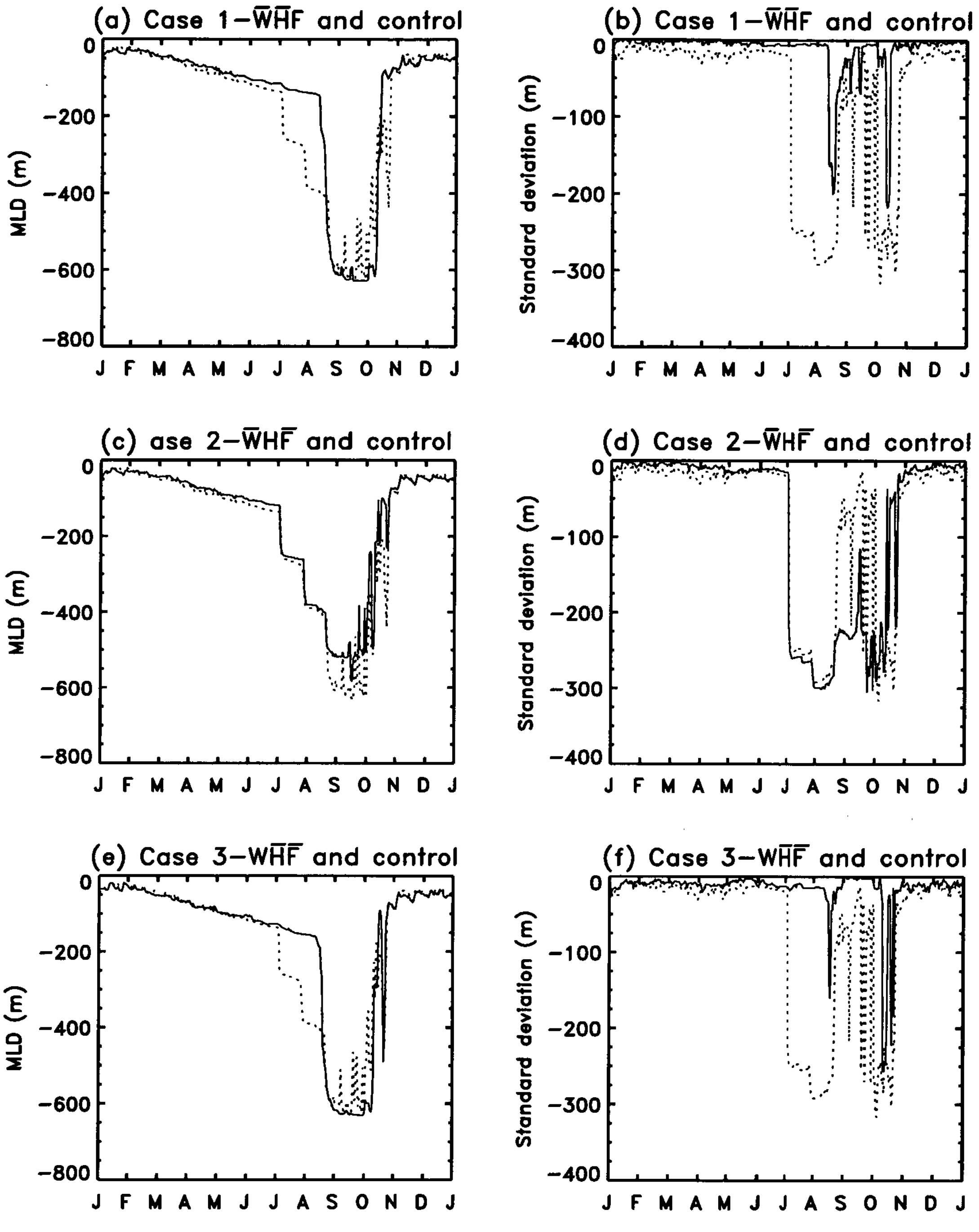

Figure 2.6. Daily means (left hand side) of the MLD calculated from four runs and the standard deviations (right hand side) in the SAZ. Solid lines are the results of the specific experiment, the dotted lines are those derived from the control experiment. The MLD is given as negative to indicate downwards from the surface (at the left). This convention has been also used for the standard deviation (at the right).

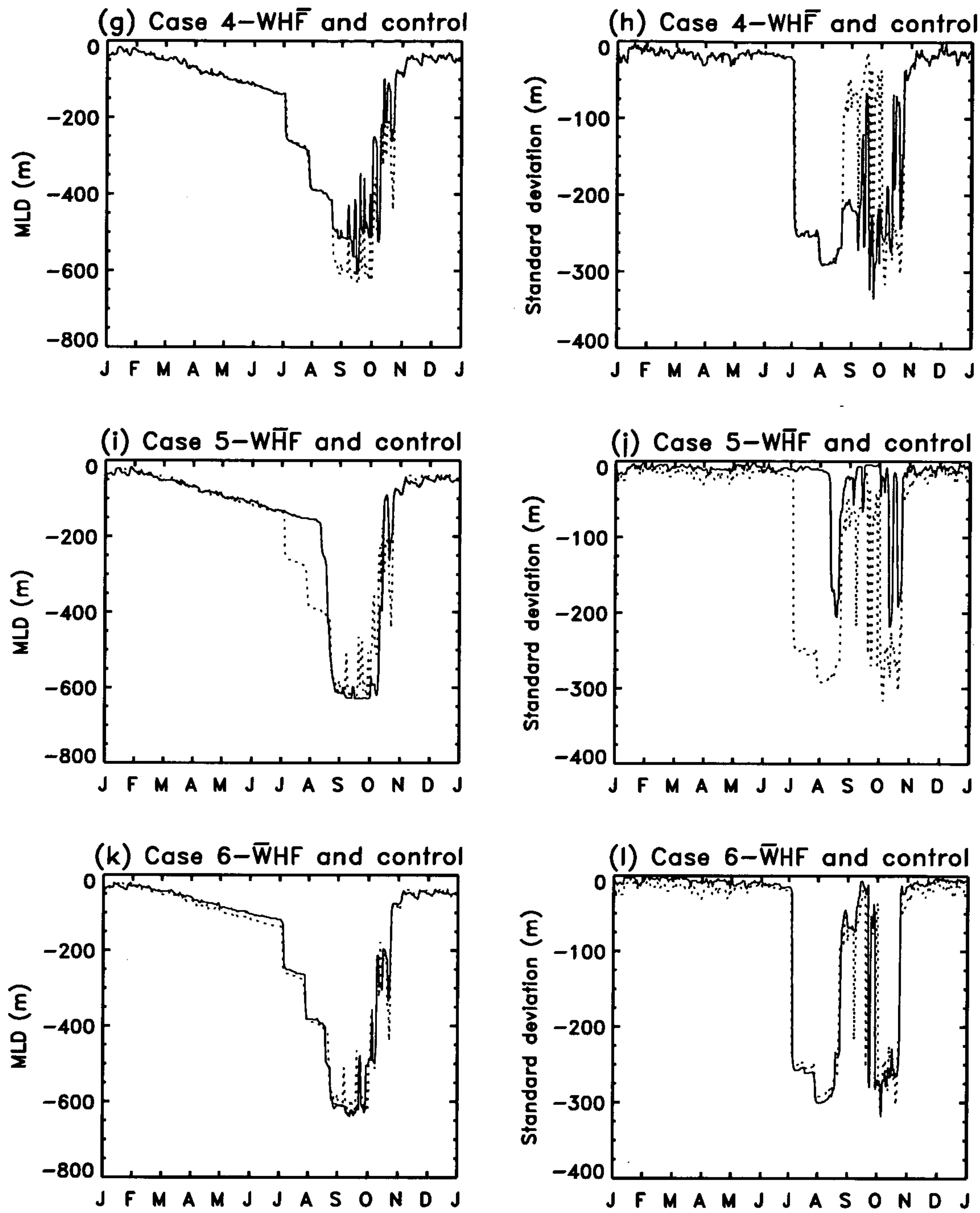

Figure 2.6. (continued)

2.5.4.2 The PFZ region

In general, using any averaged forcing fields in the PFZ, the model produced a deeper MLD than the control experiment in particular in the winter (Figure 2.7). In the control experiment, the standard deviation of the MLD showed a similar pattern to the MLD, increasing from February to August and decreasing from August to November. In the summer, the standard deviations of the MLD in the $W\overline{HF}$, the $WH\overline{F}$ and the $W\overline{H}F$ experiments closely tracked that in the control experiment (Figure 2.7f, 2.7h and 2.7j). Statistical analyses indicated that the variability in the MLD was mainly due to the variability in the wind stress, and the variability in the heat flux and the freshwater flux had little effect on the variability in the MLD (Table 2.4). In July, there was no single variable explaining more than 50% of the variance (Table 2.4), and the bias was relatively large (19 to 36 m) in all the experiments. Similarly, it is hard to identify which variable was important in driving the variability in the MLD in October although the wind stress had two out of three criteria close to the ideal values. These reflect complex interaction of the variability in the surface fluxes in driving the variability in the MLD.

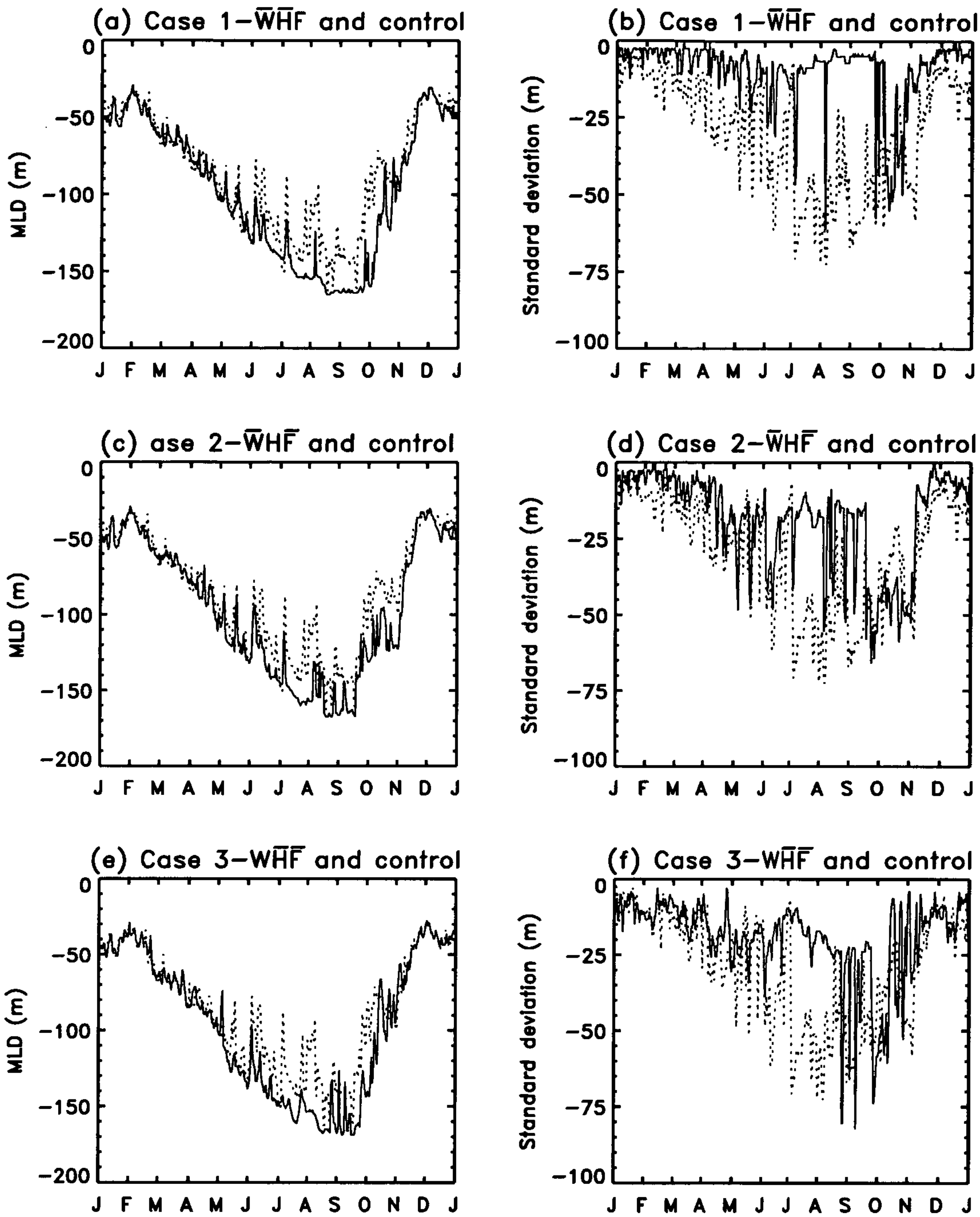

Figure 2.7. Daily means (left hand side) of the MLD calculated from four runs and the standard deviations (right hand side) in the PFZ. Solid lines are the results of the specific experiment, the dotted lines are those derived from the control experiment. The MLD is given as negative to indicate downwards from the surface (at the left). This convention has been also used for the standard deviation (at the right).

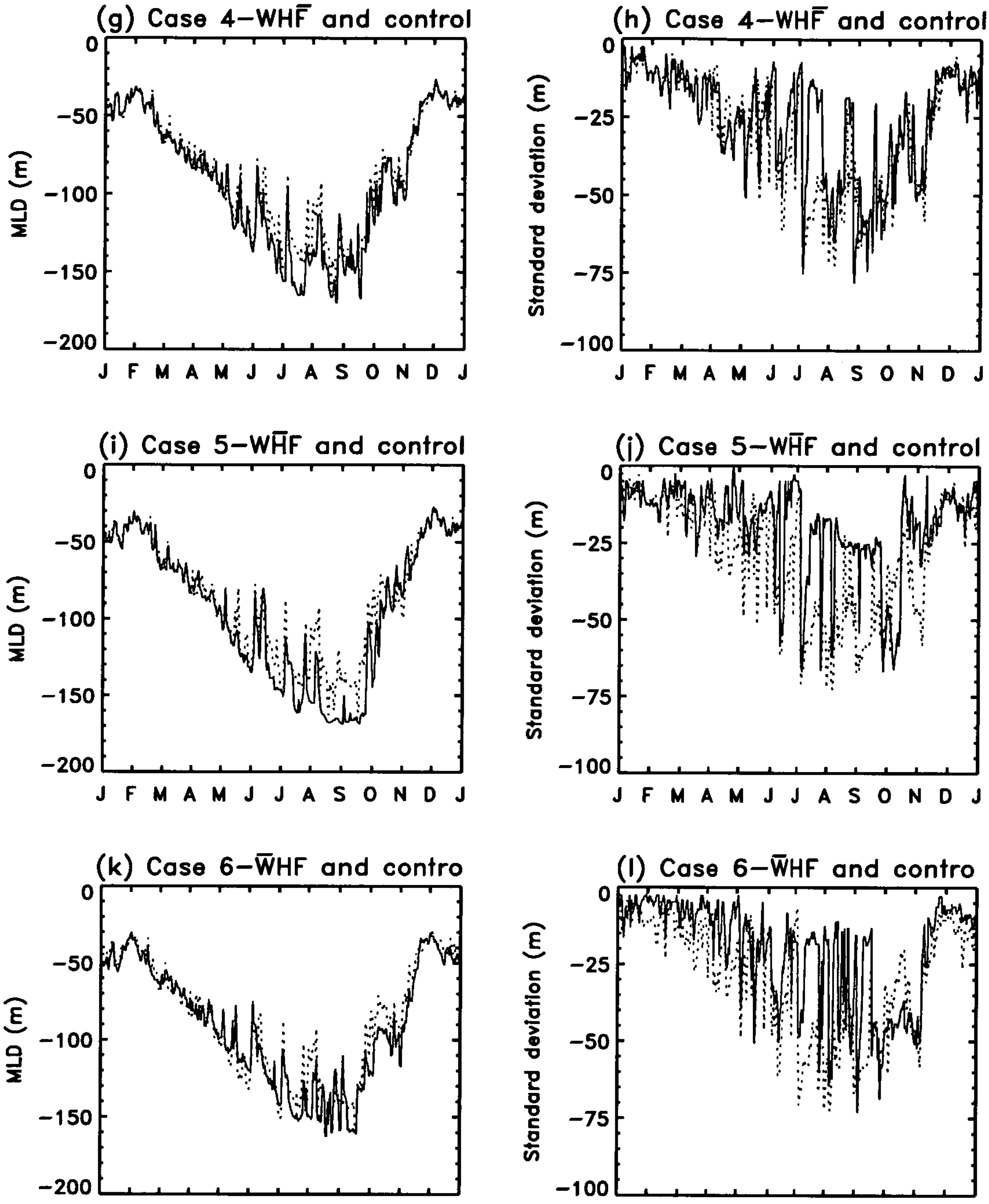

Figure 2.7. (continued)

2.6 Discussion and summary

Previous studies demonstrated that 1D mixed layer models could successfully predict the changes of the SST and the MLD in the ocean where there was no strong horizontal transport (Chen et al., 1994; Large et al., 1994; Kantha and Clayson, 1994; Anderson and Weller, 1996; Godfrey and Schiller, 1997). In the region where advection is important such as at the Bermuda Atlantic Time-Series Study site, it is necessary to add an advective correction in the heat and salt to the 1D model (Doney, 1996). This study demonstrates that the Chen and the KPP produce almost identical seasonality of the SST and MLD in the SAZ, which are consistent with the observations. In the current study, without the advective correction for the heat and freshwater fluxes in the SAZ, the Chen scheme was capable of reproducing the seasonal cycle of the MLD and the annual amplitude of the SST for most of the years. This indicates that the advection is not important in the SAZ. In the PFZ and the SAZ, with the proper advective corrections for the heat and freshwater fluxes, the Chen scheme successfully reproduced the seasonality of the SST and the MLD. The maximum MLD of 600 m produced in SAZ by the 1D model was consistent with the observation, but much greater than 200 m found by Häkkinen (1995). The annual SST amplitude was 4.0 °C for the PFZ in this model, which was consistent with the Reynolds SST amplitude (4.1 °C), but larger than Markus [1999] value of (2.5 °C). Our more realistic SST and MLD in the SAZ and the PFZ reflected the importance of including both the wind mixing and the shear instability in the simulation in this region.

This study indicated that vertical mixing processes were similar in the summer in both the SAZ and the PFZ. In particular the wind mixing was the dominant process

(Table 2.4) when the ocean gained heat, the top layer became less dense and more stable. Under this stable condition, the heat influx tended to reduce the mixed layer depth while the influence of the wind deepened the mixed layer depth. The averaged MLD was about 30 m in the SAZ, and 40 m in the PFZ for the January – February period. The shallower summer MLD in the SAZ could be explained by the lower wind stress in the SAZ than the PFZ.

In the winter, the pattern of the MLD and the mechanism of the mixing were very different between the SAZ and the PFZ. The maximum MLD was significantly shallower in the PFZ (160 m) than in the SAZ (600 m) although the winter wind stress was generally higher in the PFZ than in the SAZ. There were no signals of sharp deepening in the MLD in the winter or sudden shoaling in the spring in the PFZ, which was markedly different from the SAZ. In the SAZ, cooling was the dominant process driving the timing of the deep winter mixed layer. Freshening played an important role in determining the depth of the winter MLD, in particular in September – October period when the MLD was shoaling in the SAZ. The PFZ largely differed from the SAZ, showing lack of deep convection and little effect of the freshwater flux on the variability in the MLD. Wind stirring played an important role in determining the MLD in the PFZ in both the winter and the summer.

Our 1D model underpredicted the MLD by 10 to 20 m in summer in the SAZ and the PFZ which could be partially explained by the interannual variability (5 to 15 m). The potential bias in the NCEP forcing may further explain this difference. For example, the NCEP data may contain error (20 – 50 %) in the wind stress (Budd and Schiller pers. comm.). Using five days (7 to 12 March 1998) wind speed recorded by au9706 in the SAZ, we estimated that the wind stress in the NCEP data is about 60 % of the observation. Since the wind stirring is the dominant process driving the vertical mixing in the summer in both the SAZ and the PFZ, we expect that the summer mixed layer will deepen if the wind stress is increased. Increased wind stress during the winter would not affect the winter MLD in the SAZ but may influence the winter MLD in the PFZ.

Numerical simulations indicated that doubling the wind stress could result a deep MLD (300 m) in mid-latitude (50 °S) in the Southern Ocean (Ribbe, 1999). However, in the real ocean, it could not be possible to create a deep MLD of 600 m by wind stirring. To examine the reason for the lack of deep convection in the PFZ, we initialized the model with the winter profiles of temperature and salinity from the PFZ and forced the model with the NCEP data from the SAZ. This simulation produced a seasonal MLD evolution that was similar to the control experiment in the PFZ, which indicated that the surface forcing can not explain the large difference in the winter mixed layer between the SAZ and the PFZ. The difference in the winter mixed layer must be due to the stratification. The SAZ is weakly stratified but the PFZ is strongly stratified. There was a large density gradient (27.3 to 27.9) in the upper 1000 m of the PFZ in winter (Rintoul and Bullister, 1999), suggesting that there was little possibility to generate a deep mixed layer of 500 m in this region.

Chapter 3. Simulation of the upper ocean dynamics: II. The seasonal phosphate export and resupply

Paper in press in Journal of Geophysical Research, 2001:

Modeling seasonal phosphate export and resupply in the Subantarctic and Polar Frontal Zones in the Australian sector of the Southern Ocean

Xiujun Wang[1,2], Richard J. Matear[1,3], and Thomas W. Trull[1]

1. Antarctic CRC, University of Tasmania, GPO Box 252-80, Hobart, 7001, Tasmania, Australia.
2. Institute of Antarctic and Southern Ocean Studies, University of Tasmania, GPO Box 252-77, Hobart, 7001, Tasmania, Australia.
3. CSIRO Division of Marine Research, GPO Box 1538, Hobart, 7001, Tasmania, Australia.

3.1 Abstract

We developed and applied a one-dimensional (z) biophysical model to the Subantarctic Zone (SAZ) and the Polar Frontal Zone (PFZ) to simulate seasonal phosphate export production and resupply. The physical component of our model was capable of reproducing the observed seasonal amplitude of sea surface temperature and mixed layer depth. In the biological component of the model we used incident light, mixed layer depth, phosphate availability and estimates of phytoplankton biomass from the Sea-viewing Wide Field-of-view Sensor to determine production, and tuned the model to reproduce the observed seasonal cycle of phosphate. We carried out a series of sensitivity studies, taking into account uncertainties in both physical fields and biological formulations (including potential influence of iron limitation), which led to several robust conclusions (as represented by the ranges below). The major growing season contributed 66 – 76% of the annual export production in both regions. The simulated annual export production was significantly higher in the PFZ (68 – 83 mmol P m^{-2}) than in the SAZ (52 – 61 mmol P m^{-2}) despite the PFZ having lower seasonal nutrient depletion. The higher export production in the PFZ was due to its greater resupply of phosphate to the upper ocean during the September to March period (27 – 37 mmol P m^{-2}) relative to that in the SAZ (8 – 15 mmol P m^{-2}). Hence seasonal nutrient depletion was a better estimate of seasonal export production in the SAZ, as demonstrated by its higher ratio of seasonal depletion/export (64 – 78%) relative to that in the PFZ (34 – 47%). In the SAZ, vertical mixing was the dominant mechanism for supplying phosphate to the euphotic zone whereas in the PFZ, vertical mixing supplied only 37% of the phosphate to the euphotic zone and horizontal transport supplied the remaining 63%.

3.2 Introduction

The "biological pump" involves the photosynthetic production of organic matter from carbon and nutrients in surface waters and the subsequent transport of this organic matter into the ocean interior. This export production lowers the concentration of total dissolved carbon in surface waters and enables more carbon to be transferred from the atmosphere and stored in the ocean. The Southern Ocean (between the Antarctic continent and the Subtropical Convergence) is an important region for uptake of atmospheric carbon dioxide (CO_2) (Takahashi et al., 1997; Metzl et al., 1999). In addition, modeling studies suggest the region is likely to respond strongly to climate warming, including possible changes in export production (Sarmiento and Le Quere, 1996; Matear and Hirst, 1999; Bopp et al., 2001). Thus it is essential to determine present export production accurately.

As recently reviewed by Priddle et al. (1998) and reiterated in a JGOFS Southern Ocean Synthesis Group report (Bathmann, 2000), the present magnitude of export production in the Southern Ocean is a matter of debate. Low estimates of export production were obtained when they were based on predator carbon demand (Priddle et al., 1998), or seasonal nutrient depletion of surface waters (Lourey and Trull, 2001). But more than double the value of export production was obtained from three-dimensional assimilation of tracers (Schlitzer, 2001). The discrepancy between the different methods may reflect their inherent limitations. For example, the predator-demand method assumes only ~10% of primary production escapes the food web and is lost directly (Priddle et al., 1998). This fraction may be too low if direct sedimentation of algae to depth is an important occurrence in the Southern Ocean (Ditullio et al., 2000; Boyd and Newton, 1999). Seasonal nutrient depletion in surface waters always provides a minimum estimate of export production because any export outside the stratified period or resupply during it is ignored. Recent studies have assumed that these effects are small (Karl et al., 1991; Hoppema et al., 1995; Ishii et al., 1998; Rubin et al., 1998; Metzl et al., 1999; Sweeney et al., 2000a; Sweeney et al., 2000b; Lourey and Trull, 2001), but this has not been assessed quantitatively.

In this paper, we focus on quantifying nutrient resupply to the euphotic zone and assessing its importance to estimates of export production from seasonal nutrient depletion in surface waters. To accomplish this, we use a one-dimensional (1-D) biophysical model, which combines a mixed layer model with a new production model. Similar 1-D biophysical models have been applied at sites in the North Atlantic (Doney et al., 1996), North Pacific (Denman and Peña, 1999) and the Southern Ocean (Louanchi et al., 1996; Louanchi et al., 1999). We use a new production model along with phytoplankton biomass estimated from the Sea-viewing Wide Field-of-view Sensor (SeaWiFS) data to compute the biological uptake of nutrients. The 1-D mixed layer model then calculates the nutrient resupply to the euphotic zone. We do not attempt to simulate the details of ecosystem structural controls on either new or export production because limited data exist concerning probable key factors such as iron availability or zooplankton grazing. Instead we scale the magnitude of new production so that the model reproduces the observed seasonal nutrient depletion. In other words, we assimilate data that constrains both new production (from SeaWiFS biomass), and the sum of export and resupply (from the seasonal changes in nutrient concentrations). The 1-D model then allows us to partition the seasonal nutrient depletion into contributions from export production and from resupply. This approach replaces the uncertainties of more complex export production models by assimilating data, but it still retains some assumptions that are important to the nutrient resupply estimates. These include the possibility of delay between new and export production, the efficiency and depth profile for remineralization of organic matter, possible limitation by iron availability, and other factors. We address these issues via sensitivity studies, and show that they introduce relatively small uncertainties in our resupply estimates.

We focus on the Subantarctic Zone (SAZ) and the Polar Frontal Zone (PFZ) because these zones are important sinks for atmospheric CO_2 (Poisson et al., 1993; Metzl et al., 1999). Furthermore it is uncertain which of these two regions exports more carbon to depth. Using the seasonal nutrient depletion method, Lourey and Trull (2001) estimated that the export production was much greater in the SAZ (3.4 mol C m^{-2}) than in the PFZ (1.4 mol C m^{-2}). Conversely, mesopelagic suspended barium concentrations suggest that the PFZ is the greater carbon export region (Cardinal et al., 2001). Trull et al. (2001b) found that the total mass export from sediment trap was much greater in the PFZ than in the SAZ for the 800-1000 m depth range during September to February, but that particulate organic carbon was less in the PFZ than in the SAZ. In this study, we try to answer the question of which region has greater export production, using a different approach: a simple 1-D biophysical model.

In summary, the objectives of this study are (1) to quantify the export production in the minor growing season (i.e. between March and September) when the seasonal depletion approach is not applicable; (2) to determine the nutrient input to the euphotic zone in the major growing season (i.e. between September and March), and (3) to compare the export production and the phosphate resupply in the SAZ with the PFZ.

3.3 Model description and observational data

A 1-D biophysical model was developed to simulate phosphate export and resupply in the upper ocean in the SAZ and in the PFZ. The rate of change for phosphate P at any depth z in the model is given by:

$$\frac{dP}{dt} = \frac{d}{dz}\left(K_z \frac{dP}{dz}\right) + Q \qquad (3.1)$$

where Kz (vertical mixing coefficient) is calculated by a mixed layer model and the Q is the source term calculated by a new production model.

3.3.1 Mixed layer model

We used a model, hereafter referred to as the Chen scheme (Chen et al., 1994), which combines the Kraus-Turner bulk mixed layer model (Kraus and Turner, 1967) and Price's dynamical instability model (Price et al., 1986). However, we replaced the use of the Price et al. formulation for the Richardson number by the formulation of Pacanowski and Philander (1981) (as explained in Chapter 2) to calculate the diffusivity and viscosity. The model successfully simulates the seasonal amplitudes of the sea surface temperature (SST) and the mixed layer depth (MLD) in the SAZ and the PFZ. In brief, the model was forced with the surface fluxes of heat and fresh water and the wind stress from the National Centers for Environmental Prediction (NCEP) (Kalnay et al., 1996), and initialized with winter profiles of temperature and salinity from observations. The initial profiles of phosphate were taken from Niskin bottle data from *Aurora Australis* cruise AU9501 (Rosenberg et al., 1997). Velocity profiles were initialized to zero at all depths because a test run initialized with a previous run's winter velocity profile showed little effect on the model solution. The model domain was 0 –1000 m, with a uniform vertical grid spacing of 5 m depth. The model bottom boundary was closed so that diffusive fluxes were not allowed through this boundary.

3.3.2 New production model

A new production model was implemented in the 1-D mixed layer model to simulate the phosphate utilization in the euphotic zone (the model parameters are listed in Table 3.1).

Table 3.1. The parameters of the biological model.

Parameter	Symbol	Value	Units	Reference
Initial slope of P-I curve	α	0.025	$(W\ m^{-2}\ d)^{-1}$	Clementson et al. (2000)
Photos. active fraction	PAR	0.5		Clementson et al. (2000)
Half saturation constant	K	0.1	μM P	Matear and Hirst (1999)
Light atten. cons. phytoplankton	k_c	0.06	$m^{-1}\ (\mu M)^{-1}$	Matear (1995)
Light atten. cons. water	k_w	0.04	m^{-1}	Matear (1995)
Carbon to phosphate ratio	C:P	122		Six and Maier-Reimer (1996)
Euphotic zone	z_e	75	m	Griffiths et al. (1999)
Carbon to chl *a* ratio	C/chl	75	g:g	Arrigo et al (1998)

The daily new production in the mixed layer was specified as

$$Q = \sigma(t, H)\, P_o \frac{p}{K + p}\, R \tag{3.2}$$

where p is the phosphate concentration in the MLD, K is the half saturation constant for phosphate uptake, R is a scaling factor tuned by approximately matching the simulated seasonal draw-down in surface phosphate to shipboard observations, P_o is the phytoplankton biomass given as a phosphate concentration, and σ represents the control of algal growth by light and temperature.

P_o is estimated from the monthly SeaWiFS *Chl a*, as defined below:

$$P_o = Chl\, \frac{C}{Chl}\, \frac{1}{12(C\!:\!P)} \tag{3.3}$$

where *C/Chl* is the carbon to *Chl a* ratio (gram:gram) and C:P the Redfield ratio of carbon to phosphate. It was assumed that *Chl a* concentration was uniform within the euphotic zone.

For the daily averaged algal growth in the MLD, we used the formulation of Matear (1995):

$$\sigma(t, H) = 2\, \frac{1}{H} \int_0^l \int_0^H F(I)\, dz\, dt \tag{3.4}$$

where t is the time (day of the year), l is the half day length, and H is the MLD or the depth of the euphotic zone (z_e), whichever was shallower. The light and temperature dependency of algal growth F was specified as follows:

$$F(I) = \frac{V(T)\alpha I(z,t)}{(V(T)^2 + \alpha^2 I(z,t)^2)^{1/2}} \tag{3.5}$$

where α is the initial slope of the primary production vs irradiance (P-I) curve, and V is the maximum growth rate as $I \rightarrow \infty$, which was dependent on temperature (°C, Eppley, 1972):

$$V(T) = 0.6(1.066)^T \tag{3.6}$$

Light intensity at depth was given by

$$I(z,t) = PAR\ I(0,t)\exp(-(k_w + k_C P_o)z) \tag{3.7}$$

where PAR is the photosynthetically active fraction of total insolation, and k_w and k_c are the light attenuation constants for water and phytoplankton. The solar insolation, $I(0,t)$ was obtained from NCEP data (Figure 3.1).

With this formulation, the seasonal value of new production, Q, is primarily controlled by σ, and P_o, because R is constant, and in the nutrient-rich SAZ and PFZ, the term $p/(K+p)$ varies only slightly, between 0.89 and 0.95. As shown in Figure 3.1, σ depends largely on the seasonal solar insolation. This Q formulation is, of course, incomplete. In particular, iron availability may limit new production in this region (Sedwick et al., 1999). Insufficient iron data precludes an iron-based model, but an indicative test of the effect of iron limitation is possible by imposing a seasonal change in the $p/(K+p)$ term independently of the phosphate concentration. We investigate this possibility as one aspect of our model sensitivity studies below.

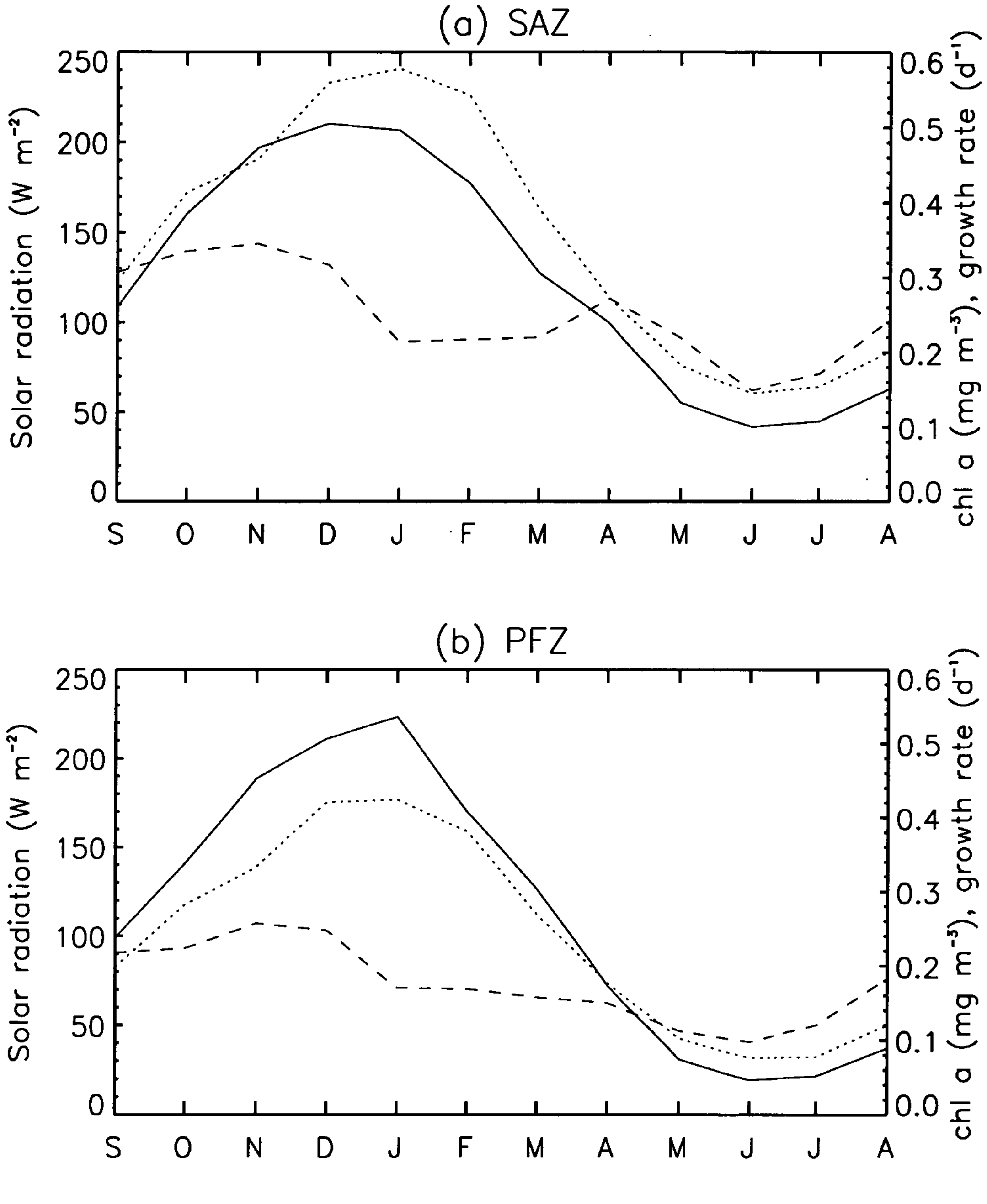

Figure 3.1. The seasonal characteristics of the new production model: the monthly SeaWiFS *Chl a* concentration (1997 – 1998, dashed line), the algal growth rate (σ term, dotted line) and solar radiation (solid line) in the (a) SAZ and (b) PFZ.

The new production, calculated as Q, was assumed to be exported from the upper layer and instantaneously remineralized below the euphotic zone. This approach effectively equates the magnitudes of the new production and the export production. However, sensitivity tests in our model indicated that up to one-month delay between phytosynthetic uptake and remineralization had little effect on the magnitude of seasonal new production or nutrient resupply, justifying this approach for the purpose of estimating nutrient resupply. However, because the model includes no ecosystem structure other than new production, the seasonal timing of export production has limited validity.

Following Williams and Follows (1998), remineralization is assumed to decrease exponentially with depth:

$$P_r(z) = \exp^{-\frac{z-z_e}{z^*}} \tag{3.8}$$

where z* is the scale length for the remineralization and is set to 400 m. The equation allows 10% of the new production produced in the euphotic zone to reach 1000 m. This fraction is slightly less than what is predicted by Martin et al. (1987) using their power law function (13%), but much greater than what Trull et al. (2001b) reported (2–3%) from sediment trap collections in the Southern Ocean. In our model, this fraction of the new production is remineralized in the bottom layer (1000 m).

In the implementation of the new production model, we assumed that the primary production was equal to the remineralization between the base of the mixed layer and the base of the euphotic zone, i.e., that there was no new production beneath the mixed layer. This assumption might underestimate export production when the MLD is much shallower than the euphotic zone. The shallowest MLD was found during December to February in both the SAZ and the PFZ (Figures 3.2 and 3.3). In a sensitivity study, we assumed the σ term below the mixed layer was 20% of that in the mixed layer, and found that it did not change the modeled phosphate seasonal cycle. However, it did decrease the scaling factor by about 16% in the SAZ and 10% in the PFZ. Sensitivity tests revealed that changing the scaling factor affected the magnitude of export production, but did not change the seasonal depletion/export ratio by more than 10% (see below).

3.3.3 Observational data and comparison procedures

The MLD and SST observations were obtained from XBT data taken as part of an ongoing program of repeat sections carried out from the French Antarctic resupply ship l'Astrolabe (Rintoul et al., 2001). We defined the observed MLD as the depth where the temperature decreased by 0.2°C from the 10 m value (equivalent to density difference of ~0.04 in the observations), whereas the simulated MLD was defined as the depth where the density increased 0.02 from the surface. We chose a density criteria to define the model MLD because it is more representative of the MLD than either a temperature or salinity defined MLD. The MLD criteria in the model (0.02 difference in the density) was guided by the profile of vertical diffusion (Kz) and was approximately equal to the depth where the Kz first changed to the background value. We used a temperature change corresponding to a slightly larger density change for defining the MLD in the XBT data because the observed vertical profiles were more variable than in the model.

The seasonal phosphate cycle was compiled from bottle data from the *Aurora Australis and Southern Survey* cruises' during 1991 – 1998 period (see references in Griffiths et al., 1999; Lourey and Trull, 2001). The data were corrected for the interannual variability in the horizontal transport by using the winter (July 1995) salinity-phosphate relationship reported by Lourey and Trull (2001). In the model simulations, phosphate depletion (ND) in a particular period was calculated by subtracting the phosphate concentration from the first day to the last day and integrated for the euphotic zone (0 – 75 m):

$$ND = \int_{z=0}^{z=75} \int_{t=a}^{t=b} [P(t,z) - P(a,z)] dt \, dz \qquad (3.9)$$

This calculation produces less depletion than that estimated by Lourey and Trull [2001], who calculated to the maximum depth of depletion as determined by comparison of winter and summer profiles (approximately 100 m in the SAZ and the PFZ). Simulated phosphate resupply was calculated by subtracting the simulated depletion from the simulated phosphate export from the euphotic zone for that period.

3.4. Model Results

For the standard simulation, seasonal MLD, SST and phosphate concentration were simulated for the period of 1st September 1994 to 31st December 1995. Two sites were examined: the SAZ represented by data from 47°S, 142°E, and the PFZ represented by data from 54°S 140°E. These are the two locations of *the SAZ Project* sediment trap moorings (Trull et al., 2001b), and they characterize the central Subantarctic Zone and the southern limit of the Polar Frontal Zone. Because no SeaWiFS *Chl a* data are available for 1994 – 1995 period, the standard simulation combined the 1994 - 1995 physical forcing with the 1997 - 1998 biomass estimates. The results of the standard simulation are discussed first, followed by examination of the sensitivity of the results to variations in model parameters and interannual variations in forcing.

3.4.1 The SAZ region

The standard simulation for the SAZ predicted a very deep winter MLD (> 600 m) which lasted from July to September (Figure 3.2). The shallowest MLD was found in December – February (< 50 m) in the simulation, and showed a good agreement with the observations. The simulation also successfully predicted the observed seasonal amplitudes in the SST. The model generally reproduced the seasonal pattern of phosphate depletion without a progressive enrichment or depletion of surface waters on interannual timescales (Figure 3.2). However, there were some differences in the details of the seasonal phosphate cycle, for example the simulation suggested lower than observed phosphate concentrations in November and December 1995 (Figure 3.2). It is difficult to assess whether this represents an overestimate of spring export at that time by the model, or reflects interannual variations in the observations.

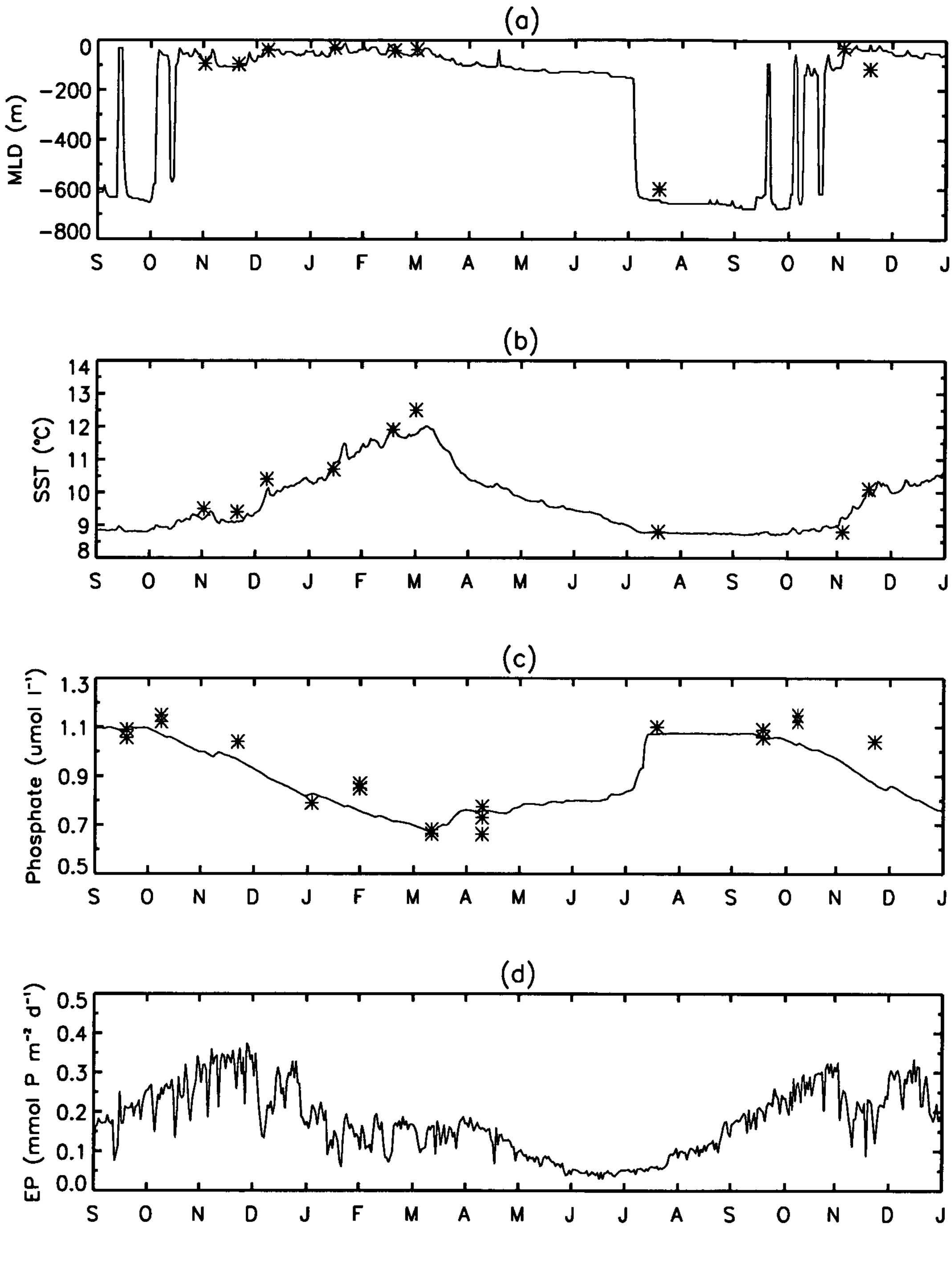

Figure 3.2. The SAZ simulation of (a) daily mixed layer depth (MLD), (b) SST, (c) phosphate concentration, and (d) export production (EP), showing the standard model results (September 1994 to December 1995, solid line) and the observed data (1991-1998, ✳).

Table 3.2. Seasonal phosphate export, depletion and resupply in the euphotic zone

Phosphate ($mmol/m^2$)	SON	DJF	MAM	JJA
		----- SAZ -----		
Export	22.4	16.6	11.0	6.7
Depletion	12.1	15.4	- 5.2	-20.3
Resupply_z*	10.3	1.2	16.2	27.0
Depletion/export (%)	54	92		
		----- PFZ -----		
Export	28.4	24.2	14.4	6.8
Depletion	12.7	9.3	-9.8	-6.6
Resupply_z	5.9	2.5	10.6	6.0
Resupply_y**	9.9	12.3	13.6	7.4
Depletion/export (%)	44	39		

* Resupply_z indicates the phosphate resupplied by the vertical mixing.

**Resupply_y indicates the phosphate resupplied by the horizontal transport.

As shown in Figure 3.2, daily phosphate export was estimated to range from 0.05 to 0.35 mmol m^{-2} d^{-1} (equivalent to 6 - 42 mmol C m^{-2} d^{-1}, using a C:P ratio of 122). The "noisy' structure of the export production reflects the high variability of the MLD. The annual phosphate export was 56.7 mmol m^{-2} (equivalent to 6.9 mol C m^{-2}) from September 1994 to September 1995. It was highest in the spring season and the lowest in the winter season (Table 3.2). The phosphate depletion was slightly greater in the summer (15.4 mmol m^{-2}) than in the spring (12.1 mmol m^{-2}) while the phosphate resupply was much greater in the spring (10.3 mmol m^{-2}) than in the summer (1.2 mmol m^{-2}). In the minor growing season, the phosphate export production contributed 31% of the annual total export (17.6 mmol m^{-2}). During the major growing season, the vertical mixing transferred 11.5 mmol m^{-2} phosphate to the euphotic zone from below, which accounts for 29% of the export for that period.

3.4.2 The PFZ region

As discussed in Wang and Matear (2001), at the PFZ site the 1-D simulation produced a drift to higher temperatures and lower salinities in the annual simulation. The drift in the model reflects the omission of the northward Ekman transport of cold salty water. With the inclusion of Ekman transport we can close the heat and freshwater budgets at this site and reproduce the observed seasonal MLD and SST amplitudes.

At the PFZ site, the model produced a relatively shallow winter MLD (160 m) in comparison to the SAZ, which was consistent with observations. The shallow winter MLD prevents the most of the exported phosphate from returning to the euphotic zone by vertical mixing in winter (more than 80% is remineralized below

160 m depth). Thus our model's the euphotic zone becomes depleted in phosphate during the simulation. Yet this is not observed. There are two possible explanations for the euphotic zone phosphate depletion: (1) remineralization in the PFZ may have a much shorter length scale than what we specify in our model, or (2) 1-D simulation misses an essential aspect of nutrient supply to PFZ surface waters.

Guided by how we closed the heat and freshwater budgets (Wang and Matear, 2001), we assumed that Ekman transport also played an important role in maintaining the new production and phosphate level in the euphotic zone in the PFZ. In simulating the phosphate, we applied an advective adjustment to the Kraus layer (wind-mixed layer) using

$$F(t) = \overline{F}\ \frac{\tau_x(t)}{\overline{\tau}_x} \tag{3.10}$$

where $F(t)$ is the advective adjustment for the phosphate concentration at time t, $\overline{F}$ is the annual mean adjustment required to maintain the phosphate concentration in the MLD in the following winter at the previous winter level, $\tau_{x(t)}$ is the eastward wind stress at time t, $\overline{\tau}_x$ is the four-year (1995-1998) averaged eastward wind stress. $\overline{F}$ was estimated by running the biophysical model without the advective adjustment and using the simulated phosphate depletion in the mixed layer in the following winter to determine the necessary amount of phosphate needed to restore the concentrations to the previous winter value.

Figure 3.3 presents the daily MLD, SST, phosphate concentration and export production from the model along with the observations. The model successfully reproduced the observed seasonal pattern and annual amplitude of the SST and MLD. The seasonal amplitude of the phosphate concentration in the PFZ (0.3 mmol m^{-3}) was slightly less than in the SAZ (0.4 mmol m^{-3}). The seasonal pattern of the phosphate export was similar to the SAZ, but the magnitude was higher than the SAZ for most of the year. The PFZ annual export production was 73.8 mmol m^{-2} for the period of September 1994 to September 1995, compared with 56.7 mmol m^{-2} in the SAZ (Table 3.2, the sums of the four seasons).

Table 3.2 indicates that in the minor growing season, the phosphate export contributed 29% of the annual total export (21.2 mmol m^{-2}). In the spring, the phosphate depletion was similar in both the SAZ and the PFZ. In the summer, the PFZ showed significantly less depletion (9.3 mmol m^{-2}) than the SAZ (15.4 mmol m^{-2}). From September to March, the phosphate depletion was 22 mmol P m^{-2} in the PFZ, which was equivalent to 42% of the export production. On an annual basis, vertical mixing provided 37% of the phosphate resupply into euphotic zone and horizontal transport provided 63%.

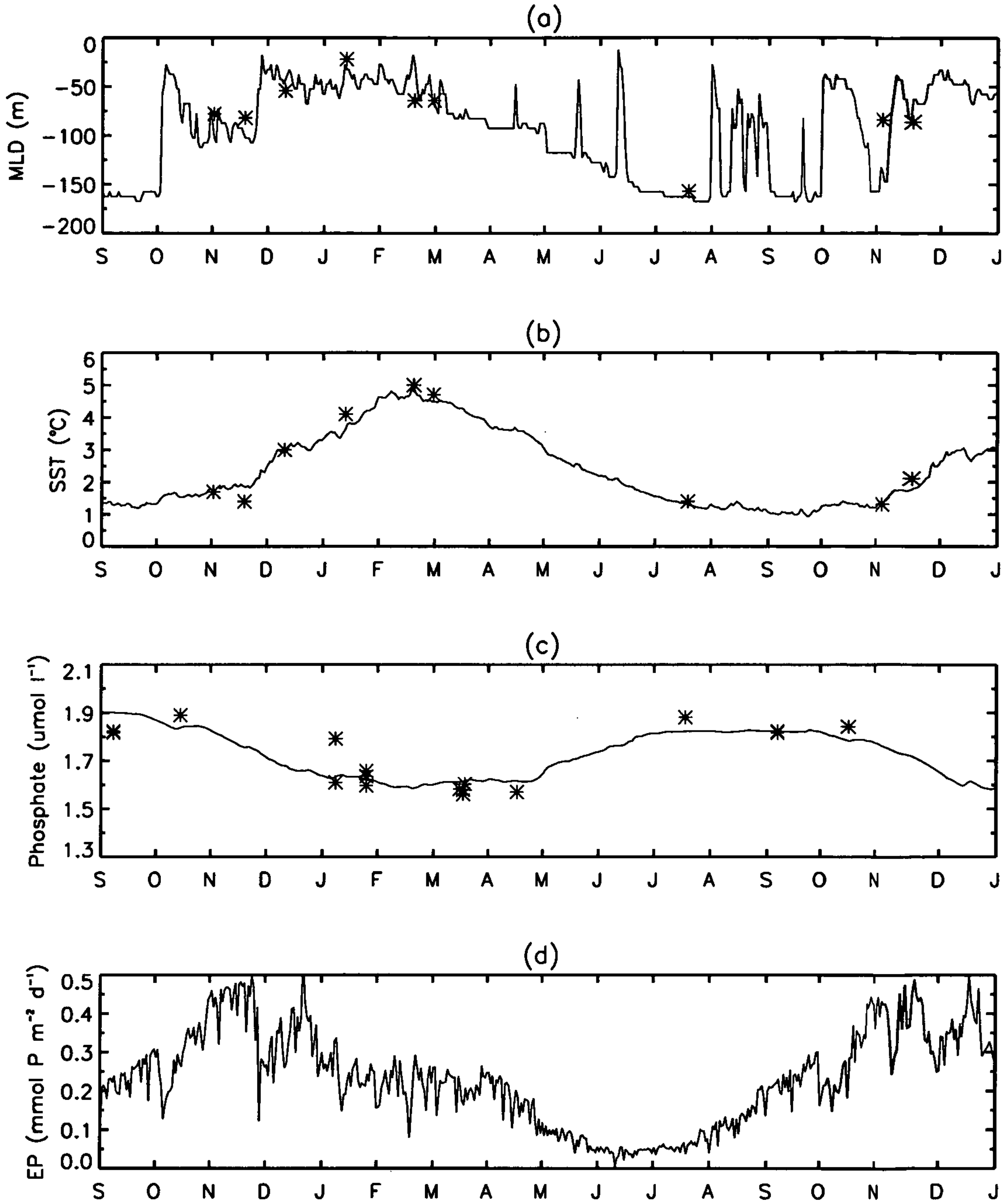

Figure 3.3. The PFZ simulation of (a) daily mixed layer depth (MLD), (b) SST, (c) phosphate concentration, and (d) export production (EP), showing the standard model results (September 1994 to December 1995, solid line) and the observed data (1991-1998, ✱).

3.5 Sensitivity studies

The standard simulation suggests that the SAZ, and to an even greater extent the PFZ, experience considerable nutrient resupply in most seasons, particularly in spring. Thus seasonal nutrient depletion significantly under-estimates export production (Table 3.2). In the following sections, we examine the robustness of this result by determining the depletion/export ratio for various formulations of the new production, export production, and vertical mixing. The scaling factor, R, remains unchanged in most of the simulations. The exceptions are in Section 4.2 where R increased by 25% for an indicative Fe test and in Section 4.4 where R increased by 40% for an enhanced wind stress run. For these conditions, the model always reproduced the observed seasonal phosphate depletion.

3.5.1 Remineralization profile

Apart from the exponential equation, another commonly used remineralization profile is the power law function (Martin et al., 1987):

$$P_r(z) = \left(\frac{z}{z_e}\right)^{-0.9} \tag{3.11}$$

With this equation, organic material is remineralized shallower in the water column relative to the exponential formulation. In our model, this created a subsurface maximum in the nutrient fields just below the euphotic zone. With equation 3.11, 13% of the organic matter reaches 1000 m, whereas with our standard run (equation 3.8) the amount is 10%. The sediment trap collections (Trull et al., 2001b), found only 2–3% of the organic matter was exported to 1000 m depth, in comparison to the surface nutrient depletion (Lourey and Trull, 2001).

Hence even more remineralization of organic matter in the upper ocean may be required. However, the sediment traps do not collect 100% of the export production (Yu et al., 2001; Trull et al., 2001b). Thus we explored the sensitivity of the simulated phosphate resupply in the SAZ and the PFZ to the chosen remineralization profile.

We performed four simulations to compare three types of remineralization profiles (power function, exponential, and uniform distribution) and two rates of export at 1000 m (Table 3.3 footnote). The power law function produced a strong subsurface maximum in phosphate concentration between 100 m and 150 m in both the SAZ and the PFZ, while the simulation with the exponential or uniform distributions did not (Figure 3.4 and Figure 3.5).

Annual export production from the euphotic zone was nearly the same for the different simulations, ranging 56.7 – 57.0 mmol P m^{-2} in the SAZ and 74.0 – 74.1 mmol P m^{-2} in the PFZ (Table 3.3). The slight differences in the phosphate export were due to the small differences in the vertical supply of the phosphate to the euphotic zone caused by the change in the vertical gradient of phosphate below the euphotic zone. Table 3.3 presents the phosphate export, depletion and resupply for the main growing season (1st September to 1st March), which is also the nutrient depletion season in the Southern Ocean. The simulations indicated that in both regions, the phosphate depletion was less when more organic material was remineralized shallower in the water column (using equation 3.11) because the phosphate resupply was stronger. However, the subsurface maximum simulated with equation 3.11 was inconsistent with the observations which showed that the nutrients were almost uniform in the remnant winter mixed layer in both the SAZ and the PFZ (Lourey and Trull, 2001). For all the other runs, the ratios of phosphate resupply to export production were very similar, and the range in depletion/export ratio was 69 – 73% for the SAZ and 37 – 44% in the PFZ. Therefore, the choice of remineralization profile did not have a large influence on our estimates of export or resupply.

3.5.2 Seasonal biological factors

Due to the lack of direct observations of phytoplankton in the Southern Ocean, we used the seasonal *Chl a* retrieved from SeaWiFS data to estimate the phosphate concentration in the phytoplankton (Equation 3.3). There is approximately ±20% disagreement between the SeaWiFS retrieved *Chl a* and the *in situ Chl a* in the Australian Sector of the Southern Ocean (Clementson et al., 2001). The two available years of *Chl a* from the SeaWiFS data revealed different seasonal pattern in the SAZ. Regarding the ratio of carbon to *Chl a* (*C/ Chl*), there was limited information in the Southern Ocean. Arrigo et al. (1998) used a value of 75 to estimate the primary production in the Southern Ocean. However, there is some evidence that *C/Chl* should vary seasonally, with relatively higher values in the summer (> 100) in the Southern Ocean (Boyd and Griffiths, pers. comm.). Uncertainties in the *Chl a* field and the *C/Chl* ratio, particularly their seasonality, might affect the model results by changing the seasonality of the export production. As discussed above, iron limitation may also change the seasonality of export production. Thus, we investigated their potential influence on phosphate export and resupply estimates.

Table 3.3. Effect of remineralization profile on phosphate export, depletion and resupply in the euphotic zone from 1st September to 1st March

Phosphate ($mmol/m^2$)	Remineralization profile* Exp1	Exp2	PWL	Linear	Average
			SAZ		
Annual export	56.7	56.8	57.0	56.7	56.8
Seasonal export	38.8	38.7	38.9	38.8	38.8
Seasonal depletion	27.4	26.8	24.9	28.2	26.8
Seasonal resupply_z	11.4	11.9	14.0	10.6	12.0
Seasonal dep./export (%)	71	69	64	73	69
			PFZ		
Annual export	74.1	74.1	74.2	74.0	74.1
Seasonal export	52.6	52.6	52.7	52.6	52.6
Seasonal depletion	21.9	21.0	17.9	23.0	20.9
Seasonal resupply_z	8.4	9.3	12.5	7.4	9.4
Seasonal resupply_y	22.2	22.2	22.2	22.2	22.2
Seasonal dep./export (%)	42	37	34	44	39

* Exp1: $\exp^{-\left(\frac{z-z_e}{400}\right)}$ (10% of the new production reached 1000 m)

Exp2: $\exp^{-\left(\frac{z-z_e}{250}\right)}$ (2.5% of the new production reached 1000 m)

PWL: $\left(\frac{z}{75}\right)^{-0.89}$ (10% of the new production reached 1000 m)

Linear: $1 - \frac{0.9}{925}(z-75)$ (10% of the new production reached 1000 m)

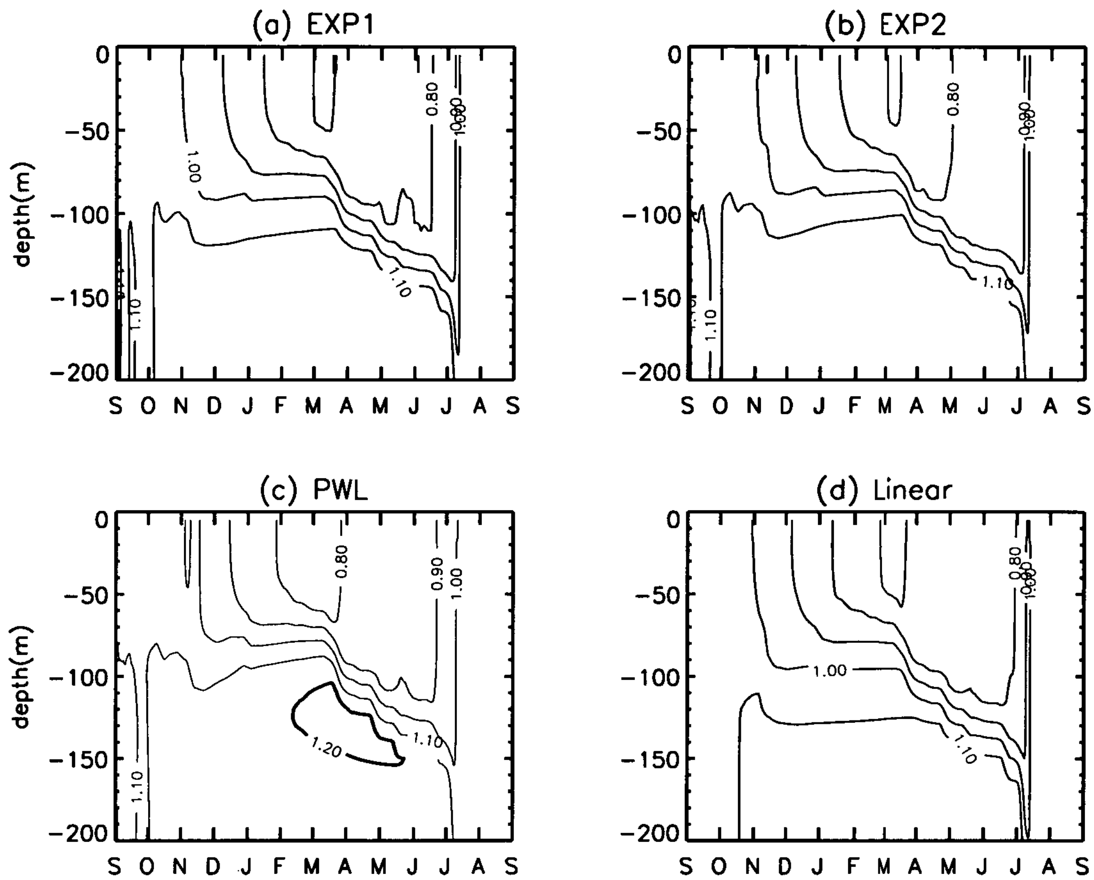

Figure 3.4. The sensitivity of the SAZ simulation to the vertical distribution of remineralization for the daily phosphate concentration for the (a) EXP1, (b) EXP2, (c) PWL, and (d) Linear formulations.

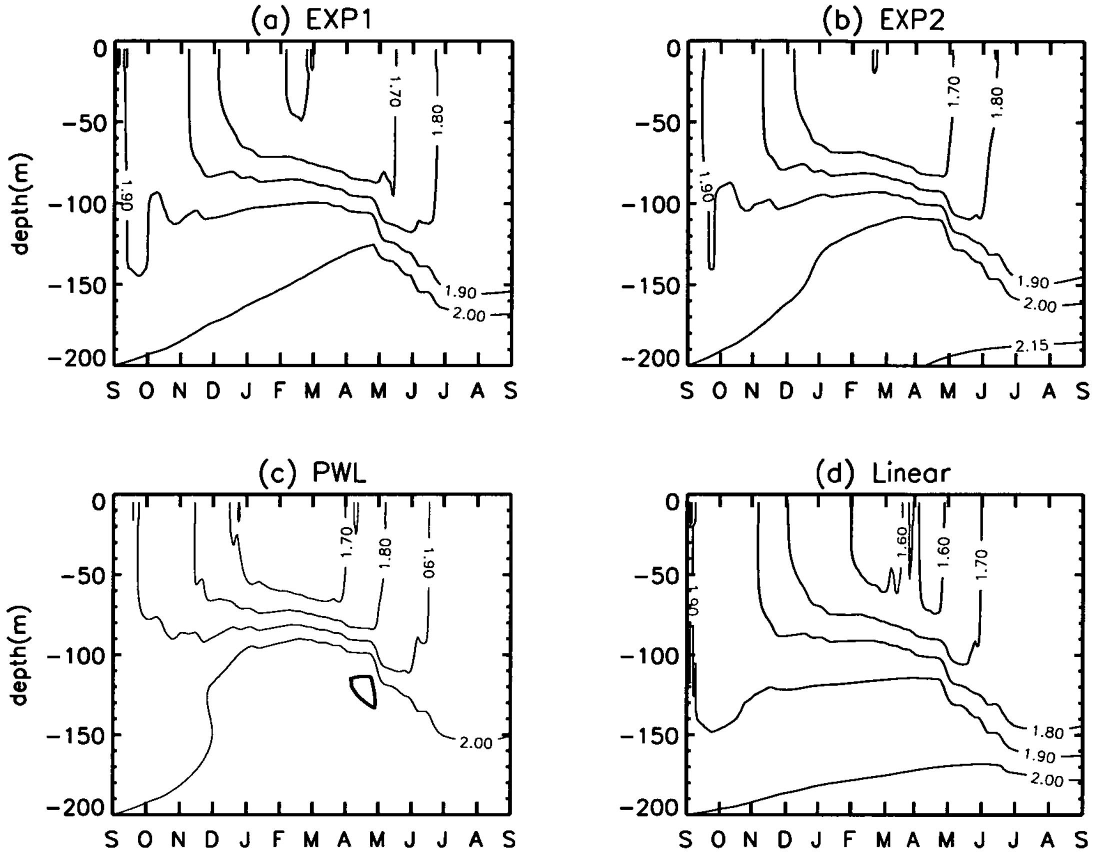

Figure 3.5. The sensitivity of the PFZ simulation to the vertical distribution of remineralization for the daily phosphate concentration for the (a) EXP1, (b) EXP2, (c) PWL, and (d) Linear formulations.

As given in the footnotes of Table 3.4, we compared three seasonal patterns of the *Chl a* concentration and one seasonal *C/Chl* variation (linear change from 100 in December and January to 50 in June and July). For an indicative test of iron limitation (Fe*), we explicitly decrease the term $p/(K+p)$ by 50% for the period of January to June. This approach was based on recent studies which suggest that seasonal iron limitation is likely to reduce the phytoplankton growth rate by ~50% in the summer (Pondaven et al., 2001; Blain et al., 2001), via a variety of cellular mechanisms including changes in light utilization (Geider and LaRoche, 1994).

Figure 3.6 shows the seasonal patterns of the phosphate concentration and export. There were no significant differences in the seasonal phosphate field between the five runs in both regions. But the phosphate declined more rapidly in the Fe* run than the other runs in the spring to early summer. The export production was the highest in the spring season except in the run Chl98 in the SAZ where using the SeaWiFS *Chl a* from 1998/1999 predicted the highest export in the summer season. It is not surprising that the Fe* run produced the highest export production in spring and the lowest in summer. It is interesting to note that the Fe* run created the lowest seasonal depletion/export ratio in both regions. Among the other runs, although there were some differences in the seasonal export production, the seasonal patterns of the *Chl a* and *C/Chl a* did not affect the phosphate export and resupply estimates in the major growing season (Table 3.4). By changing the seasonality of the export production, the season depletion/export ranged from 67% to 78% in the SAZ and from 41% to 46% in the PFZ.

Table 3.4. Phosphate export, depletion and resupply in the euphotic zone in relation to seasonal biological factors from 1st September to 1st March

Phosphate	------ Seasonal biological factors# -------				
($mmol/m^2$)	Chl97	Chl98	Chl0	C/Chl	Fe*
			---------------- SAZ ----------------		
Annual export	57.0	57.1	57.7	54.8	60.9
Seasonal export	39.5	36.8	36.1	40.6	45.4
Seasonal depletion	29.9	28.6	26.4	30.1	30.1
Seasonal resupply_z	9.6	8.2	9.7	10.5	15.3
Seasonal dep./export (%)	76	78	73	74	67
			---------------- PFZ ----------------		
Annual export	74.4	70.5	82.5	74.1	71.5
Seasonal export	56.5	52.0	54.3	56.7	55.0
Seasonal depletion	26.0	22.4	23.9	26.1	22.6
Seasonal resupply_z	8.2	7.3	8.2	8.4	10.2
Seasonal resupply_y	22.2	22.2	22.2	22.2	22.2
Seasonal dep./export (%)	46	43	44	46	41

Chl97: using 8 day average *Chl a* from 1st Sep. 1997 to 1st Sep. 1998 (SeaWiFS).
Chl98: using 8 day average *Chl a* from 1st Sep. 1998 to 1st Sep. 1999 (SeaWiFS).
Chl0: *Chl a* set to 0.27 mg m^{-3} for the SAZ, 0.25 mg m^{-3} for the PFZ.
C/Chl: carbon to *Chl a* ratio varying from 50 (Jun.-Jul.) to 100 (Dec.-Jan.).
Fe*: *Chl a* and C/*Chl a* are the same as the standard run.

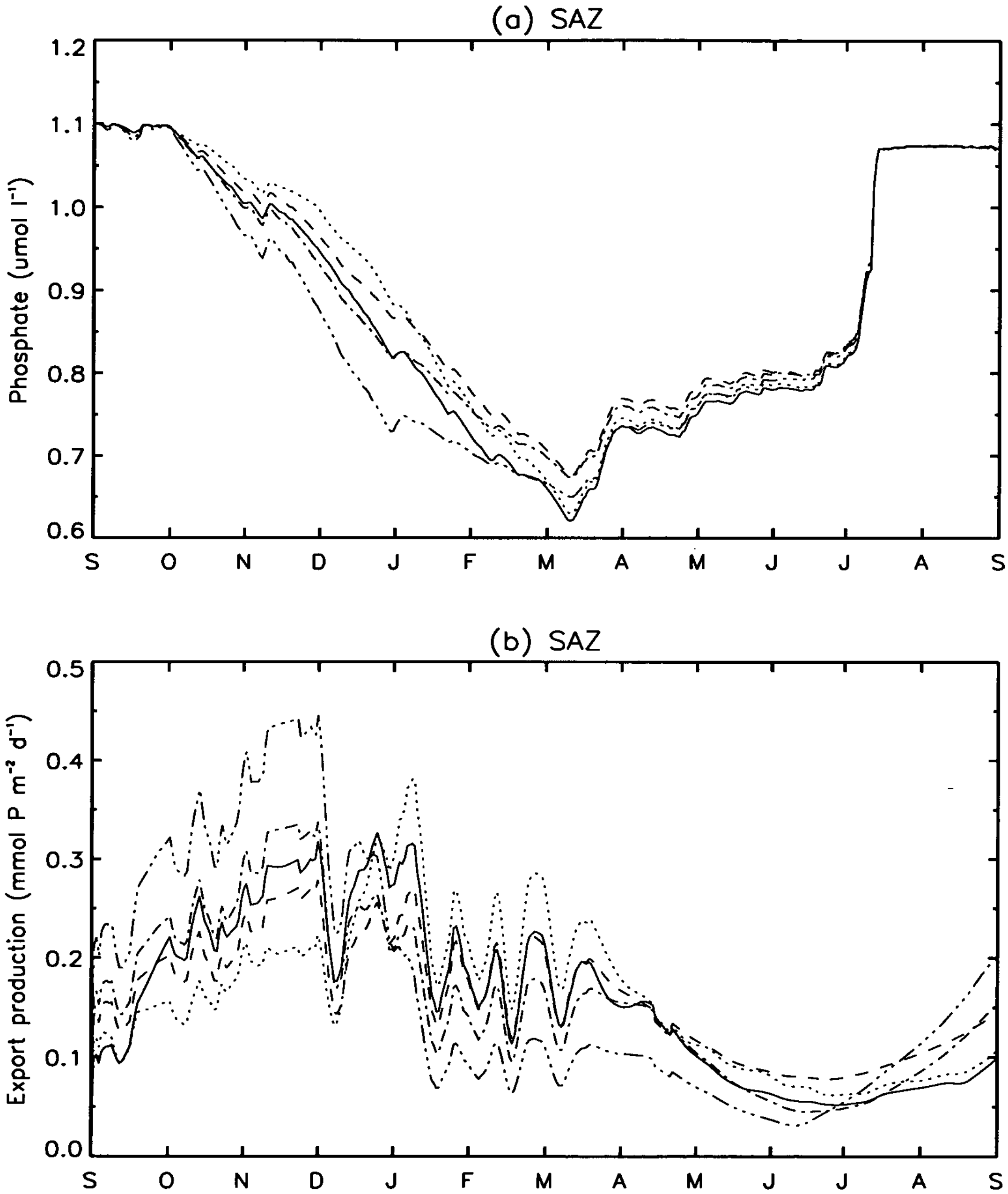

Figure 3.6. The simulated daily phosphate concentration in (a) SAZ and (c) PFZ, and weekly export production in (b) SAZ and (d) PFZ, showing Chl97 (solid line), Chl98 (dotted line), Chl0 (dashed line), C/Chl (dot-dashed line), and Fe* (dot-dot-dot-dashed line).

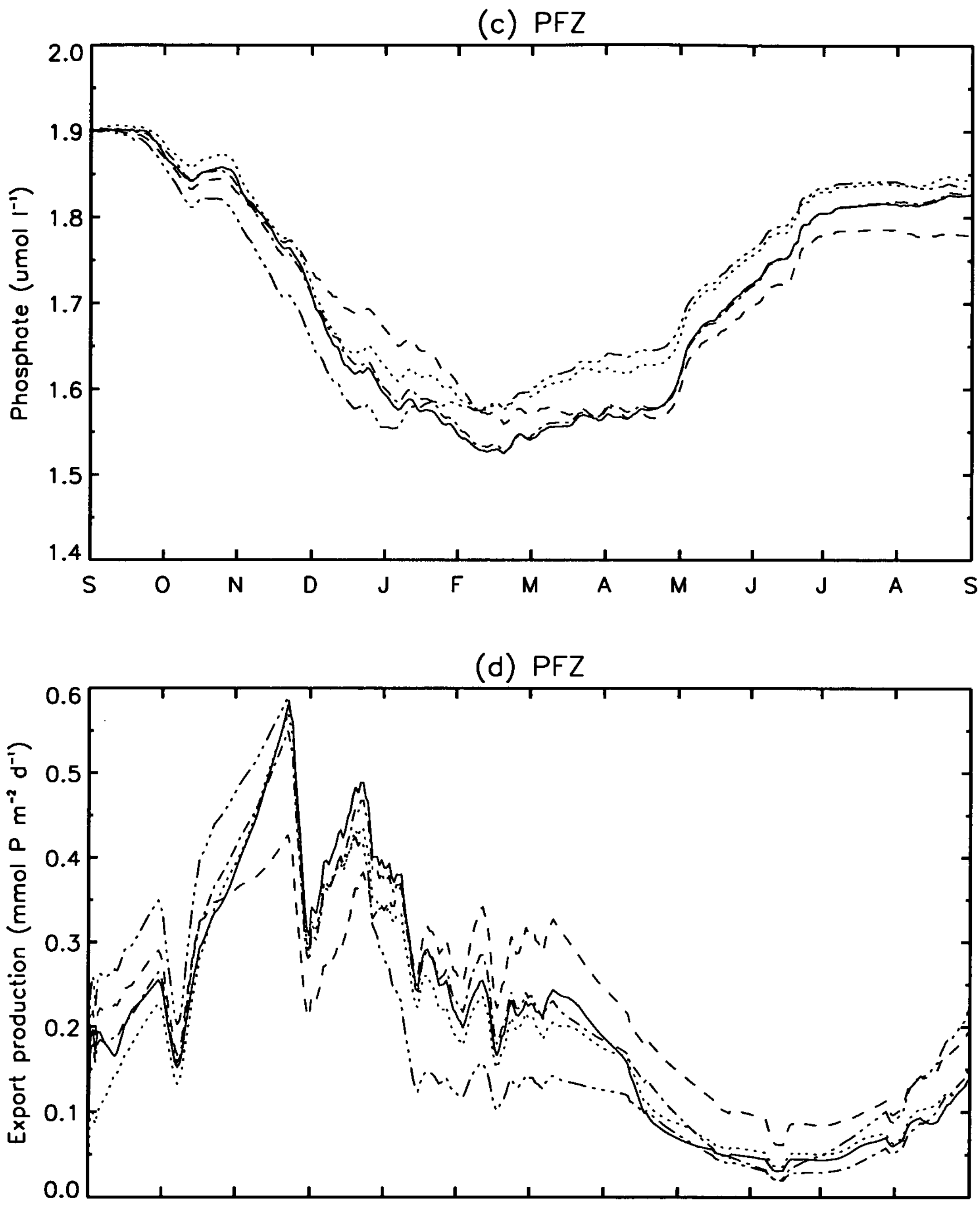

Figure 3.6. (continued)

3.5.3 Interannual variability

In the SAZ and the PFZ, there is considerable interannual variability in both the nutrient concentration and the seasonal nutrient depletion [Lourey and Trull, 2001] as well as the SST and MLD (Trull et al., 2001b; Parslow et al., 2001). In addition, our model simulations (Wang and Matear, 2001) produced large interannual variability in the SST and MLD when forced with data from four different years (1995 – 1998) of forcing fields. Since the SST and the MLD help determine the new production, it is important to investigate their influence on the export and the resupply estimates. We are unable to fully evaluate the interannual variability due to the lack of multi-year observation in both the nutrient and *Chl a* fields. However, we can examine the variations which result from different physical forcing, using four years of forcing (1995 to 1998) as described by Wang and Matear (2001). For lack of data at other times, we used the same observed seasonal phosphate and *Chl a* from the SeaWiFS data to calibrate the model.

Using four different years of forcing, the simulated seasonal SST and the MLD in the SAZ (Figure 3.7) and in the PFZ (Figure 3.8) do vary. In the SAZ, for the period of November – February, the year 1995 had the lowest SST and the deepest MLD and the years 1996 and 1997 had the highest SST and the shallowest MLD. In the SAZ, it appeared that when the MLD was deeper (1995 and 1998), the annual total export, the seasonal export and resupply were higher than in the other years (Table 3.5). In the PFZ, there was no clear trend in the MLD although the SST was generally lower in 1995 and 1998 than in 1996 and 1997. The interannual variation in the export production was small (less than 10%) although there was significant interannual variability in the phosphate in both regions. The depletion/export for the major growing season ranged from 68% to 75% in the SAZ and from 42% to 47% in the PFZ.

Table 3.5. Interannual variability of the phosphate export, depletion and resupply in the euphotic zone from 1st September to 1st March

Phosphate	---------------- Year ----------------				
($mmol/m^2$)	1995	1996	1997	1998	Average
		---------------- SAZ ----------------			
Annual export	56.7	52.6	51.8	55.7	54.2
Seasonal export	39.1	35.7	34.4	38.2	36.9
Seasonal depletion	27.6	26.8	25.7	26.1	26.5
Seasonal resupply_z	11.5	8.9	8.7	12.1	10.3
Seasonal dep./export (%)	71	75	75	68	72
		---------------- PFZ ----------------			
Annual export	74.1	70.2	68.0	71.9	71. 1
Seasonal export	52.6	50.2	47.2	50.3	49.6
Seasonal depletion	22.2	23.7	20.4	21.5	21.9
Seasonal resupply_z	8.2	7.2	9.1	4.6	7.3
Seasonal resupply_y	22.2	19.3	17.7	24.2	20.9
Seasonal dep./export (%)	42	47	43	42	43

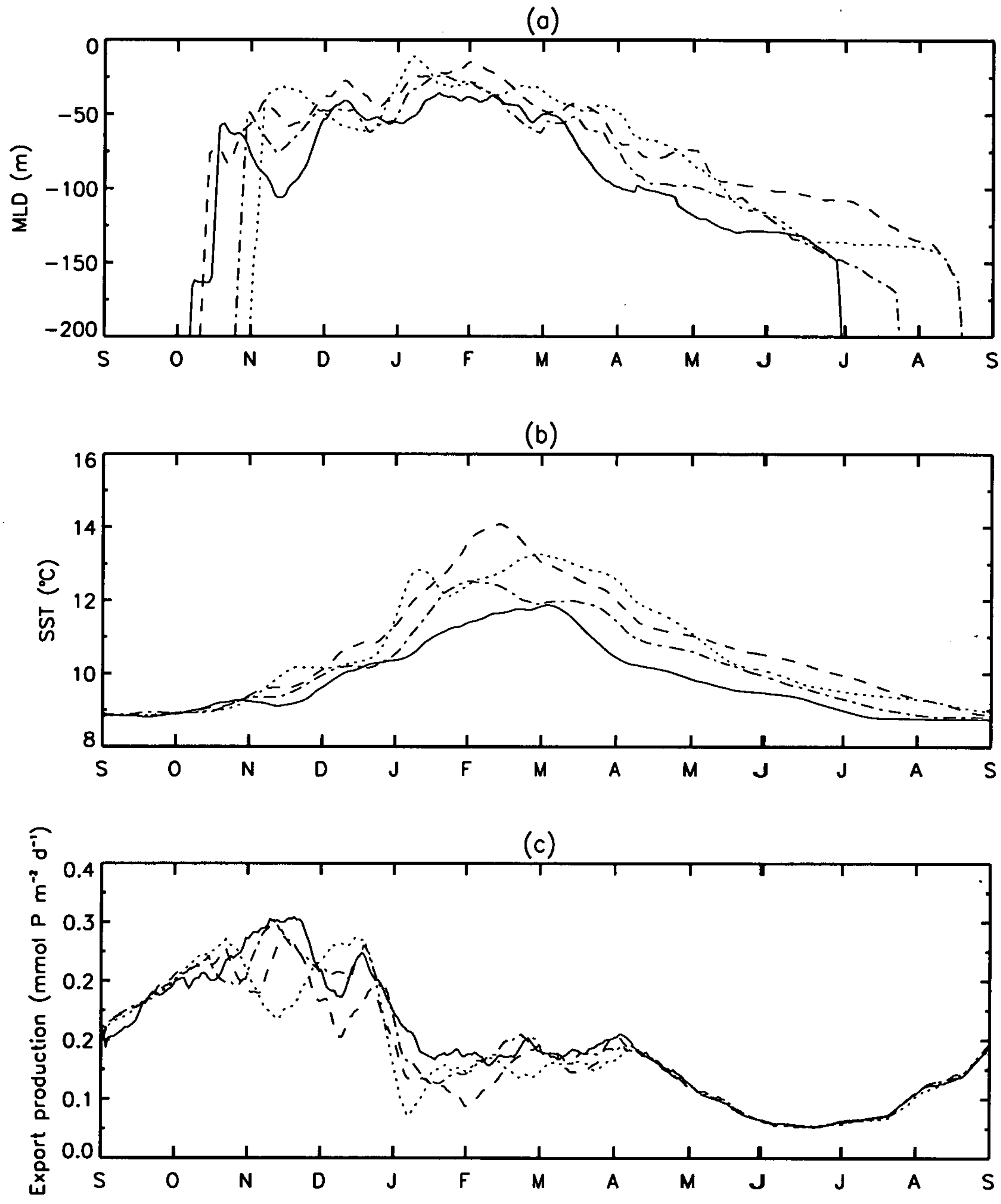

Figure 3.7. The SAZ simulation of (a) weekly mixed layer depth (MLD), (b) SST, and (c) export production, in 1995 (solid line), 1996 (dotted line), 1997 (dashed line) and 1998 (dot-dashed line).

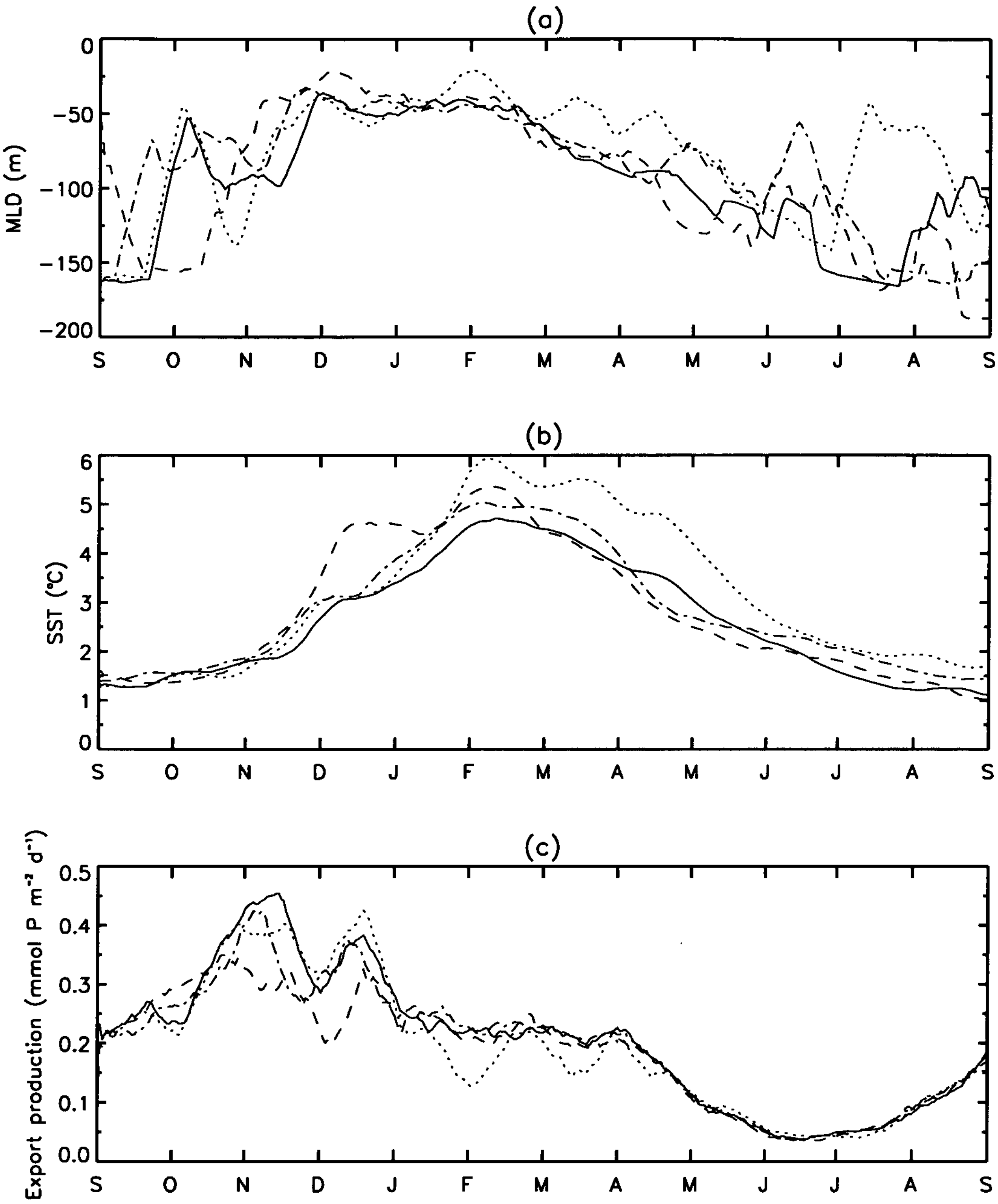

Figure 3.8. The PFZ simulation of (a) weekly mixed layer depth (MLD), (b) SST, and (c) export production (same line patterns as in Figure 3.7).

3.5.4 Influence of enhanced mixing

Using the CTD data, Wang and Matear (2001) showed that the 1-D mixed layer model underestimated the summer MLD by 10 to 20 m in both the SAZ and the PFZ. Similarly, the XBT data showed a deeper mixed layer in the summer of 1998 than simulated (Figures 3.9 and 3.10). One partial explanation is a bias in the NCEP forcing. For example, the wind stress in the NCEP data was only 60% of the wind stresses during March 7 to 12, 1998 in the SAZ (Wang and Matear, 2001). Here we investigate the influence of the potential bias in the NCEP wind field on the model simulation for 1998, by increasing the wind stress by 60% (referred to as WS). For comparison, we also perform the simulation for 1995.

Apart from the potential bias in the NCEP forcing, another possible explanation for the underestimated MLD in the summer is that the model underestimated the vertical mixing in the summer. This hypothesis is also examined by modifying the entrainment formulation used in the physical model (Wang and Matear, 2001: equation 8):

$$W_e\, H_k(b_l - b_2) = 2mu^{*3} + H_k[(1+n)\, B_0 - (1-n)|B_0|]/2 + B_l \qquad (3.12)$$

to (hereafter referred to as Chen2):

$$W_e\, H_k(b_l - b_2) = 2mu^{*3} + H_k n B_0 + B_l \qquad (3.13)$$

where W_e is the entrainment rate (positive), b_l and b_2 are the buoyancies of water in the Kraus depth and just below it, m and n are constants (m=0.4, n=0.18), u* is the surface friction velocity, B_0 is the total surface buoyancy flux, and B_l is the rate of potential energy generation due to penetration of solar radiation.

Using the new formulation (equation 3.13), the entrainment is only increased in the summer when B_0 is negative. By increasing the entrainment rate one increases vertical mixing in the summer between the MLD and the underlying water. Our Chen2 formulation is similar to that of Markus (1999) except that he set $n = 0.8$ for $B_0 > 0$ and $n = 1$ for $B_0 \leq 0$. Our choice produces more realistic seasonal SST and MLD than does the Markus formulation (Wang and Matear, 2001).

3.5.4.1 The SAZ region

Using the standard Chen scheme (hereafter referred to as Chen) (Chen et al., 1994), the model produced realistic MLDs in 1995, but too shallow MLD in January 1998 (Figure 3.9). The Chen2 and WS runs did not change the MLD in the winter, but significantly deepened the summer MLD. On average, the summer MLD was 10 m deeper in the Chen2 than in the Chen. The MLD was similar in the WS to the Chen2 except that the WS produced deeper MLD than the Chen2 during deepening events in the spring and late summer. In both 1995 and 1998, the Chen more faithfully reproduced the observed seasonal SST than either the Chen2 or the WS. The summer SST was generally lower in the Chen2 and the WS than both the Chen and the observations.

With the similar seasonal phosphate depletion from winter to summer, the WS simulation, with deeper summer MLD, had greater export production than the Chen and the Chen2. The phosphate export was very similar between the Chen and the Chen2 in the spring. However, in the summer the export was much greater in the Chen2 than the Chen. Compared with the Chen, the Chen2 increased the annual export production by ~5% while the WS increased by 20% (Table 3.6). The seasonal depletion/export ratio was lowest in the WS (52 – 53%) but highest in the Chen (68 – 71%).

3.5.4.2 The PFZ region

Figure 3.10 shows that the Chen produced reasonable SST and MLD against the observations in 1995 whereas the Chen2 and the WS predicted slightly deeper MLD and lower SST in the summer. In 1998, the Chen simulated shallower MLD and higher SST in the summer, compared with the observations. The Chen2 and the WS made little differences in the MLD and the SST in the spring but produced deeper MLD (5 – 10 m) and lower SST than the Chen in the summer. The SST simulated in the Chen best represented to the observations.

Compared with the Chen, the annual export of phosphate in the Chen2 increased by 5% and in the WS increased 40% (Table 3.6) because of the strong sensitivity of export production to the summer MLD. Both the Chen2 and the WS simulations increased phosphate resupply. The depletion/export was similar in the major growing season between the Chen2 (36%) and the WS (35 - 38%), which was lower than in the Chen (42%).

Table 3.6. Effect of enhanced mixing on the seasonal phosphate export, depletion and resupply in the euphotic zone from 1st September to 1st March

Phosphate	------ 1995 -------			------ 1998 ------		
($mmol/m^2$)	Chen*	Chen2	WS	Chen	Chen2	WS
			---------------- SAZ ----------------			
Annual export	56.7	57.8	79.4	55.7	58.9	77.9
Seasonal export	39.1	43.8	55.6	38.2	41.1	54.5
Seasonal depletion	27.6	30.6	29.7	26.1	26.2	28.5
Seasonal resupply_z	11.5	13.2	25.9	12.1	14.9	26.0
Seasonal dep./export (%)	71	70	53	68	64	52
			---------------- PFZ ----------------			
Annual export	74.1	77.9	103.9	71.9	75.2	100.7
Seasonal export	52.6	56.7	75.2	50.3	53.7	71.8
Seasonal depletion	22.2	20.2	26.2	21.5	19.5	27.1
Seasonal resupply_z	8.2	14.3	26.8	4.6	10.0	20.5
Seasonal resupply_y	22.2	22.2	22.2	24.2	24.2	24.2
Seasonal dep./export (%)	42	36	35	42	36	38

* Chen: the original scheme.

Chen2: modified to increase vertical mixing in the summer.

WS: forced with 60 % higher wind stress.

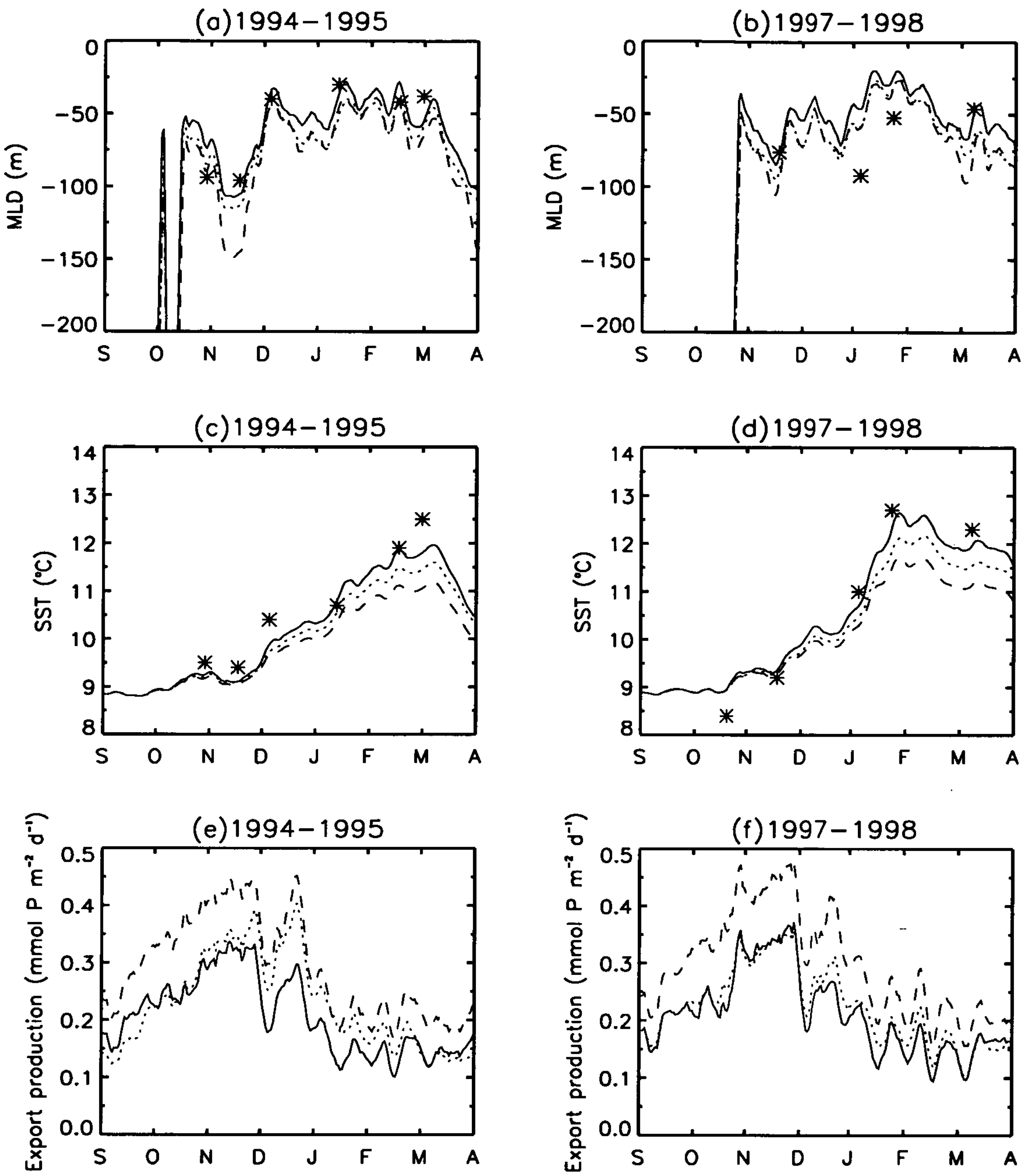

Figure 3.9. The SAZ observation (✳) and simulations with the Chen (solid line), Chen2 (dotted line) and WS (dashed line) formulations for the (a) weekly mean mixed layer depth (MLD) in 1995, (b) MLD in 1998, (c) SST in 1995, (d) SST in 1998, (e) export production in 1995, and (f) export production in 1998.

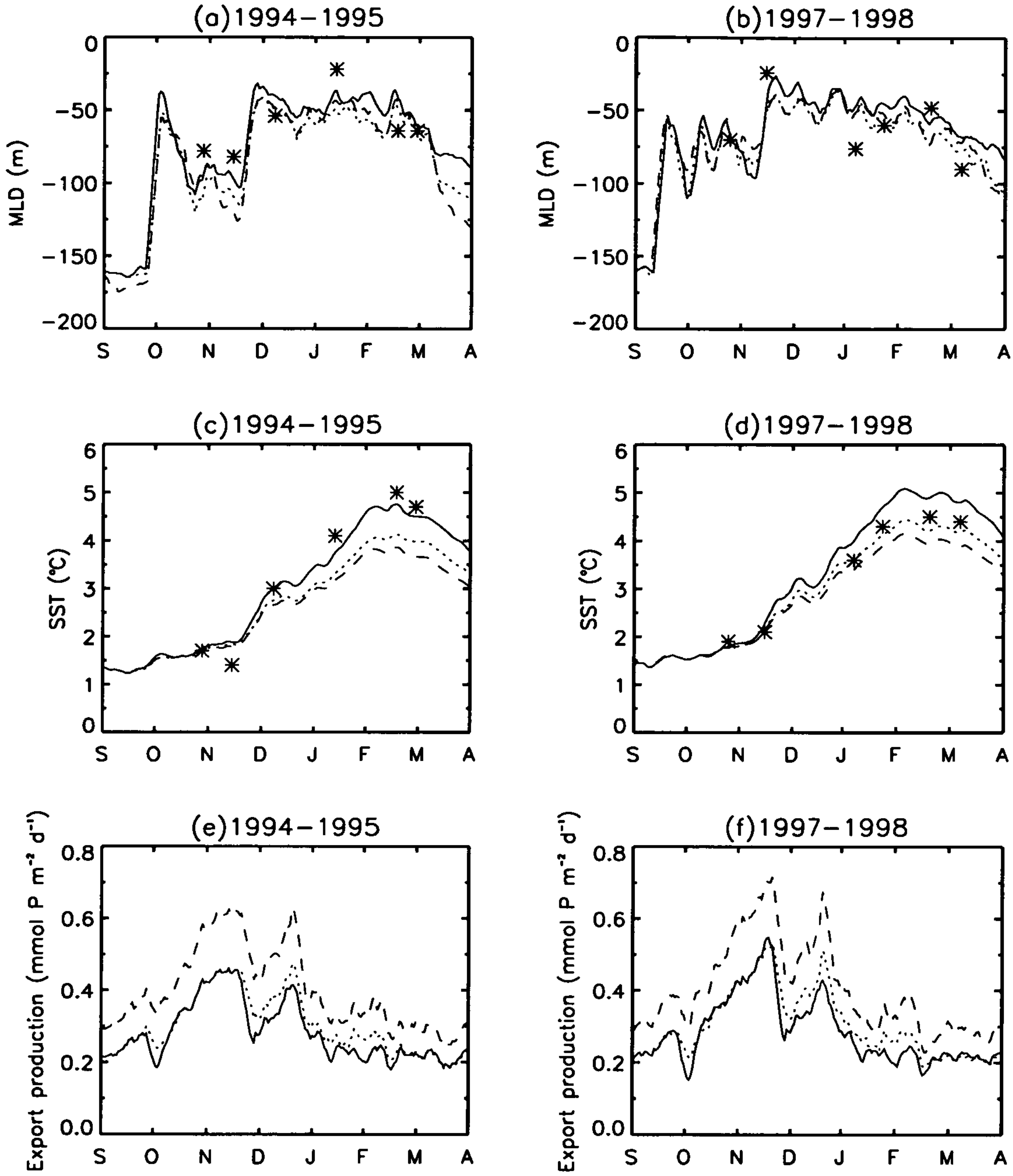

Figure 3.10. The PFZ observation (✳) and simulations with the Chen (solid line), Chen2 (dotted line) and WS (dashed line) formulations for the (a) weekly mean mixed layer depth (MLD) in 1995, (b) MLD in 1998, (c) SST in 1995, (d) SST in 1998, (e) export production in 1995, and (f) export production in 1998.

3.6 Discussion

At our two sites we simulated the seasonal cycle of SST, MLD and phosphate concentrations. The seasonal SST and MLD were consistent with observations. The simulated export production was determined by reproducing the seasonal depletion of observed surface phosphate concentrations. The seasonal pattern of the modeled export production was similar to the seasonal primary production found by Parslow et al. (2001) and Griffiths (unpublished data, 2000). That is the minimum daily winter production was 20% of the maximum daily summer value in the SAZ and 10% of that in the PFZ.

To evaluate uncertainties in the biological field, we undertook a series of sensitivity studies including varying the remineralization profile, the seasonal *Chl a* concentration and the C/*Chl a* ratio and the possibility of iron limitation. We also examined the potential influence due to the uncertainties in physical fields by using different years of NCEP forcing, increasing the wind stress and enhancing summer vertical mixing. In general, the simulated seasonal export production was insensitive to the remineralization profile, the seasonal C/*Chl a* ratio and different year forcing, but more sensitive to the seasonal pattern of *Chl a* and possible iron limitation. Excluding the increased wind stress (WS) simulation (which underestimated the seasonal SST amplitude), our simulations showed three robust features: (1) the major growing season contributed 66 – 76% of the annual export production in both regions, (2) the annual export production ranged 6.3 – 7.2 mol C m^{-2} yr^{-1} in the SAZ and 8.6 – 10.1 mol C m^{-2} yr^{-1} in the PFZ, and (3) the seasonal phosphate depletion/export production ratio was 67 – 78% in the SAZ and 37 – 47% in the PFZ.

Our estimated export production in the SAZ is close to the lower bound estimate (6.66 mol C m^{-2} yr^{-1}) determined by Metzl et al. (1999), but significantly higher than what Lourey and Trull (2001) calculated using the nutrient depletion method (3.4 and 1.4 mol C m^{-2} yr^{-1} in the SAZ and PFZ, respectively). Our model simulation indicated that the seasonal depletion only explains 45 – 55% of the annual export production in the SAZ and 26 – 35% in the PFZ. The significant underestimate of export production occurs for two reasons: (1) export production is not negligible in the minor growing season, which contributes 24–34% of the annual export production in both the SAZ and the PFZ; (2) nutrient resupply is important in the major growing season, with averaged resupply/export of 27% in the SAZ and 58% in the PFZ.

Based on the studies by Parslow et al. (2001) and Griffiths (unpublished data, 2000), the primary production is approximately 12 mol C m^{-2} yr^{-1} in the SAZ and 9 – 11 mmol C m^{-2} yr^{-1} in the PFZ. Using their primary production values and our estimate of export production, we obtain a *f-ratio* (ratio of new production to primary production) of 0.52 – 0.57 in the SAZ and 0.78 – 1 in the PFZ. Our *f-ratios* are higher than what Elskens et al. (2001) estimated based on ^{15}N uptake experiments in late summer (0.3 – 0.5 in the SAZ and 0.56 in the PFZ). In addition to possible seasonal variation, the difference could be partly explained by the uncertainty in the carbon to phosphate (C:P) ratio. We used a ratio of 122 for C:P to convert phosphate export to carbon export. Although the exact values of the calculated *f-ratio* are open to debate, our higher *f-ratio* in the PFZ relative to that in the SAZ indicates that the SAZ is a region of stronger recycling of carbon and nutrients, whereas the PFZ is a region with higher export production. This conclusion is supported by the observations that mesopelagic Ba contents are higher in the PFZ than in the SAZ (Cardinal et al., 2001), which also suggests higher export in the PFZ than in the SAZ.

Despite the similarity in the seasonality of the export production and the phosphate depletion in both the SAZ and the PFZ, the phosphate resupply differed considerably. This is the result of different upper ocean dynamics, in particular the larger role of horizontal resupply of nutrients in the PFZ. In the SAZ, a deep winter MLD (600 m) permits effective vertical supply of phosphate to the upper ocean during the winter, while summer stratification limits resupply during the major growing season to ~20 % of the annual total. In the PFZ, the relatively strong stratification in the water below the mixed layer throughout the year produced much shallower winter MLD (160 m), so that most of the exported phosphate is remineralized below the winter MLD and cannot be effectively resupplied to the upper ocean during the winter. The loss of phosphate from the upper ocean from the sinking of organic matter below the winter MLD must be balanced by horizontal resupply. Given the assumption that this is achieved by Ekman transport in response to the high eastward wind stress, nutrient resupply occurs throughout the year, so that seasonal nutrient depletion provides a large underestimate of export over the major growing season in the PFZ.

The assumption of horizontal resupply via Ekman transport is clearly a simplification, but it appears to be reasonable. A horizontal supply is also need to maintain the observed constant salinity in the upper ocean under the conditions of a large fresh water (88 cm yr^{-1}) influx to the ocean from the atmosphere (Wang and Matear, 2001). Using the averaged eastward wind stress (0.2 N m^{-2}) and the phosphate concentration gradient in a 10° latitude band centered in the PFZ (0.4 mmol m^{-3}) (Rintoul and Bullister, 1999), we estimated that the Ekman transport was ~0.8 x 10^{-6} mmol P m^{-2} s^{-1}. The simple calculation accounts for 50% of the required horizontal supply of phosphate needed to close the annual phosphate budget. Eddy transport would supply additional nutrients and cold salty water to the region, but we do not have sufficient data to quantify this. On an annual basis, we estimate that the horizontal transport provided 63% of the phosphate to the euphotic zone of the PFZ. The phosphate resupply in the major growing season was nearly equal to that in the minor growing season. It is this horizontal resupply, that is required to balance the 1-D model of the seasonal cycle of nutrient concentrations, which produces the low depletion/export ratio in the PFZ during the major growing season. This reconciles the previous apparent contradiction of low seasonal nutrient depletion in the PFZ (Lourey and Trull, 2001) in the presence of high export production (Cardinal et al, 2001).

In summary, the PFZ is a region of greater export production than the SAZ, despite lower primary production and lower seasonal nutrient depletion. Lower nutrient depletion in the PFZ reflects greater horizontal transport, whereas the high export production may reflect a greater proportion of large phytoplankton that has a fast sinking rate. A well-validated 3-D modelling approach would eventually offer a better understanding of horizontal nutrient supply. Better constrains on export production should come from combining such a 3-D model with a more sophisticated ecosystem model that includes iron limitation and phytoplankton dynamics.

Chapter 4. Simulation of the upper ocean dynamics: III. The seasonal nutrient utilization ratios

A paper will be submitted to Global Biogeochemical Cycles:

Nutrient utilization ratios in the Polar Frontal Zone in the Australian sector of the Southern Ocean: a model approach

Xiujun Wang[1,2], Richard J. Matear[1,3], and Thomas W. Trull[1]

1. Antarctic CRC, University of Tasmania, GPO Box 252-80, Hobart, 7001, Tasmania, Australia.
2. Institute of Antarctic and Southern Ocean Studies, University of Tasmania, GPO Box 252-77, Hobart, 7001, Tasmania, Australia.
3. CSIRO Division of Marine Research, GPO Box 1538, Hobart, 7001, Tasmania, Australia.

4.1 Abstract

We developed a one-dimensional biophysical model to simulate seasonal phosphate, nitrate and silicate export production in the Polar Frontal Zone (PFZ) of the Southern Ocean. There were two groups of phytoplankton: diatoms and non-diatoms in the model. We assumed that nutrient utilization ratio followed the Redfield ratio in the non-diatoms and determined the N/P/Si utilization ratios in the diatoms in a steady state ocean. We used estimates of phytoplankton biomass from the Sea-viewing Wide Field-of-view Sensor to determine production, and tuned the model to reproduce the observed seasonal cycles of phosphate and silicate. For nitrate, we carried out a series of sensitivity studies to identify the possible mechanism required to reproduce the observed seasonal cycle. The estimated annual export production is ~65 mmol P m^{-2}, ~820 mmol N m^{-2} and 1826 mmol Si m^{-2} in the euphotic zone for phosphate, nitrate and silicate respectively. The diatoms contribute 85% and 80% of the annual phosphate and nitrate export production. In the euphotic zone, the annual N/P utilization ratio is 11.5 – 12.9 in the diatoms and 12.1 – 13.6 in the community. The seasonal Si/N utilization ratio is 3 – 6 in the diatoms and 1 – 4 in the community, with the lowest found in the late summer. The annual Si/N utilization ratio is 2.5 – 3 in the diatoms and 2 – 2.5 in the community. The low N/P depletion ratio is associated with the preferential recycling of phosphate below the euphotic zone, the low ΔDON/ΔDOP ratio in the euphotic zone and the low N/P utilization ratio in the diatoms. The low N/P and high Si/N utilization ratio may reflect the low iron availability in the PFZ waters.

4.2. Introduction

Estimates of carbon utilization and export have often been obtained from extrapolation of N or P utilization using assumed C/N or C/P ratio (Jennings et al., 1984; Sarmiento and Le Quere, 1996; Matear and hirst, 1999). This approach is useful as an average for diverse phytoplankton assemblages, and to allow large-scale comparisons. However it may introduce considerable bias in regional ocean studies, in particular in an area such as the Southern Ocean where the classical Redfield ratios do not hold (Jennings et al., 1984; Karl et al., 1991; DeBaar et al., 1997; Rubin et al., 1998; Arrigo et al., 2000; Sweeney et al., 2000; Lourey and Trull, 2001). Although the non-Redfield ratio has been widely observed, there is a study showing that the carbon, nitrate and phosphate depletion ratios are consistent with the Redfield ratio in the Southern Ocean (Hoppema and Goeyens, 1999). They have suggested that the Redfield ratios may only apply to the seasonal to annual cycle whereas the non-Redfield ratios are short-period events. Hence this issue needs to be addressed because most of model simulations of ocean carbon export is sensitive to changes of the Redfield ratios, and our understanding of how the ocean carbon and nutrient cycles are coupled needs to be revised (Denman et al., 1996). In particular we need better understanding the biological pump in the Southern Ocean because the export production is most likely to respond strongly to climate change (Sarmiento and Le Quere, 1996; Matear and Hirst, 1999; Bopp et al., 2001).

The inconsistency in the nutrient utilization ratios in the Southern Ocean may reflect phytoplankton community structure because researches have shown that the low N/P depletion ratios have been related to the diatoms in the Southern Ocean (DeBaar et al., 1997; Arrigo et al., 2000; Sweeney et al., 2000). For example, Arrigo et al. (2000) reported that the N/P depletion ratio (9.5) for waters dominated by diatoms was significantly lower than the Redfield ratio, and DeBaar et al. (1997) reported even lower N/P depletion ratio (4.4–6.1) during a spring diatom bloom in the PFZ. They suggested that the low N/P depletion ratio might result from preferential regeneration of organic N into nitrate relative to organic P into phosphate. However, a few studies show that organic P is preferentially remineralized over organic N (Clark et al., 1998; Benitez-Nelson and Buesseler, 1999; Loh and Bauer, 2000). Another hypothesis is that the dissolved organic pool (DOM) accumulates DON and DOP in anomalous proportions (DeBaar et al., 1997). It is important to note that while the seasonal accumulation of ammonium and its use by phytoplankton during regenerated production can produce seasonal variations in the N/P depletion ratio, ammonium use cannot be the origin of the low N/P depletion ratio over the seasonal cycle, because all ammonium derives initially from nitrate via new production and subsequent grazing, i.e there is no significant pool of ammonium in winter.

While there is limited information about the nutrient regeneration and DON/DOP ratio in the PFZ, there is evidence that the diatoms have a lower N/P uptake requirement than non-diatoms, and that the N/P uptake ratio decreases under Fe limited condition (Takeda, 1998; Boyd et al., 1999). Research has also shown that in nutrient-limited (macronutrient or micronutrient) waters, the nitrate uptake is often decoupled from carbon consumption and silicate uptake (Richardson and Cullen,, 1995; Moore and Villareal, 1996; Parslow et al., 2001). For example, more nitrate uptake occurred associated with high Fe availability (Franck et al., 2000). Limited research has shown that more nitrate uptake occurred in the subsurface, in comparison to that in the mixed layer (F. Dehairs, personal communication 2001). This is probably partially due to the increase of iron availability in the subsurface and partially due to uptake of nitrate at night (Parslow et al., 2001).

In this study we use a model to investigate the factors that may contribute to low N/P depletion ratio observed in the PFZ. To do this, we develop a simple one-dimensional (1-D) biophysical model by including two groups of phytoplankton: diatoms and non-diatoms. We assume that nutrient utilization ratio follows the Redfield ratio in the non-diatoms, but determine the seasonal N/P/Si utilization ratios of diatoms in a steady state ocean. We take into account the potential influence of iron availability and the decoupled nitrate uptake from other nutrient uptake. In addition to the N and P cycles, we also study the Si cycle because silicate can be a limiting nutrient for diatoms in this region (Franck et al., 2000). An important feature in this region is a diatom dominated subsurface chlorophyll maximum (SCM), which is intense and productive in spring (~35% of the total production) and early summer (~50% of the total production) but less intense and unproductive in later summer (5-20%) (Parslow et al., 2001). The objectives of this study are (1) to identify the potential mechanisms capable reproducing the observed nutrient fields, (2) to determine the nutrient utilization ratios at the seasonal to annual time-scale in the euphotic zone, (3) to investigate the relationship between the low N/P depletion ratio and the recycling of nitrate and phosphate, and (4) to study the potential role of DON/DOP ratio on the N/P depletion ratio.

4.3. Hydrographic setting and distribution of nutrients

The Southern Ocean refers to the large area between the Antarctic continent and the Subtropical Front (STF, Figure 4.1). The ocean circulation in this area is dominated by the continuous eastward-flowing Antarctic Circumpolar Current (ACC) which causes the horizontal distribution of water properties in the Southern Ocean to be relatively uniform in the zonal direction (Pickard and Emery, 1990).

There have been several cruises undertaking both hydrographic and biogeochemical measurements along ~140°E of the Southern Ocean during 1991–1998 (see references in Griffiths et al., 1999; Lourey and Trull, 2001) (Figure 4.2).

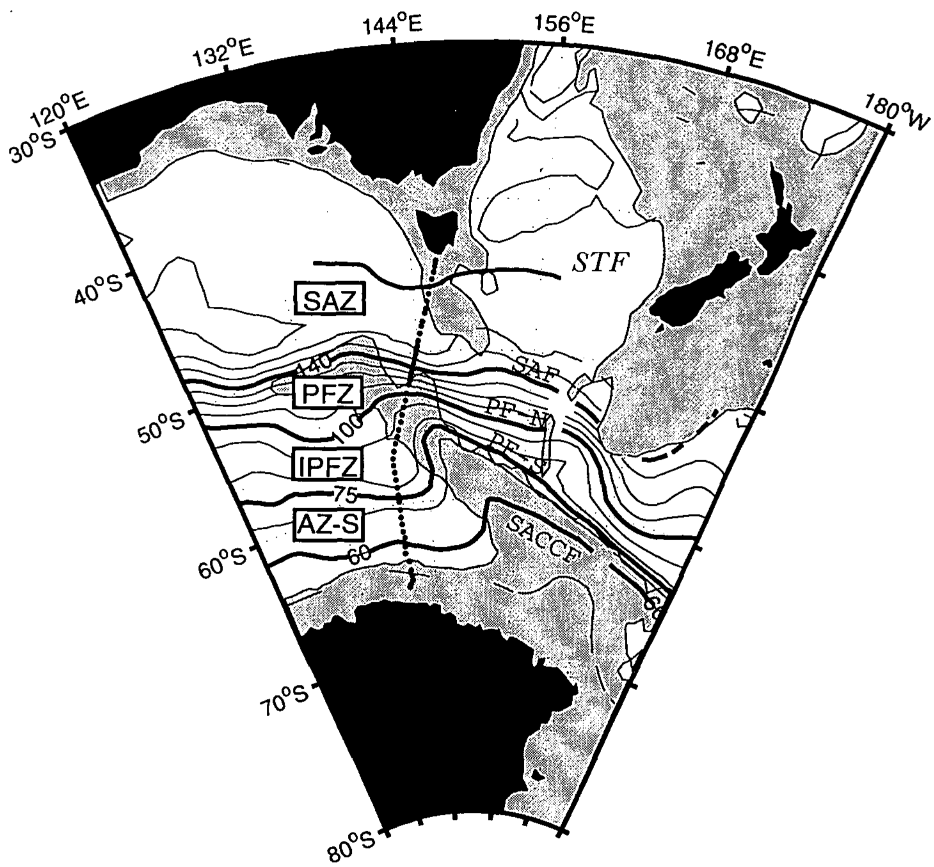

Figure 4.1. The Australian sector of the Southern Ocean with dynamic height (dyn cm, solid lines), approximate positions of the major fronts and zones, and the nutrient sample sites.

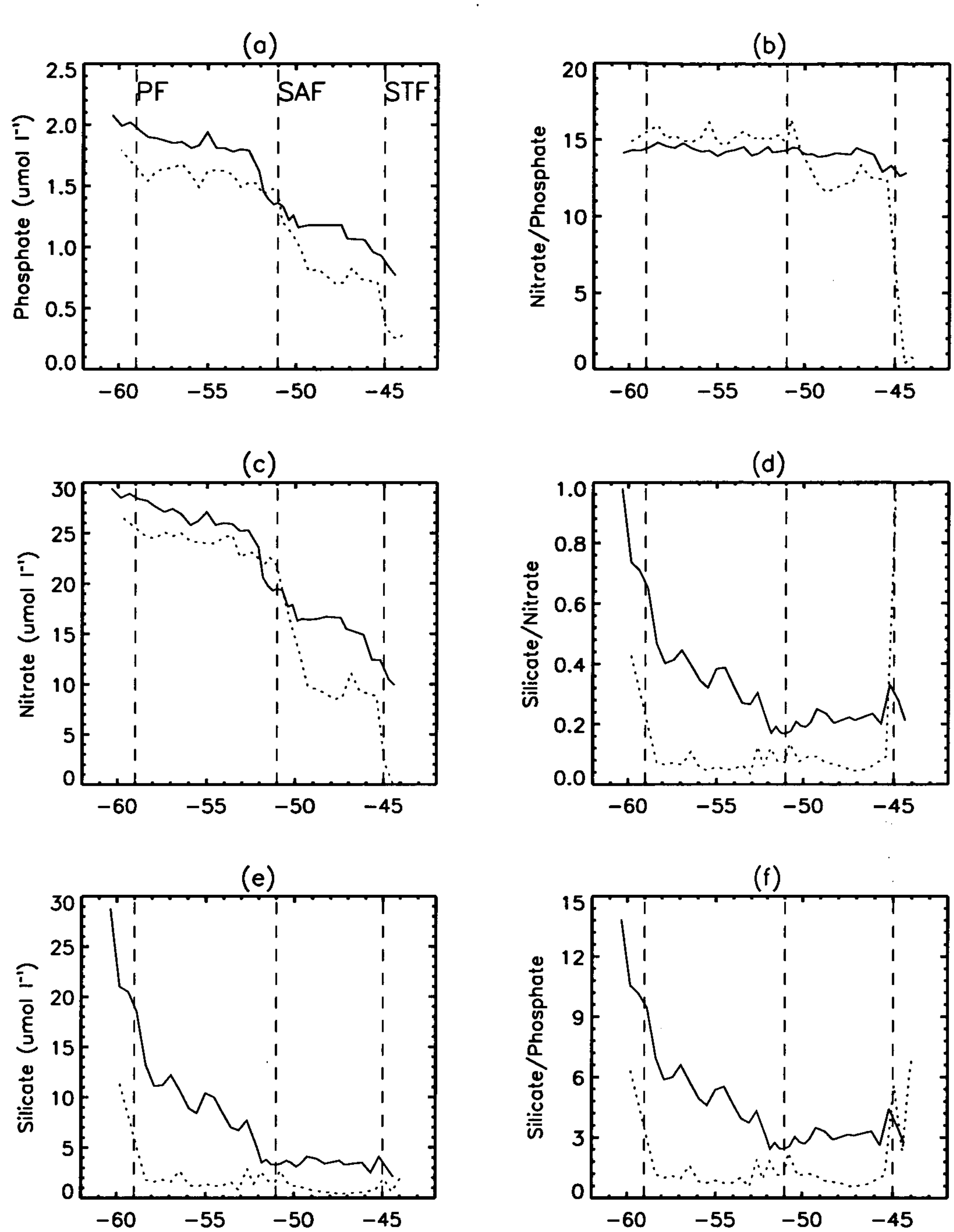

Figure 4.2. Meridional concentration change for (a) phosphate, (c) nitrate, and (e) silicate, and ratio change for (b) nitrate/phosphate, (d) silicate/nitrate, and (f) silicate/phosphate in the surface waters in AU9501 (solid lines) and AU9309 (dotted lines).

In general, the concentrations of nitrate, phosphate and silicate in the mixed layer increased from north to south in both the winter and the summer waters. However, there are some discrepancies in the meridional patterns of the nutrients. The concentrations of nitrate and phosphate display very similar meridional patterns with the greatest meridional gradient found in the Subantarctic Front (SAF) while the concentration of silicate showed the greatest zonal gradient at the Polar Front (PF). The silicate nearly completely depleted in the summer across the whole region.

In the winter, nitrate/phosphate ratio was almost uniform in the region, ranging from 14 to 15 (Figure 4.2b), which was slightly lower than the classic Redfield ratio of 16. However, the summer waters showed higher nitrate/phosphate ratio south (~16) of the Subantarctic Front than north of the Front (<13), reflecting lower nitrate/phosphate depletion ratio in the south than the north. The nitrate/silicate and silicate/phosphate ratios are also different between the winter waters and the summer waters. The meridional and seasonal differences in the nitrate/phosphate, nitrate/silicate and silicate/phosphate ratios suggest that biogeochemical processes may be significantly different between the south and the north of the Subantarctic Front. In the following sections, we will use some of the observed features in the nutrient field to constrain the biophysical model and to address some of the gaps in our knowledge.

4.4. Model description

In the euphotic zone the nutrient cycle is affected by physical (resupply by entrainment and horizontal transfer) and biological (phytoplankton consumption and export) processes and in our model we express it as:

$$\frac{dX}{dt}=\frac{d}{dz}\left(Kz\frac{dX}{dz}\right)+F^{X}-EP^{X} \tag{4.1}$$

where X represents the simulated nutrient (e.g. nitrate, phosphate or silicate), K_z is vertical mixing coefficient calculated by our mixed layer model (Wang and Matear 2001), F^X is the horizontal supply of the nutrient, and EP^X is the export production for nutrient X.

4.4.1 Horizontal supply

Ekman transport plays a major role in supplying nutrients and cold salty water to the upper ocean in the PFZ (Wang and Matear, 2001; Wang et al., 2001). Following Wang and Matear (2001) parameterization of horizontal supply of the cold and salty water in this region, we specify the horizontal supply of F^X as follows:

$$F^{X}(t)=\overline{F}^{X}\frac{\tau x(t)\,Xy(t)}{\overline{\tau x}\;\;\overline{Xy}} \tag{4.2}$$

where $\tau x(t)$ is the eastward wind stress at time t, $\overline{\tau x}$ the 4 year (1995-1998) averaged eastward wind stress, $X_y(t)$ the zonal gradient of the nutrient at time t, and $\overline{X}_y$ the annual mean of the zonal nutrient gradient. The term $\overline{F}^{X}$ is the annual mean horizontal transport for nutrient X (see Section 4.4.3).

For nitrate and phosphate, the meridional gradient display no seasonalitysouth of the SAF (Figure 4.2), thus we set $X_y(t) = \overline{X}_y$. The nitrate/phosphate ratio is almost uniform in the PFZ (~14.5 in the winter and ~16 in the summer, Figure 4.2), hence we set $\overline{F}^N = 14.5\overline{F}^P$. For silicate, the meridional gradient is largest in the winter and smallest in the summer (Figure 4.2). Based on the observations, $Si_y(t)$ is calculated from silicate concentration (Si), $Si_y(t) = \lambda(Si(t) - 0.5)$, where λ is a constant (1 m^{-1}). Hence the $Si_y(t)/\overline{Si}_y$ ratio can be scaled from the seasonal change of silicate concentration at the PFZ site so that the meridional gradient is 6 times higher in winter than in summer.

4.4.2. Formulation of the biological model

The biological model parameterizes the biological export of phosphate, nitrate and silicate from the euphotic zone (EP^X term in equation 4.1). There are two groups of phytoplankton, diatoms (Phy_1 in unit of phosphate) and non-diatoms (Phy_2 in unit of phosphate). It is assumed that silicate and phosphate limit the growth of diatoms and non-diatoms, respectively. For phosphate (P), nitrate (N) and silicate (Si) export production is

$$EP^P = \sigma(t,z)\left(\frac{Si}{K\mu + Si} Phy_1 r_1^P + \frac{P}{Kp + P} Phy_2\ r_2^P\right) \tag{4.3}$$

$$EP^N = \sigma(t,z)\left(\frac{Si}{K\mu + Si}\frac{Fe}{Kf + Fe} Phy_1\ r_1^N + \frac{P}{Kp + P} Phy_2\ r_2^N\right) \tag{4.4}$$

$$EP^{Si} = \sigma(t,z)\left(\frac{Si}{K\mu + Si}\frac{Si}{Ks + Si} Phy_1\ r_1^{Si}\right) \tag{4.5}$$

where σ is the algal growth controlled by light (I) and temperature (T) at time t and depth z (Clementson et al., 1998):

$$\sigma(t, z) = V(T)\,(1 - exp(-\frac{\alpha I(t,z)}{V(T)})) \tag{4.6}$$

where $V(T)=0.6(1.066)^T$, (Eppley, 1972) and α the initial slope of the *P-I* curve. Light intensity at depth is given

$$I(t,z)=PAR\ I(t,0)\exp(-(k_w+k_c P_0)z) \tag{4.7}$$

where PAR is the photosynthetically active fraction of total insolation, and k_w and k_c are the light attenuation constants for water and phytoplankton. The solar insolation, $I(t,0)$ was obtained from NCEP data (Kalnay et al., 1996).

In equations 4.3–4.5, $\frac{Si}{K\mu+Si}$ and $\frac{P}{Kp+P}$ are the nutrient limiting factor controlling the growth rate of diatoms and non-diatoms, respectively, with $K\mu$ and Kp the half saturation constants. In equation 4.4, $\frac{Fe}{Kf+Fe}$ represents iron limitation. No iron limitation has been taken to affect the non-diatoms, because observations suggest their response to iron is very small in comparison to diatoms (e.g. Boyd et al., 1999). For the diatoms, iron is considered to affect only the nitrate uptake (see section 4.4.4.3). In equation 4.5, $\frac{Si}{Ks+Si}$ is the silicate limitation on the silicate uptake, with Ks the half saturation constant. For many diatom species, $K\mu$ is much smaller than Ks, and for most of the species, $K\mu$ ranges from 0.04 to 1 (Ragueneau et al., 2000). Thus, Michaelis-Menton terms in both Ks and $K\mu$ must be included in equation 4.5 in order to model silicate depletion and link it to phytoplankton growth. Phy_1 and Phy_2 are the biomass of diatoms and non-diatoms in units of P (phosphate), respectively (see Section 4.4.4.1). The r_i^X terms are scaling factors converting primary production (in P unit) to export production (in X unit), which will be determined by matching the nutrient depletion in the simulation to the observations (see Section 4.4.3). For non-diatoms, we assume that the uptake of nitrate and phosphate satisfies the Redfield ratio (N/P = 16) therefore $16r_2^P = r_2^N$. Parameters required are given in the Table 4.1.

Table 4.1. Parameters used by the biological model.

Parameter	Units	Value	Reference
α in ML	$(\mathrm{W\ m^{-2}\ d})^{-1}$	0.05	Parslow et al. (2001)
α in SCM	$(\mathrm{W\ m^{-2}\ d})^{-1}$	0.1	Parslow et al. (2001)
PAR		0.5	Clementson et al. (2001)
K	μM	0.1	Matear and Hirst (1999)
K_μ	μM	1.0	This study
K_c	$\mathrm{m^{-1}}$ $(\mu\mathrm{M\ P})^{-1}$	0.96	Matear (1995)
K_w	$\mathrm{m^{-1}}$	0.04	Matear (1995)
z_e	m	120	This study

4.4.3. The mass balance calculation

Based on two assumptions discussed above: $\overline{F}^N = 14.5\overline{F}^P$ and $16r_2^P = r_2^N$, we can re-write the equation 4.1 for P, N and Si as follows:

$$\frac{dP}{dt}=\frac{d}{dz}\left(Kz\frac{dP}{dz}\right)+\overline{F}^P\frac{\tau x(t)}{\overline{\tau x}}-Q_1r_1^P-Q_2r_2^P \tag{4.8}$$

$$\frac{dN}{dt}=\frac{d}{dz}\left(Kz\frac{dN}{dz}\right)+14.5\overline{F}^P\frac{\tau x(t)}{\overline{\tau x}}-\frac{Fe}{Kf+Fe}Q_1r_1^N-16Q_2r_2^P \tag{4.9}$$

$$\frac{dSi}{dt}=\frac{d}{dz}\left(Kz\frac{dSi}{dz}\right)+\overline{F}^{Si}\frac{\tau x(t)}{\overline{\tau x}}\frac{Si_y(t)}{\overline{Si}_y}-\frac{Si}{Ks+Si}Q_1r_1^{Si} \tag{4.10}$$

where

$$Q_1=\sigma(t,z)\left(\frac{Si}{K\mu+Si}Phy_1\right) \tag{4.11}$$

$$Q_2=\sigma(t,z)\left(\frac{P}{Kp+P}Phy_2\right) \tag{4.12}$$

Based on the observation that diatoms have much higher fraction of export production than the non-diatoms, due to their faster sinking rate (Boyd and Newton, 1999), we set $r_1^P=4r_2^P$. With this assumption, averaged fraction of export is ~0.8 and ~0.2 for the diatoms and non-diatoms respectively in this study. The *f*-ratio in community (ratio of export to total production) is ~0.65 in the spring and ~0.35 in the summer, and thus is consistent with the observations in the PFZ (Mengesha et al., 1998; Caillian et al., 1999). Without this assumption, the community *f*-ratio would be constant for the whole year, which is in disagreement with the observations. By replacing r_1^P with $4r_2^P$ in the 4.8, we only have five unknown variables ($\overline{F}^P$, $\overline{F}^{Si}$, r_2^P, r_1^N and r_1^{Si}) which need be solved.

In a steady state ocean, the annual consumption of nutrients by phytoplankton in the euphotic zone must balance the sum of the vertical resupply and the horizontal transfer of the nutrients. By closing the annual budget for phosphate and silicate in the euphotic zone and by comparing their seasonal depletion in the simulation to the observation, we iteratively find the solution for $\overline{F}^P$, $\overline{F}^{Si}$, r_2^P and r_1^{Si} in equations 4.8 and 4.10. The solution is unique because the relationship between the export and horizontal supply represents a de-coupled balance, with nutrients decreasing mainly in spring – summer through phytoplankton consumption (EP^X) but increasing in all seasons through horizontal supply (F^X). We also investigate the uniqueness of the solution by changing the initial start point. If we double the initial $\overline{F}^X$ and r_i^X we still obtain the same solution. Once the $\overline{F}^P$ and r_2^P are determined, the unknown r_1^N is determined by closing the annual nitrate budget. Hence, nitrate depletion is not tuned to match the observations, which allows us to identify the potential mechanisms required to reproduce the observed seasonal cycle of nitrate.

4.4.4. Parameterizations of the biological model

4.4.4.1. Prescription of the biomass of diatoms and non-diatoms

Total biomass in phosphate unit (P_o) is estimated from the monthly chlorophyll a (*chl a*) derived from the Sea-viewing Wide Field-of-view Sensor (SeaWiFS):

$$P_o = chl \frac{C}{chl} \frac{1}{12C:P} \tag{4.13}$$

where *C/chl* is the carbon to *chl a* ratio (set to 75, Arrigo et al., 1998) and C:P the ratio of carbon to phosphate (set to 90, based on our preliminary modeling study). We assume that *chl a* concentration is uniform within the mixed layer. To reflect the SCM, between the base of the mixed layer and base of the euphotic zone, we linearly increase *chl a* to 2.5Po at the middle of the layer then decreased linearly to P_o at the base of the euphotic zone.

Parslow et al. (2001), showed that in the mixed layer, diatoms dominate the phytoplankton composition in the early spring but are a minor component (~30%) in late summer while in the SCM diatoms always dominate with 70-80% in late summer. To satisfy the observations, we compute the diatoms in P units in the mixed layer as follows:

$$Phy_1 = 0.5\ P_0 \qquad \text{when MLD} > 100 \text{ m} \qquad (4.14)$$

$$Phy_1 = 0.7\ P_0 \qquad \text{when MLD} \leq 100 \text{ m and silicate} > \text{Ks} \qquad (4.15)$$

$$Phy_1 = 0.3\ P_0 \qquad \text{when MLD} \leq 100 \text{ m and silicate} \leq \text{Ks} \qquad (4.16)$$

Below the mixed layer, we set $Phy_1 = 0.75\ P_0$. In the euphotic zone, the biomass of non-diatoms is given as $Phy_2 = P_0 - Phy_1$. Our formulation ensures that diatoms dominate the phytoplankton population in the spring in the mixed layer and in all the seasons in the SCM.

4.4.4.2. Parameterization of the half saturation constant Ks

Pondaven et al. (2000) summarized the Ks values from published data which show large variation (3 to 30 mmol Si m^{-2}). Recent research indicated that Ks ranged from 4 to 50 mmol Si m^{-2} in the Southern Ocean (Franck et al., 2000; Quéguiner, 2001). To determine Ks in our region, we compared the simulated export production using different Ks (2, 3.6 and 6 mmol Si m^{-2}). Model simulations indicate that there is an early (October) and short peak in the export production with Ks = 6 mmol Si m^{-2}, while there is no clear peak, but generally high export production during October to December with Ks = 2 mmol Si m^{-2}. Comparison of our simulated Si export production to the sediment traps suggests that the Ks of 3.6 mmol Si m^{-2} is reasonable (Figure 4.10e). Hence, we choose Ks = 3.6 mmol Si m^{-2}, which has the same ratio (0.4) to the winter silicate concentration as what Pondaven et al. (2000) used in their modeling study.

4.4.4.3. Parameterization of nitrate uptake by the diatoms

The availability of iron may play an important role in nitrate assimilation rate because iron is essential in the enzymes for nitrate and nitrite reductase. Research has shown that Fe addition can significantly stimulate nitrate uptake in the PFZ (DeBaar et al., 1997; Franck et al., 2000). Therefore, we introduce the $\frac{Fe}{K_f+Fe}$ term in the nitrate uptake formulation for the diatoms, with K_f the half saturation constant for nitrate and nitrite reductase activity or nitrate uptake (it is different to the half saturation constant for iron uptake). We don't explicitly model Fe concentration because we don't yet have a clear picture of the seasonal cycle of Fe in the PFZ. However, we have some evidence that the dissolved Fe is 0.3 – 0.4 nM in the winter, < 0.1 nM in the summer (Sedwick, per. Comm.), and the half saturation constant for growth is 0.09 nM for the diatoms in the PFZ (Blain et al., 2001). Assuming that the seasonality of Fe depletion is similar to that of silicate in the euphotic zone, we estimate the Fe concentration from $Fe = 0.04\ Si$ throughout the upper water column. This gives a seasonal change of Fe concentration from 0.36 nM to 0.08 nM, which is comparable to the limited observations. With this assumption, the ratio of Si/N uptake in the diatoms is the ratio of $\frac{Si}{Ks+Si} / \frac{Fe}{K_f+Fe}$.

Parslow et al. (2001) reported that Si/N uptake ratio was ~1 in the mixed layer and ~0.5 in the SCM in March 1998 in this region. With the above formulations, it is impossible to reproduce the observed Si/N uptake ratio in the SCM. This suggests that our formulations may underestimate nitrate uptake below the mixed layer. While we can not fully investigate the iron issue due to the lack of data, the fact that iron addition rarely decreased the Si/N uptake ratio to 1:1 in the PFZ (Franck et al., 2000) suggests that iron availability can not solely produce the observed low ratio of Si/N uptake below the mixed layer.

Research has shown that the ratio of carbohydrate:protein in the diatoms can change their buoyancy and that these reserves are adequate to support dark nitrate uptake (Moore and Villareal, 1996; Richardson and Cullen, 1995). The change in the buoyancy would also lead to subsurface population maximum and decoupled nitrate uptake from other nutrient uptakes (Moore and Villareal, 1996). These features, including subsurface *chl a* maximum, decoupled nitrate uptake to carbon or silicate uptake and high nitrate uptake ratio in the SCM have been observed in this region (Parslow et al., 2001; Dehairs pers. comm. 2001). For example, nitrate uptake rate was as ~2.5 times as high at 110 m as that at 20 m in March 1998 (Dehairs pers. comm. 2001). The *chl a* data show that the biomass is also ~2.5

times at 110 m as that at 20 m (Parslow et al., 2001), suggesting that nitrate uptake per unit of phytoplankton is same both at 20 m and 110 m. When we apply this rate to the nitrate uptake in the diatoms below the mixed layer in our model, we find that there is a strong subsurface minimum in the nitrate/phosphate concentration which is inconsistent with observations (Figure 4.3). Hence, we replace this approach with a simple adaptation of the vertical migration for diatoms by modifying the light control term in the SCM (i.e. only below the mixed layer) as:

$$I(t,z) = PAR\ I(t,0)\exp(-(k_w + k_c P_0)h) \qquad (4.17)$$

where h is a depth which the diatoms can rise up (= z – 15 m). The buoyancy depth (15 m) is determined by ensuring that the model simulation can reproduce the observed subsurface minimum of nitrate/phosphate in the water column (Figure 4.3). While this formulation has uncertainties, it predicts <2 times nitrate uptake below the mixed layer relative to that in the mixed layer in March, which is slightly less than the observed 2.5 times.

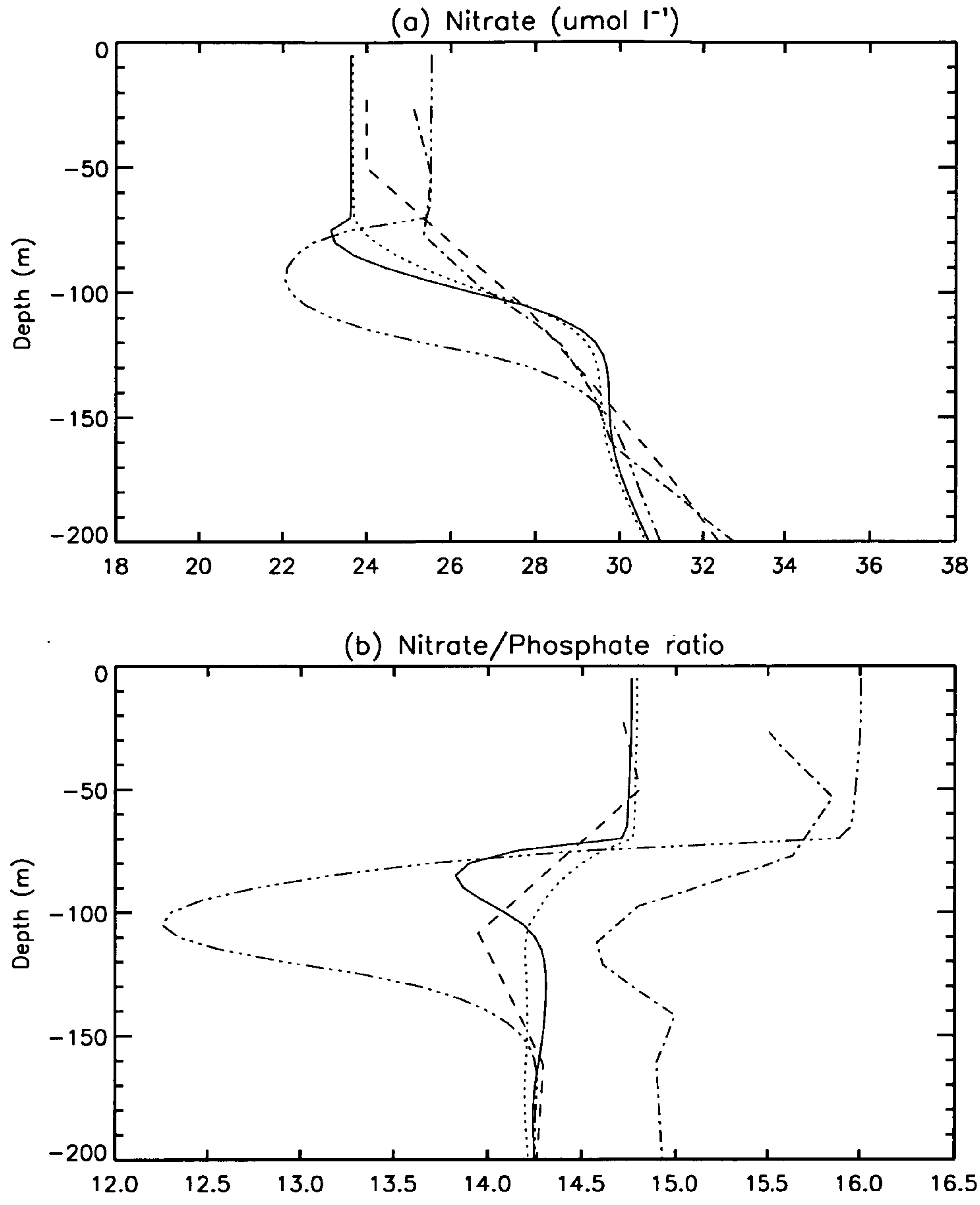

Figure 4.3. Profiles of (a) nitrate and (b) nitrate/phosphate ratio from AU 9309 (dashed line), AU9706 (dot-dashed line), model simulation with 15 m buoyancy (solid line), model simulation without buoyancy (dotted line), and model simulation with fixed nitrate uptake per unit of phytoplankton (dot-dot-dot-dashed line).

4.4.4.4. Parameterization of the remineralization of particulate organic matter (POM)

In our model, we assume that the export production (the EP^x term) is instantaneously remineralized below the euphotic zone (z_e). The fraction of remineralized nutrient decreases exponentially with depth (Williams and Follows, 1998):

$$P_r(z) = \exp^{-\frac{z-z_e}{z*}} \tag{4.18}$$

where z* is the scale length for remineralization. We first used the export production from preliminary model simulation (this study) and sediment trap data for nitrate and silicate (Trull et al., 2001b) (Table 4.2). Since there is no particulate organic phosphate (POP) data from the sediment traps in this region, the scale length for phosphate is set to the same as for nitrate in the initial run. The estimated export fraction (22%) of biogenic silica at 800 m (Trull et al., 2001b) seems too low, comparing with the value (27% at 1000 m) if we use the ^{234}Th derived bio-silica (1.4 mol) at 100 m and the sediment trap data at 1000 m (0.38 mol) in the PFZ (Nelson et al., 2001). A comparison study shows that the simulated silicate export production is ~5% higher using a scale length of 700 m relative to 450 m. But the scale length shows little influence on the ratios of Si/N and Si/P utilization. Therefore we choose the scale length of 450 m for silicate in our simulations.

Table 4.2. Estimates of the scale height for nitrate, phosphate and silicate

	Nitrate	Silicate
Depletion ($mmol/m^2$)	250	714
Export at 120 m ($mmol/m^2$)	604	1400
Particle at 800 m ($mmol/m^2$)	13.6	301
800 m/120 m (%)	2.2	22
1000 m/120 m (%)	0.8	14
Scale height (m)	180	450

4.4.5. Model set-up

The model set-up was described in detail by Wang and Matear (2001) and Wang et al. (2001). In brief, the model was forced with the surface fluxes of heat and fresh water and the wind stress from the NCEP (September 1997 – September 1998) and initialized with winter profiles of temperature and salinity from observations (AU9501). The initial profiles of nitrate, phosphate and silicate were extracted from Niskin bottle data from *Aurora Australis* cruise AU9501 (Rosenberg et al., 1997). The model domain was 0-1000 m, with a uniform vertical grid spacing of 5 m depth. The model bottom boundary was closed so that diffusive fluxes were not allowed across the model base. The test site is at 54°S 140°E in the PFZ.

4.5. Model experiments

We first perform an initial simulation using the above described model formulations and parameters and compare the simulated nutrient fields to observations. The observed seasonal nutrient cycle was compiled from bottle data from the *Aurora Australis and Southern Survey* cruises' during 1991 – 1998 period (see references in Griffiths et al., 1999; Lourey and Trull, 2001). We then carry out a series of sensitivity studies to identify other possible mechanisms capable reproducing the observed nutrient fields. In particular, we focus on the recycling of nitrate and phosphate, the potential role of DON/DOP ratio and iron limitation.

4.5.1. Initial simulation

Figure 4.4 presents the simulated phosphate, nitrate and silicate concentrations and nitrate/phosphate, silicate/nitrate and silicate/phosphate ratios in the mixed layer. The seasonal phosphate and silicate cycles and the silicate/nitrate and silicate/phosphate ratios are satisfied. But this simulation overestimates nitrate depletion in particular in March (Figure 4.4c), the simulated nitrate/phosphate ratio (14.3 – 14.9) is lower than the observation (14.5 – 15.5) during most of the growth season (Figure 4.4b).

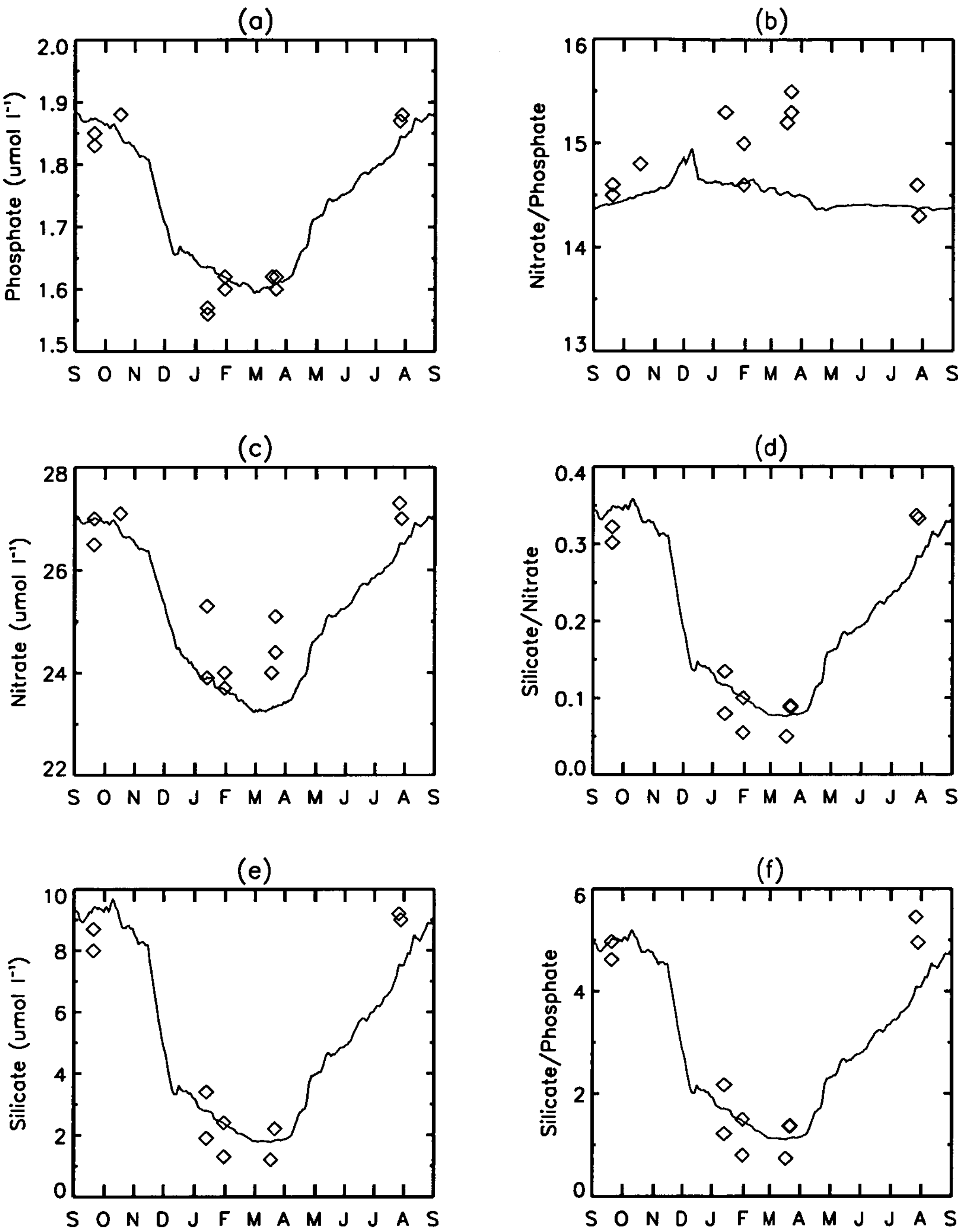

Figure 4.4. Daily concentration change for (a) phosphate, (c) nitrate, and (e) silicate, and ratio change for (b) nitrate/phosphate, (d) silicate/nitrate, and (f) silicate/phosphate in the surface waters from observations (◇) and initial simulation (solid lines).

Figure 4.5 presents the daily nutrient utilization ratios of the diatoms (left side) and of the community (right side). For the diatoms, the N/P utilization ratio ranges from 6 to 11 in the mixed layer. Below the mixed layer, the N/P utilization ratio (~25) is 2 – 3 times as high as that in the mixed layer during December – April (Figure 4.5a). The nutrient utilization ratios below the mixed layer for the period of May – November show large variations resulting from the MLD variability (not shown). For the community, the N/P utilization ratio is nearly constant (~12) in the mixed layer (Figure 4.5b). The Si/N utilization ratio reveals different features to the N/P utilization ratio. For the diatoms, the Si/N utilization ratio changes from ~4 in the spring to 2.5 in late summer in the mixed layer. Below the mixed layer, the Si/N utilization ratio decreases from 1.5 in the early summer to 1 in autumn. The seasonality of Si/N utilization ratio in our simulation is contrast to that expected from the seasonal iron depletion alone (see discussion below). For the community, there is no marked difference in the Si/N utilization ratio between the mixed layer and the deep water, which is high during September - December (~3), but low (~1) during January – April in the mixed layer. The simulated Si/N utilization ratio in March is in agreement with observation (~1) in the mixed layer, but much higher than observation (~0.5) below the mixed layer (Parslow et al., 2001).

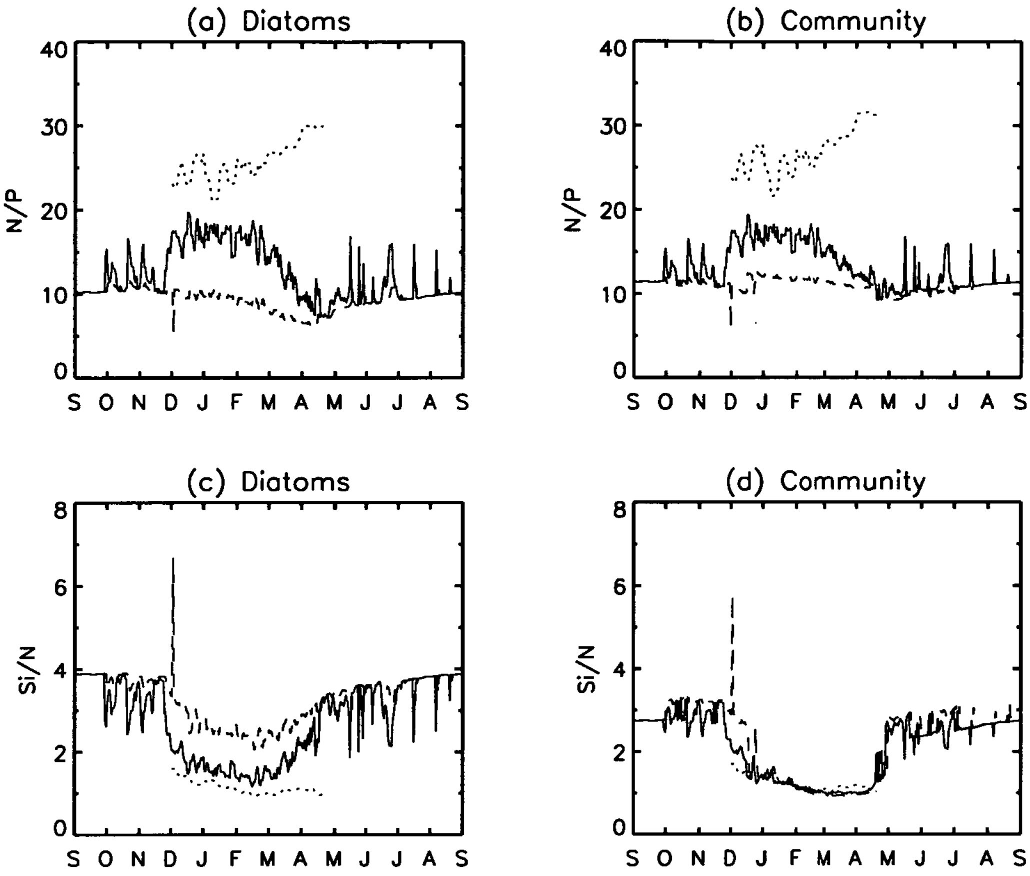

Figure 4.5. Simulated daily N/P utilization ratio of (a) diatoms and (b) community, and Si/N utilization ratio of (c) diatoms and (d) community in the mixed layer (dashed lines), below the mixed layer (dotted lines) and in 0-120 m water column (solid lines).

4.5.2. Sensitivity studies

The initial simulation indicates that in the mixed layer, the N/P utilization ratio is much lower than the Redfield ratio in either the diatoms or the community year-around. The Si/N utilization ratio varies between 1 and 4 in the diatoms and between 1 and 3 in the community. However, the initial simulation can not reproduce the observed seasonal nitrate depletion, nitrate/phosphate ratio in the mixed layer nor Si/N utilization ratio below the mixed layer. In the following sections, we investigate these two issues taking into account some of uncertainties in our formulations. Firstly, we examine if the model can reproduce the observed nutrient seasonality by having different remineralization length for phosphate and nitrate. Secondly, we investigate if the dissolved organic pool can significantly affect the simulated nutrient fields, in particular the DON/DOP ratio. Lastly, we test if the model can reproduce the observed Si/N utilization ratio using different value for the half saturation constant (K_f).

4.5.2.1. Remineralization of PON and POP

There is large uncertainty using modeled export production and deep sediment trap data to estimate the remineralization scale length. We can not determine the absolute values for nitrate and phosphate because of lack of information, but our intention is to determine which nutrient has a short remineralization length or preferential recycle. For simplicity, we set the scale length for phosphate constant (180 m). We perform two runs setting the remineralization length of nitrate to 125 m and 250 m.

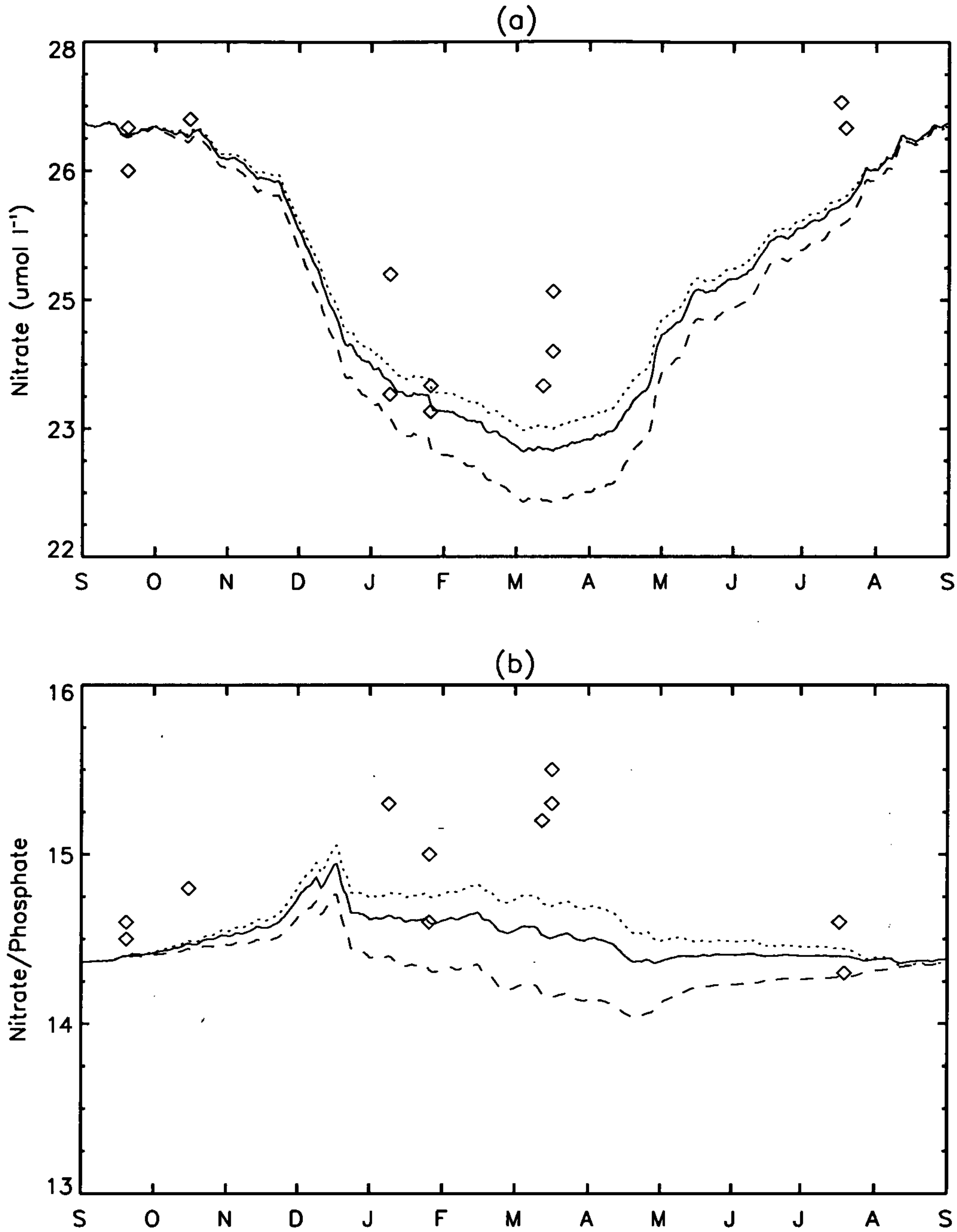

Figure 4.6. Seasonal change for (a) nitrate and (b) nitrate/phosphate ratio in the surface waters from simulations (initial run: solid lines, z*_pon=250: dotted lines, z*_pon=125: dashed lines) and from observations (◇).

Table 4.3. Nitrate and phosphate fluxes in relation to remineralization length during September – March (S-M) and March – September (M-S)

	Phosphate		Nitrate		Nitrate/Phosphate	
	S-M	M-S	S-M	M-S	S-M	M-S
Initial						
EP	49	16.9	720	203	14.7	12.0
Depletion	24	-23.2	364	-352	15.2	15.2
Res.-y	23.3	28.5	338	414	14.5	14.5
Res.-z	1.7	11.6	18	141	10.6	12.2
Res. total		40.1		555		13.8
*z*_pon =250*						
EP	50	17.1	697	198	13.9	11.6
Depletion	24.3	-23.5	342	-327	14.1	13.9
Res.-y	23.3	28.5	338	414	14.5	14.5
Res.-z	2.4	12.1	17	111	7.1	9.2
Res. total		40.6		525		12.9
*z*_pon =125*						
EP	50	17.1	784	217	15.7	12.7
Depletion	24.3	-23.5	418	-401	17.2	17.1
Res.-y	23.3	28.5	338	414	14.5	14.5
Res.-z	2.4	12.1	28	204	11.7	16.9
Res. total		40.6		618		15.2

$$\text{Depletion} = \int_{z}^{z-120} \int_{-a}^{t-b} \left[P(t,z) - P(a,z)\right] dt\, dz$$

Res.-y: horizontal transport.

Res.-z: vertical resupply.

Res. Total = Res.-y + Res.-z

Figure 4.6 shows the simulated nitrate concentration and nitrate/phosphate ratio in the mixed layer. The run with 125 m overestimates the nitrate depletion thus underestimates nitrate/phosphate concentration ratio. The run with 250 m slightly better performs than the initial run. Table 4.3 indicates that increasing scale length from 180 m to 250 m reduces nitrate resupply by 30 mmol m^{-2} through entrainment in autumn – winter, thus nitrate export production must decrease to meet the requirement of closing the annual budget. Because the nitrate depletion is mainly driven by export production in September – March, the reduced export production results in less depletion. Therefore the simulation with 250 m better performs than the initial (180 m) and 125 m simulations in reproducing the nitrate/phosphate depletion ratio. This suggests that below the euphotic zone, we should expect preferential recycling of phosphate.

4.5.2.2. DON/DOP ratio in the labile DOM pool

There is no measurement for DON and DOP in this region, but DOC data shows a seasonal change of 5 – 15 μM in 50 m mixed layer (Trull, unpublished 2001). Assuming a ratio of 100 for DOC/DOP ratio in the labile DOM pool, we estimate a maximum seasonal change of 0.15 μM DOP in the mixed layer. Based on observation, inorganic N pool other than nitrate (refer as other N), including ammonium (Watson, unpublished 2001), nitrite (Trull, unpublished, 2001) and urea (Dehairs, unpublished, 2001), accumulates ~75 mmol N m^{-2} in the euphotic zone in excess of that presents in the subsurface in March. Here we test two hypotheses: (1) ΔDON/ΔDOP ratio (e.g. $\frac{DON_{surface}-DON_{subsurface}}{DOP_{surface}-DOP_{subsurface}}$) = 6, (2) ΔDON/ΔDOP ratio = 16. In this experiment, ΔDON + other N and ΔDOP are accumulated consistently from September to February and then released as nitrate and phosphate consistently from March to August.

Table 4.4. Nitrate and phosphate fluxes and their ratios in relation to DON/DOP ratio during September – March (S-M) and March – September (M-S)

	Phosphate		Nitrate		Nitrate/Phosphate	
	S-M	M-S	S-M	M-S	S-M	M-S
ΔDON/ΔDOP=6						
EP	47.3	16.3	666	190	14.1	11.7
Depletion	25.2	-24.7	359	-349	14.2	14.1
Res.-y	18.8	23.0	273	334	14.5	14.5
Res.-z	3.3	10.5	34	85	10.3	11.4
DX*		7.5		120		16
Total**		41		539		13.1
ΔDON/ΔDOP=16						
EP	47.3	16.3	716	200	15.1	12.3
Depletion	25.2	-24.7	398	-391	15.8	15.8
Res.-y	18.8	23.0	273	334	14.5	14.5
Res.-z	3.3	10.5	45	62	13.6	5.9
DX		7.5		195		26
Total		41		591		14.4

*DX indicates DOP and DON+other N for phosphate and nitrate, respectively.

**Total = Res.-y + Res.-z + DX

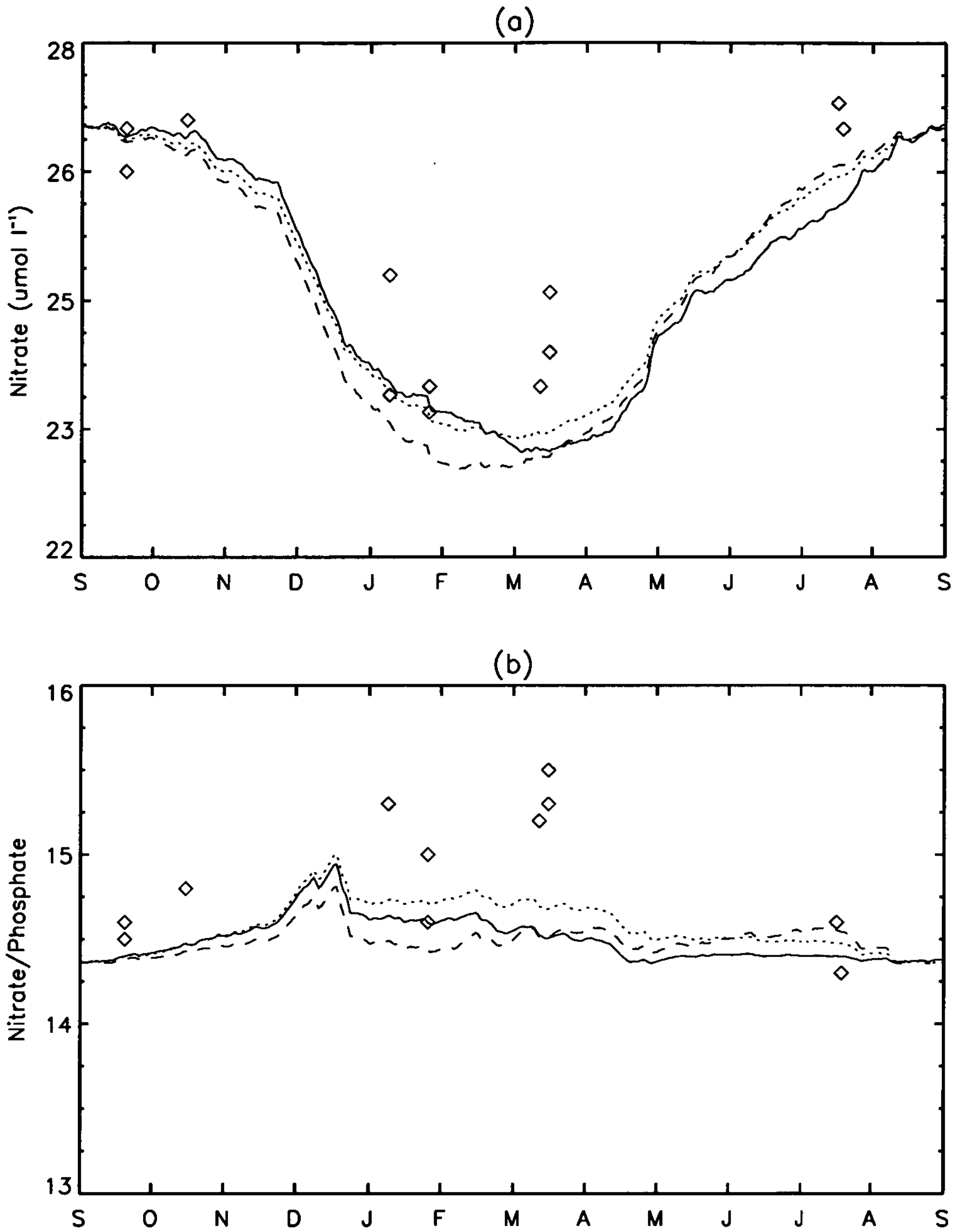

Figure 4.7. Seasonal change for (a) nitrate and (b) nitrate/phosphate ratio in the surface waters from simulations (initial run: solid lines, ΔDON/ΔDOP=6: dotted lines, ΔDON/ΔDOP=16: dashed lines) and from observations (◇).

Figure 4.7 shows that the run with low ΔDON/ΔDOP ratio of 6 performs better than the initial simulation but the run with high ΔDON/ΔDOP ratio does not. Table 4.4 indicates that during the period of March – September, increasing ΔDON/ΔDOP ratio from 6 to 16 increases the conversion of DON to nitrate by 75 mmol N m^{-2}, but only decreases the vertical resupply by 23 mmol N m^{-2}. Hence after the growth season, total production of nitrate is higher (591 mmol N m^{-2}) with ΔDON/ΔDOP = 16 relative to that with ΔDON/ΔDOP = 6. The high production of nitrate after the growth season reflects high export production in the growth season. This experiment suggests that the dissolved organic pool accumulates DON and DOP in proportions much lower than the Redfield ratio and this pool is important to balance the budget.

4.5.2.3. Iron limitation

While there is evidence that iron addition can stimulate nitrate uptake, there is little information available on the relationship of nitrate uptake rate and iron availability. We apply the growth formulation to this relationship and we use the half saturation constant for diatoms growth (0.09, Blain et al., 2001) for the K_f value in our initial simulation. As summarized by Blain et al. (2001), there are large variations in the half saturation constant for the growth. Here we explore the sensitivity of our model simulation to the chosen K_f value.

The model produces similar nitrate depletion in the mixed layer regardless what K_f value we use. Figure 4.8 shows that a high K_f of 0.4 produces slightly lower Si/N utilization ratio below the mixed layer (0.8 in March) relative to that in the mixed

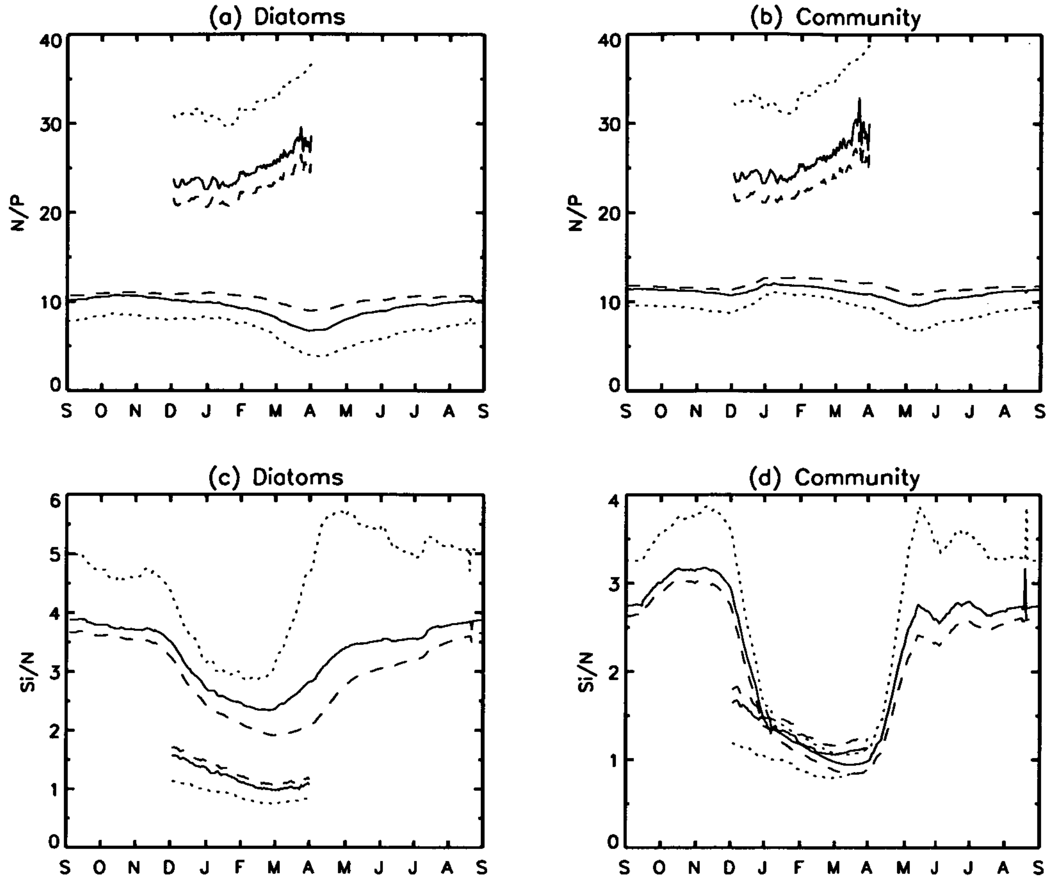

Figure 4.8. Monthly N/P utilization ratio in the mixed layer (long lines) and below the mixed layer (short lines) in (a) diatoms and (b) community and Si/N utilization ratio in (c) diatoms and (d) community from initial simulation (solid lines), simulation with large K_f (0.4 μM, dotted lines) and simulation with small K_f (0.03 μM, dashed lines).

layer (1.2). There is only one measurement which was carried out in March, showing that Si/N uptake ratio is ~1 at 20 m and ~0.5 at 110 m in the community (*Parslow et al.*, 2001). Hence, it is difficult to assess the simulated seasonal change and vertical profile of Si/N utilization ratio. Nevertheless, the seasonality of nitrate in model simulation is insensitive to the chosen K_f value.

4.5.2.4. Combination of preferential recycling of phosphate and low ΔDON/ΔDOP

The sensitivity tests show that it improves the agreement between the simulation and observation when the dissolved organic pool has a lower DON/DOP accumulation ratio than the Redfield ratio in the euphotic zone, and when there is preferential recycling of POP to phosphate below the euphotic zone. However, neither of the runs could successfully reproduce the seasonal nitrate depletion nor nitrate/phosphate ratio in the MLD. Here we combine both the DOM and POM behavior to examine if the model can reproduce the observed seasonal nitrate depletion. In this experiment, we set ΔDON/ΔDOP ratio to 5. We perform two runs: (1) z*_pon = 180, z*_pop = 125 (refer as Final1) and (2) z*_pon = 250, z*_pop = 180 (refer as Final2), and compare them to the initial run (z*_pon = 180, z*_pop = 180). These two formulations (Final1 and Final2) produce more reasonable seasonal nitrate and nitrate/phosphate ratio relative to the initial run (Figure 4.9) although they still overestimate nitrate depletion. Simulation can be improved if smaller ΔDON/ΔDOP ratio and larger difference between z*_pon and z*_pop are used relative to Final1 or Final2. More realistic simulation of DOM may also improve the agreement between the simulation and the observation in nitrate cycle because the seasonality of DOM breakdown affects the calculation of nitrate budget.

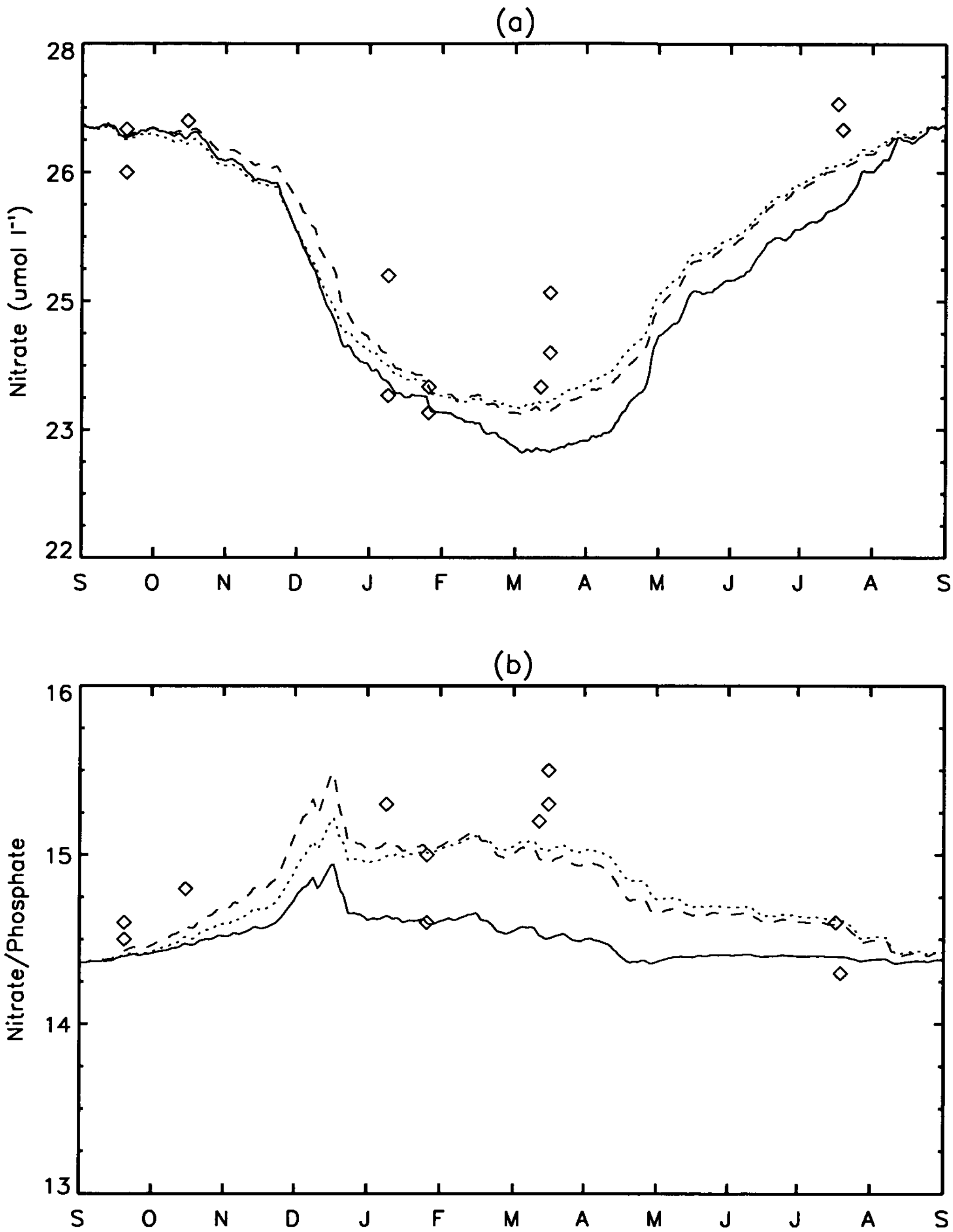

Figure 4.9. Seasonal change for (a) nitrate and (b) nitrate/phosphate ratio in the surface waters from observations (◇) and simulations (initial run: solid lines, Final1: dotted lines, Final2: dashed lines).

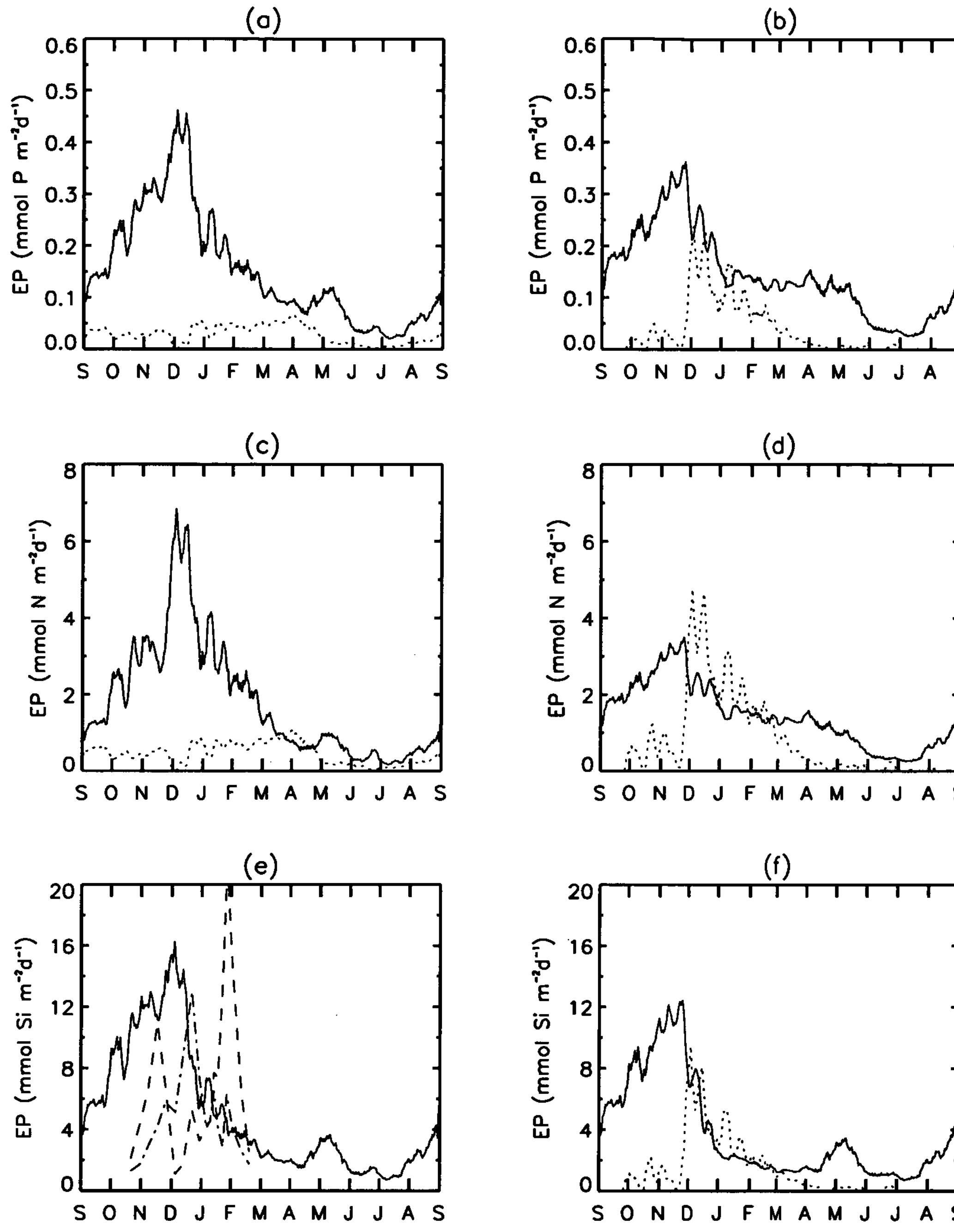

Figure 4.10. Simulated weekly export production for (a) phosphate in diatoms (solid line) and non-diatoms (dotted line), (b) phosphate in community (solid line: in the mixed layer; dotted line: below the mixed layer), (c) nitrate in diatoms (solid line) and non-diatoms (dotted line), (d) nitrate in community, (e) silicate in diatoms (solid line), sediment-trap collected at 800 m (dashed line) and at 1500 m (dash-lotted line), and (f) silicate in community. Line patterns in (d) and (f) are the same as in (b).

Figure 4.10 presents the seasonal export production in the diatoms and non-diatoms (left side) and community export production (right side) in the mixed layer and below the mixed layer. There is a strong seasonal pattern for the export production in the diatoms with the peak in early December, which results from high light intensity and high Si concentration (>K_s) in the mixed layer. The simulated silicate export production remains high for about 120 days (October – late December), which is roughly similar to the period of high biogenic silica collections found in the 800 m sediment trap, although those observations suggest two peaks of export rather than a single broad peak as in the model (Figure 4.10e). It is difficult to further assess temporal and amplitude differences between the modeled EP (at 120 m) and the deep sediment collection (at 800 m) because remineralization, differential settling of different components of the export flux, and ocean circulation can significantly alter the magnitude of sedimentation. Interestingly, there are similar time lags between the onset of the simulated high export production in the model and the first peak of biogenic silica at 800 m, and between the first peaks of biogenic silica at 800 m and at 1500 m from the sediment trap collections (Figure 4.10e). This may suggest that the diatoms' sinking rate is constant below the euphotic zone.

The seasonality of the export production in the non-diatoms is different, slightly increasing from spring to summer, reflecting a shift from the diatoms to non-diatoms in the phytoplankton community. The community export production in the mixed layer contributes more than 50% of the water column export production for most of the year. The exception is that during December – February, the export production below the mixed layer counts at least 50% for the nitrate and silicate export production. This is in agreement with the observation that the production in the SCM is ~50% of the total production in early summer (Parslow et al., 2001).

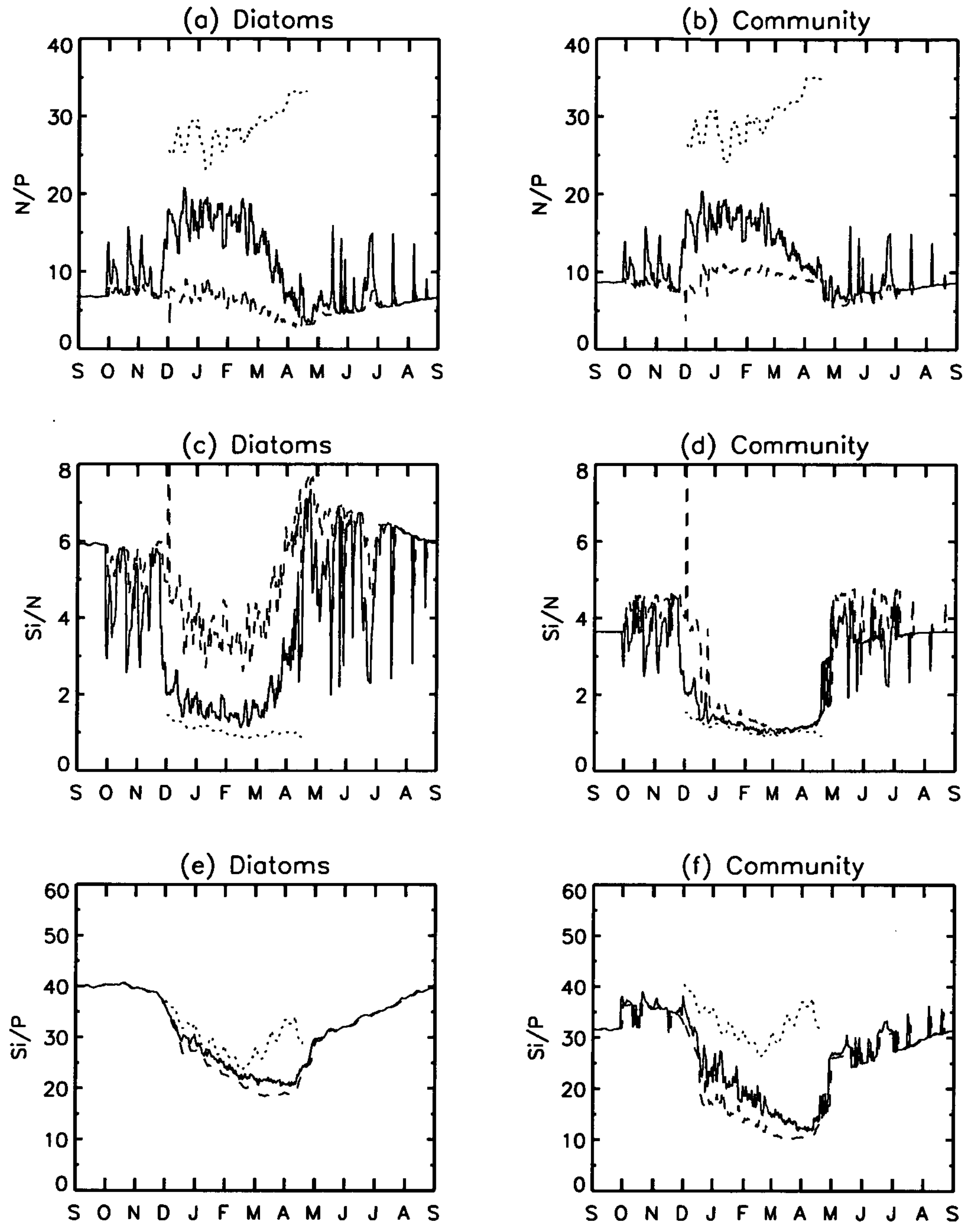

Figure 4.11. Simulated daily nutrient utilization ratio in the mixed layer (dashed lines), below the mixed layer (dotted lines) and in 0-120 m water column (solid lines) in (a) N/P ratio in diatoms, and (b) N/P ratio in community, (c) Si/N ratio in diatoms, (d) Si/N ratio in community, (e) Si/P ratio in diatoms, and (f) Si/P ratio in community.

Figure 4.11 presents the daily nutrient utilization ratios in the diatoms (left side) and in the community (right side). For the diatoms, the N/P utilization ratio is ranging 3 – 8 in the mixed layer and 25 – 30 below the mixed layer during December – April (Figure 4.11a). We don't present the nutrient utilization ratios below the mixed layer for the period of May – November due to large variations. For the community, the N/P utilization ratio is nearly constant (~9) in the mixed layer except in late November when there is a very short period with a low N/P utilization ratio (~4, Figure 4.11b). Such low nitrate/phosphate utilization ratio is similar to the nitrate/phosphate depletion ratios observed in diatom dominated waters (Arrigo et al., 2000; De Baar et al., 1997). The Si/N utilization ratio reveals strong seasonality. For the diatoms, the Si/N utilization ratio changes from ~6 in the spring to 3 in late summer in the mixed layer. Below the mixed layer, the Si/N utilization ratio decreases from 1.5 in the early summer to 1 in autumn. For the community, there is no pronounced difference in the Si/N utilization ratio between in the mixed layer and below the mixed layer. The mixed layer Si/N utilization ratio is high during September - December (~4), but low (~1) during January – April in the mixed layer. There is less variability in the Si/P utilization ratio in the diatoms, with a clear seasonal pattern of high (40) in the winter and low (20) in the late summer in the mixed layer (Figure 4.11e).

4.6. Discussion and conclusion

In this study, we used a bio-physical model to investigate the potential mechanisms contributing to the observed low nitrate/phosphate depletion ratio in the diatom dominated PFZ. We applied the Redfield ratio to the N/P utilization ratio of the non-diatoms. We determined the seasonal N/P/Si utilization ratios of the diatoms in a steady state ocean. We used estimates of phytoplankton biomass from the SeaWiFS to determine production, and tuned the model to reproduce the observed seasonal cycles of phosphate and silicate. For nitrate simulations, we set the horizontal transport to be constant to that of phosphate, and we carried out a series of experiments to identify the possible mechanism required to reproduce the observed seasonal cycle.

Our study demonstrates that there are three mechanisms responsible for the low nitrate/phosphate depletion ratio in observations: (1) the preferential recycling of phosphate below the euphotic zone, (2) the low ΔDON/ΔDOP ratio in the euphotic zone, and (3) the low N/P utilization ratio in the diatoms. Model simulations indicate that the nitrate/phosphate depletion ratio is ~14 with either of these mechanisms (Tables 4.3 and 4.4). Combination of these three will produce a nitrate/phosphate depletion ratio of ~12, which is close to the observed nitrate/phosphate depletion ratio.

4.6.1. The POM and DOM

There have been studies showing that organic P is preferentially remineralized over organic N (Clark et al., 1998; Benitez-Nelson and Buesseler, 1999; Loh and Bauer, 2000). The preferential recycling of P may be explained by the difference in the N/P requirement between the phytoplankton and zooplankton. As discussed by Arrigo et al. (2000), the mean N/P ratio for marine macrozooplankton is ~27, whereas the N/P ratio in the phytoplankton is <16. Hence, grazing may be responsible for the preferential recycling of P. The preferential recycling of P between the euphotic zone and depth may explain the different N/P export ratio between the subsurface and deep waters. As widely observed in the Southern Ocean, the nitrate/phosphate depletion ratio or the N/P utilization ratio is lower than the Redfield ratio of 16 in the surface water (Jennings et al., 1984; Karl et al., 1991; DeBaar et al., 1997; Rubin et al., 1998; Arrigo et al., 2000; Sweeney et al., 2000; Lourey and Trull, 2001), but there is evidence that PON/POP ratio in the sinking material increases with depth in the diatom dominated region of the Southern Ocean (Nodder and Northcote, 2001).

While there are few measurements of DOP and the DON/DOP ratio in this region, one measured in the PFZ had a DON/DOP ratio of ~20 in the euphotic zone (54°S, 176°W) whereas the ΔDON/ΔDOP ratio was ~15 (Loh and Bauer, 2000). However, other researches showed a DOC/DON ratio that was higher than the Redfield ratio in this region (Ogawa et al., 1999) and in diatoms produced organic matter (Biddanda and Benner, 1997). These may suggest regional difference in the properties of the dissolved organic pool, but they may also suggest non-Redfield in the dissolve organic materials.

4.6.2. Nutrient utilization ratios

Our study suggests that the N/P utilization ratio is 11.5 – 12.9 in the diatoms and 12.1 – 13.6 in the community in the PFZ (Table 4.5). This is similar to the observed nitrate/phosphate uptake ratio (<13) in the spring in the Polar Frontal water along the 6°W meridian (De Baar et al., 1997) and to that in other part of the Southern Ocean (Takeda, 1998). Assuming C/P utilization ratio is close to the Redfield ratio of 106, our estimated C/N utilization ratio is ~9.5 in the spring and ~6.5 in the summer (Figure 4.11b). This is similar to the POC/PON ratio (9 – 10 in the spring and 6.8 in the summer) observed in this region (Lourey and Trull, 2001).

Table 4.5. Annual mean nutrient utilization (mmol m^{-2} y^{-1}) and ratios

Experiment	Phosphate	Nitrate	Silicate	N/P	Si/N
Diatoms					
ΔDON/ΔDOP=6	55	625	1826	11.5	2.9
z*_pon=250 m	56	729	1826	12.9	2.5
Final1	52	602	1826	11.6	3.0
Final2	55	656	1826	11.8	2.8
Community					
ΔDON/ΔDOP=6	65	787	1826	12.1	2.3
z*_pon=250 m	66	897	1826	13.6	2.0
Final1	62	756	1826	12.2	2.4
Final2	66	831	1826	12.6	2.2

In the mixed layer, the Si/N utilization ratio is 3 – 6 in the diatoms and 1 – 4 in the community, with the lowest value simulated in the late summer (Figure 4.11c). The low Si/N utilization ratio in the summer results from the low silicate concentration. There is only one measurement of Si/N uptake ratio in this region (Parslow et al., 2001), which is in agreement with our simulation. We don't have observations to assess the seasonal Si/N utilization ratio in this region, but similar seasonal change of Si/N removal ratio has been observed in other part of the Southern Ocean (Smith and Asper, 2001). The simulated seasonality of the Si/N utilization ratio is contrast to that expected from the seasonality of iron concentration. This result suggests that the Si/N uptake ratio is not a function of iron availability only, but a combination of iron, silicate and nitrate availability. For example, an incubation study revealed a large range of Si/N uptake ratio (1 – 8) during spring – summer in the PFZ waters in the Pacific Sector (*Franck et al.*, 2000). Their highest ratio was found in the summer which may result from the higher silicate (5 μM) and lower nitrate (2.5 μM) relative to those at our site. However, our estimated Si/N utilization ratio in the diatoms is higher than the measured Si/N uptake ratio in diatoms (2.3 – 3) in incubation experiments under iron-deficit condition (Takeda, 1998; Hutchins and Bruland, 1998), which may reflect low availability of iron in the surface water year-around in this region, or possibly other influences such as light effects (see the recent review by Martin-Jezequel et al., 2001).

4.6.3. Export production

We estimate that the annual export production is ~65 mmol P m^{-2}, ~820 mmol N m^{-2} and 1826 mmol Si m^{-2} in the euphotic zone for phosphate, nitrate and silicate respectively (Table 4.5). The diatoms contribute 85% and 80% of the annual phosphate and nitrate export production. Our estimated Si export production is ~10 mmol $m^{-2}d^{-1}$ in the spring, which is similar to the predicted opal export production in the PFZ along 6°W using a complicated ecological model (Lancelot et al., 2000). The simulated silicate export production is ~2 mmol m^{-2} d^{-1} in March, which is ~80% of the biogenic silica total production measured by Quéguiner (2001). Our annual export production is comparable to the predicted 360 mmol N m^{-2} and 1100 mmol Si m^{-2} at 200 m at the Kerfix station of the Southern Ocean (Pondaven et al., 1997).

4.6.4. Mechanisms unable to explain the low nitrate/phosphate depletion ratio

There might be other explanations for the observed low nitrate/phosphate depletion ratio because any excess influx of nitrate to phosphate into the euphotic zone might cause low nitrate/phosphate depletion ratio. These may include enhanced recycling of organic N in to nitrate in the euphotic zone (De Baar et al., 1997), and high nitrate/phosphate ratio through horizontal transport. Though we do not explicitly model DON and DOP, our sensitivity test indicates that ΔDON/ΔDOP ratio should be much lower than the Redfield ratio. However, the bacterial activity was very low during that period in this region (Church et al., 2000), which may rule out the possibility of significant conversion of other N to nitrate.

Figure 4.2 shows that nitrate/phosphate concentration ratio has a weak seasonality, with ~14.5 in the winter and ~16 in the late summer in the PFZ. We set the nitrate/phosphate transport ratio to 14.5 in our model simulations, which may underestimate the horizontal supply of nitrate after the growth season. However, increasing nitrate supply requires more nitrate export to close the annual budget, which causes more nitrate depletion. Hence, the increase of nitrate/phosphate transport ratio from 14.5 to 16 will not be able to reproduce the nitrate concentration or nitrate/phosphate concentration ratio in the mixed layer.

In summary, this study demonstrate that the low nitrate/phosphate depletion ratio is not due to (1) the resupply through horizontal transport or vertical mixing, (2) the preferential recycling of nitrate below the euphotic zone, nor (3) the enhanced nitrate recycling in the euphotic zone. The low nitrate/phosphate depletion ratio is associated with the preferential recycling of phosphate below the euphotic zone, the low ΔDON/ΔDOP ratio in the euphotic zone, and the low N/P utilization ratio in the diatoms. The low N/P and high Si/N utilization ratio may reflect the low iron availability in the PFZ waters. Hence, more observations including the dissolved organic pool, remineralization and iron availability would offer a better understanding of the nutrient recycles in the Southern Ocean. A well-validated 3-D modelling approach would eventually offer a better understanding of horizontal nutrient supply. A more sophisticated ecosystem model that includes iron limitation and phytoplankton dynamics would provide better constrains on nutrient utilization ratios.

Chapter 5. General discussion and conclusion

The upper ocean dynamics is a key element studying oceanic carbon cycle. In particular, the vertical mixing plays an important role in determining the air-sea exchange of heat and other ocean properties. The vertical mixing processes are similar in both the SAZ and the PFZ in the summer when the ocean gains heat, the top layer becomes less dense and more stable. Under this stable condition, the heat influx tends to reduce the mixed layer depth while the influence of the wind deepens the mixed layer depth. Hence the wind mixing is the dominant process determining the MLD in the summer. The shallower summer MLD in the SAZ (~30 m) relative to that in the PFZ (~40 m) could be explained by the lower wind stress in the SAZ relative to that in the PFZ.

In the winter, the mechanism of the vertical mixing and the pattern of the MLD are very different between the SAZ and the PFZ. In the SAZ, cooling is the dominant process driving the timing of the deep winter mixed layer. Freshening plays an important role in determining the depth of the winter MLD, in particular in September – October period when the MLD is shoaling. The PFZ largely differs from the SAZ, showing little effect of the freshwater flux on the variability in the MLD. Wind stirring plays an important role in determining the MLD in the PFZ in both the winter and the summer. The maximum MLD is significantly shallower in the PFZ (160 m) than in the SAZ (600 m) although the winter wind stress is generally higher in the PFZ than in the SAZ. There are no signals of sharp deepening in the MLD in the winter or sudden shoaling in the spring in the PFZ, which is markedly different from the SAZ. The large difference in the winter mixed layer between the SAZ and the PFZ is not due to the difference in the surface forcing but to the stratification in the water column. The SAZ is weakly stratified but the PFZ is strongly stratified. There is a large density gradient (27.3 to 27.9) in the upper 1000 m of the PFZ in winter (Rintoul and Bullister, 1999), suggesting that there is little possibility to generate a deep mixed layer of 500 m in this region.

Apart from the differences in the vertical mixing and the MLD pattern, the PFZ is a region with pronounced horizontal transports, mainly the northward Ekman transport, due to the high wind stress and relative strong meridional gradients. However, the SAZ is a region showing a deep homogeneous layer with weak wind stress and weak meridional gradients in physical and biogeochemical properties.

Due to the different upper ocean dynamics, the biogeochemical processes are largely different between the two regions. For example, in the SAZ, a deep winter MLD (600 m) permits effective vertical supply of nutrient to the upper ocean during the winter. However, in the PFZ, the relatively strong stratification in the water below the mixed layer throughout the year produces much shallower winter MLD (160 m), so that most of the exported nutrient is remineralized below the winter MLD and can not be effectively resupplied to the upper ocean during the winter. The loss of nutrient from the upper ocean from the sinking of organic matter below the winter MLD must be balanced by horizontal resupply. Hence the shallower the winter MLD is, the greater the horizontal resupply is. In the SAZ, vertical mixing was the dominant mechanism for supplying nutrient (>80%) to the euphotic zone whereas in the PFZ, vertical mixing supplied only 37% of the nutrient to the euphotic zone and horizontal transport supplied the remaining 63%.

Associated with the large difference in the nutrient resupply, the two regions show pronounced difference in primary production and nutrient depletion. The SAZ has higher total production and larger nutrient depletion than the PFZ. However, the export production is higher in the PFZ (~65 mmol P m^{-2} y^{-1}) than in the SAZ (~55 mmol P m^{-2} y^{-1}) despite the PFZ having lower primary production and seasonal nutrient depletion. The lower nutrient depletion in the PFZ was due to its greater resupply of nutrient to the upper ocean through horizontal transport. Hence seasonal nutrient depletion was a better estimate of seasonal export production in the SAZ. The higher export production in the PFZ relative to that in the SAZ indicates that the SAZ is a region of stronger recycling of carbon and nutrients, whereas the PFZ is a region with higher export production. This conclusion is supported by the observations that mesopelagic Ba contents are higher in the PFZ than in the SAZ (Cardinal et al., 2001), which also suggests higher export in the PFZ than in the SAZ. While the lower nutrient depletion in the PFZ reflects greater horizontal transport, the high export production may reflect a greater proportion of large phytoplankton (diatoms).

While community structure is largely different between the two regions, with diatoms dominating in the PFZ but cocolithophores dominating in the SAZ, carbon and nutrient depletion ratios are also very different. In the SAZ, C/N/P depletion ratios are ~122/16/1, close to the Redfield ratio. But in the PFZ, C/N/P depletion ratios are much lower than the Redfield ratio (~90/9/1). The low carbon and nutrient depletion ratios in the PFZ may not be due to the resupply through horizontal transport or vertical mixing, but largely due to the low C/N/P utilization ratios in the diatoms.

There are three mechanisms responsible for the low nitrate/phosphate depletion ratios in observations in the PFZ: (1) the preferential recycle of phosphate below the euphotic zone, (2) the low ΔDON/ΔDOP ratio in the euphotic zone, and (3) the low N/P utilization ratio in the diatoms. The preferential recycle of P may be explained by the difference in the N/P requirement between the phytoplankton and zooplankton. As discussed by Arrigo et al. (2000), the mean N/P ratio for marine macrozooplankton is ~27, whereas the N/P ratio in the phytoplankton is <16. Hence, grazing may be responsible for the preferential recycle of P. The preferential recycle of P between the euphotic zone and depth may explain why the PON/POP ratio in the sinking material increases with depth in the diatom dominated region of the Southern Ocean (Nodder and Northcote, 2001).

While this study shows that the low ΔDON/ΔDOP ratio is associated with the low nitrate/phosphate depletion ratio, the labile DOM pool is relatively small (< 20% of the export production) in the PFZ. In addition, bacterial activity is low in later summer, which may rule out the possibility of large conversion of other form N to nitrate.

The N/P utilization ratio is much lower than the Redfield ratio in the PFZ, which is similar to the observed nitrate/phosphate uptake ratio (<13) in the spring in the Polar Frontal water along the 6°W meridian (De Baar et al., 1997) and to that in other part of the Southern Ocean (Takeda, 1998). The nitrate/phosphate export ratio is relatively low in the spring but high during the summer whereas the nitrate/phosphate utilization ratio shows no clear seasonality in the mixed layer. Therefore the observed nitrate/phosphate uptake or utilization ratio may not represent the export ratio at the base of the euphotic zone. This may partially explain the different N/P export ratio between the surface and deep waters in the observations.

The seasonal Si/N utilization appears in opposite to that of N/P utilization ratio, with the lowest value in the late summer. This seasonal pattern reflects the seasonality of Si availability. It is contrast to that expected from the seasonal iron availability and suggests that the Si/N utilization ratio is not only determined by the iron availability but also the silicate availability. However, the estimated Si/N utilization ratio in the diatoms is higher than the measured Si/N uptake ratio in diatoms (2.3 – 3) in incubation experiments under iron-deficit condition (Takeda, 1998; Hutchins and Bruland, 1998), which may reflect low availability of iron in the surface water year-around in the PFZ.

In summary, there are large differences in the physical and biogeochemical processes between the SAZ and the PFZ. One should take into account these differences for understanding the different role they playing in the oceanic carbon cycle. The relatively large carbon depletion in the SAZ may cause large amount of atmospheric CO influx to the ocean. However, this are-sea exchange should be much less pronounced in the PFZ due to its small carbon depletion. But in the PFZ, the fast sinking diatoms may more efficiently export the organic materials into deep ocean. Hence, future modeling studies should use a more sophisticated ecosystem model that includes phytoplankton dynamics to better understand the carbon and nutrient cycles in the Southern Ocean.

Appendix A

A1. Calculation of Ekman pumping

The rate of the Ekman pumping W depends on the curl of the surface wind stress:

$$W = \frac{1}{\rho f}\left(\frac{\partial \tau_y}{\partial x} - \frac{\partial \tau_x}{\partial y}\right) \tag{A1}$$

where ρ is the water density, f is the Coriolis parameter, and $\frac{\partial \tau_y}{\partial x} - \frac{\partial \tau_x}{\partial y}$ is the curl of the surface wind stress. Using the 4-year (1995-1998) averaged wind stress (Kalnay, 1996), the curl of the surface wind stress is ~8×10^{-8} and ~3×10^{-8} N/m^3 in the SAZ (46-48°S) and the PFZ (54-56°S), respectively. The rates of downwelling in the SAZ and upwelling in the PFZ are estimated as 21 and 10 m/y, respectively.

A2. Calculation of the averaged entrainment/detrainment rate

Averaged entrainment/detrainment rates are calculated using the data presented in Figures 2.4 and 2.5 for the SAZ and the PFZ, respectively:

$$\overline{W_e} = \frac{\sum_{i=2}^{n} \left| H_{ki} - H_{ki+1} \right|}{n-1} \tag{A2}$$

where H_{ki} is the Kraus depth (see 'Chapter 2' for further description) at day i, and n is the number of days to be averaged. The calculated averaged entrainment/detrainment rates are given in the following table.

Table. Mean entrainment/detrainment rate (m/d) in the SAZ and the PFZ.

	SAZ	PFZ
Sep.-Nov.	10	7.5
Dec.-Feb.	6	6
Annual mean	9	9.5

References

Anderson, S.P. and R.A. Weller, Surface buoyancy forcing and the mixed layer of the Western Pacific warm pool: Observation and 1D model results, *J. Climate, 9,* 3056-3085, 1996.

Arrigo, K.R., D. Worthen, A. Schnell, and M.P. Lizotte, Primary production in southern ocean waters, *J. Geophys. Res.-Oceans, (C8),* 15587-15600, 1998.

Arrigo, K.R., G.R. DiTullio, R.B. Dunbar, D.H. Robinson, M. VanWoert, D.L. Worthen, and M.P. Lizotte, Phytoplankton taxonomic variability in nutrient utilization and primary production in the Ross Sea, *J. Geophys. Res.-Oceans, 105(C4),* 8827-8845, 2000.

Bathmann, U.V., (Ed.), JGOFS Southern Ocean Regional Synthesis Report. JGOFS Report No. 31, XX pp. Bergen, Norway, 2000.

Benitez-Nelson, C.R. and K.O. Buesseler, Variability of inorganic and organic phosphorus turnover rates in the coastal ocean, *Nature, 398(6727),* 502-505, 1999.

Bi, D., Transient and long-term behaviour of the world ocean under global warming, Ph.D Thesis, 283 pp., University of Tasmania, Hobart, Australia, 2001.

Biddanda, B. and R. Benner, Carbon, nitrogen, and carbohydrate fluxes during the production of particulate and dissolved organic matter by marine phytoplankton, *Limnology & Oceanography, 42(3),* 506-518, 1997.

Blain, S., P.N. Sedwick, F.B. Griffiths, B. Quéguiner, E. Bucciarelli, M. Fiala, P. Pondaven, and P. Tréguer, Quantification of algal iron requirements in the Subantarctic Southern Ocean, *Deep-Sea Res. II,* Submitted, 2001.

Bopp, L., P. Monfray, O. Aumont, J.L. Dufresne, H. Le Treut, G. Madec, L. Terray, and J.C. Orr, Potential impact of climate change on marine export production, *Global Biogeochem. Cycles, 15(1),* 81-99, 2001.

Boyd, P., J. LaRoche, M. Gall, R. Frew, and R.M.L. McKay, Role of iron, light, and silicate in controlling algal biomass in subantarctic waters SE of New Zealand, *J. Geophys. Res.-Oceans, 104(C6),* 13395-13408, 1999.

Boyd, P.W., and P. Newton, Does planktonic community structure determine downward particulate organic carbon flux in different oceanic provinces? *Deep-Sea Res. I, 46*, 63-91, 1999.

Cailliau, C., S. Belviso, M. Goutx, A. Bedo, Y. Park, and E. Charriaud, Sedimentation pathways in the Indian sector of the Southern Ocean during a production regime dominated by regeneration, *Marine Ecology-Progress Series, 190,* 53-67, 1999.

Cardinal, D., F. Dehairs, T. Cattaldo, and L. André, Geochemistry of suspended particles in the Subantarctic and Polar Frontal Zones south of Australia: constraints on export and advection processes, *J. Geophys. Res.,* in press, 2001.

Chen, D., L.M. Rothstein, and A.J. Busalacchi, A hybrid vertical mixing scheme and its application to tropical ocean models, *J. Phys. Oceanogr., 24,* 2156-2179, 1994.

Church, M.J., D.A. Hutchins, and H.W. Ducklow, Limitation of bacterial growth by dissolved organic matter and iron in the Southern Ocean, *Applied & Environmental Microbiology, 66(2),* 455-466, 2000.

Clark, L.L., E.D. Ingall, and R. Benner, Marine phosphorus is selectively remineralized, *Nature, 393(6684),* 426, 1998.

Clementson, L.A., J.S. Parslow, A.R. Turnbull, D.C. McKenzie, and C.E. Rathbone, Parameters influencing the optical properties of the waters in the Australasian sector of the Southern Ocean, *J. Geophys. Res.*, in press, 2001.

Clementson, L.A., J.S. Parslow, F.B. Griffiths, V.D. Lyne, D.J. Mackey, G.P. Harris, D.C. McKenzie, P.I. Bonham, C.A. Rathbone, and S. Rintoul, Controls on phytoplankton production in the Australasian sector of the subtropical convergence, *Deep-Sea Research I, 45(10),* 1627-1661, 1998.

Davis, R.E., R. DeSzoeke, and P. Niiler, Variability in the upper ocean during MILE. Part II: Modeling the mixed layer response, *Deep-Sea Res., 28A*, 1453-1475, 1981.

Deardorff, J.W., A multi-limit mixed-layer entrainment formulation, *J. Phys. Oceanogr., 13,* 988-1002, 1983.

Debaar, H.J.W., Vanleeuwe, M.A., Scharek, R., Goeyens, L., Bakker, K.M.J., Fritsche, P., Nutrient anomalies in fragilariopsis kerguelensis blooms, iron deficiency and the nitrate/phosphate ratio (redfield,a.c.) of the antarctic ocean. *Deep-Sea Res. II* 44, 229-261, 1997.

Denman, K., E. Hofman, and H. Marchant. Marine biotic responses to environmental change and feedbacks to climate, in *Climate Change 1995*, edited by J.T. Houghton et al., pp. 483-517, Cambridge University Press, Cambridge, 1996.

Denman, K.L., and M.A. Peña, A coupled 1-D biological/physical model of the northeast subarctic Pacific Ocean with iron limitation. *Deep-Sea Res. II* 46, 2877-2908, 1999.

DiTullio, G.R., J.M. Grebmeier, K.R. Arrigo, M.P. Lizotte, D.H. Robinson, A. Leventer, J.B. Barry , M.L. VanWoert, and R.B.Dunbar, Rapid and early export of Phaeocystis antarctica blooms in the Ross Sea, Antarctica, *Nature, 404(6778),* 595-598, 2000.

Doney, S.C., A synoptic atmospheric surface forcing data set and physical upper ocean model for the U.S. JGOFS Bermuda Atlantic Time-Series Study site, *J. Geophys. Res., 101,* 25615-25634, 1996.

Doney, S.C., D.M. Glover, and R.G. Najjar, A new coupled, one-dimensional biological-physical model for the upper ocean - applications to the JGOFS Bermuda Atlantic time-series study (BATS) site, *Deep-Sea Res. II, 43(2-3),* 591-624, 1996.

Elskens, M., F. Dehairs, B. Griffiths and T. Cattaldo, N-uptake conditions during summer in the subantarctic and polar frontal zones in the Australian sector of the Southern Ocean, *J. Geophys. Res.,* in press, 2001.

Eppley, R.W., Temperature and phytoplankton growth in the sea, *Fish. Bull. U.S., 70,* 1063-1085, 1972.

Franck, V.M., M.A. Brzezinski, K.H. Coale, and D.M. Nelson, Iron and silicic acid concentrations regulate Si uptake north and south of the Polar Frontal Zone in the Pacific Sector of the Southern Ocean, *Deep-Sea Res. II, 47(15-16),* 3315-3338, 2000.

Gaspar, P., Y. Grégoris, and J. Lefevre, A simple eddy kinetic energy model for simulations of the oceanic vertical mixing: tests at Station Papa and long-term upper ocean study site, *J. Geophys. Res., 95,* 16179-16193, 1990.

Geider, R.J. and J. La Roche, The role of iron in phytoplankton photosynthesis and the potential for iron-limitation of primary productivity in the sea. *Photosynthesis Research,* 39, 275-301, 1994

Godfrey, J.S. and A. Schiller, Tests of mixed-layer schemes and surface boundary conditions in an ocean general circulation model, using the IMET flux data set, CSIRO MARINE LABORATORIES Report 231, 1997.

Griffiths, F.B., T.S. Bates, P.K. Quinn, L.A. Clementson, and J.S. Parslow, Oceanographic context of the First Aerosol Characterization Experiment (ACE 1): A physical, chemical, and biological overview, *J. Geophys. Res.-Atmospheres, 104(D17),* 21649-21671, 1999.

Häkkinen, S, Seasonal simulation of the southern ocean coupled ice-ocean system, *J. Geophys. Res., 100 (C11),* 22733-22748, 1995.

Hense, I., U.V. Bathmann, and R. Timmermann, Plankton dynamics in frontal systems of the Southern Ocean, *Journal of Marine Systems, 27(1-3),* 235-252, 2000.

Hoppema, M., E. Fahrbach, M. Schroder, A. Wisotzki, and H.J.W. Debaar, Winter-summer differences of carbon dioxide and oxygen in the Weddell Sea surface layer, *Marine Chemistry, (3),* 177-192, 1995.

Hoppema, M. and L. Goeyens, Redfield behaviour of carbon, nitrate and phosphate depletions in Antarctic surface water, *Limnol. Oceanogr., 44,* 220-224, 1999.

Hutchins, D.A. and K.W. Bruland, Iron-limited diatom growth and Si/N uptake ratios in a coastal upwelling regime, *Nature, 393(6685),* 561-564, 1998.

Ishii, M., H.Y. Inoue, H. Matsueda, and E. Tanoue, Close coupling between seasonal biological production and dynamics of dissolved inorganic carbon in the Indian Ocean sector and the western Pacific Ocean sector of the Antarctic ocean, *Deep-Sea Res. I, 45(7),* 1187-1209, 1998.

Jennings, J.C., L.I. Gordon, and D.M. Nelson, Nutrient depletion indicates high primary productivity in the Weddell Sea, *Nature 309* (May): 51-54, 1984.

Kalnay, E., et al., The NCEP/NCAR 40-year reanalysis project, *Bull. Amer. Meteorol. Soc. 77,* 437-471, 1996.

Kantha, L.H. and C.A. Clayson, An improved mixed layer model for geophysical applications, *J. Geophys. Res., 99,* 25235-25266, 1994.

Karl, D.M., B.D. Tilbrook, and G. Tien, Seasonal coupling of organic matter production and particle flux in the western Bransfield strait, Antarctica. *Deep-Sea Res. 38*, 1097-1126, 1991.

Kraus, E.B., and J.S. Turner, A one-dimensional model of the seasonal thermocline, II. The general theory and its consequences, *Tellus, 19,* 98-105, 1967.

Lancelot, C., E. Hannon, S. Becquevort, C. Veth, and H.J.W. De Baar, Modeling phytoplankton blooms and carbon export production in the Southern Ocean: dominant controls by light and iron in the Atlantic sector in Austral spring 1992, *Deep-Sea Research I, 47(9),* 1621-1662, 2000.

Large, W.G., J.C. McWilliams, and S.C. Doney, Oceanic vertical mixing: A review and a model with nonlocal boundary layer parameterization, *Rev. Geophys., 32,* 363-403, 1994.

Loh, A.N., and J.E. Bauer, Distribution, partitioning and fluxes of dissolved and particulate organic C, N and P in the eastern North Pacific and Southern Oceans, *Deep Sea Res. Part I, 47*, 2287-2316, 2000.

Louanchi, F., N. Metzl, and A. Poisson, Modelling the monthly sea surface fCO_2 fields in the Indian Ocean, *Marine Chemistry, 55(3-4),* 265-279, 1996.

Louanchi, F., M. Hoppema, D.C.E. Bakker, A. Poisson, M.H.C. Stoll, H.J.W. De

Baar, S. Schauer, D.P. Ruiz-Pino, and D. Wolf-Gladrow, Modelled and observed sea surface fCO_2 in the Southern Ocean: a comparative study, *Tellus, 51(2),* 541-559, 1999.

Lourey, M., and T.W. Trull , Seasonal nutrient depletion and carbon export in the Sub-Antarctic and Polar Frontal Zones of the Southern Ocean, South of Australia., *J. Geophys. Res.,* in press, 2001.

Markus, T., Results from an ECMWF-SSM/I forced mixed layer model of the Southern Ocean, *J Geophys Res, 104(C7),* 15603-15620, 1999.

Martin, J.H., G.A. Knauer, D.M. Karl, and W.W. Broenkow. VERTEX: carbon cycling in the Northeast Pacific. *Deep-Sea Res. 34*, 267-285, 1987.

Martin, P.J., Simulation of the mixed layer at OWS November and Papa with several models, *J. Geophys. Res., 90,* 903-916, 1985.

Martin-Jezequel, V., M. Hildebrand, and M.A. Brzezinski, Silicon metabolism in diatoms: Implications for growth, *Journal of Phycology, 36* (5), 821-840, 2000.

Matear, R.J., Parameter optimization and analysis of ecosystem models using simulated annealing - a case study at Station P, *J. Marine Res., (4),* 571-607, 1995.

Matear, R.J. and A.C. Hirst, Climate change feedback on the future oceanic CO2 uptake, *Tellus, 51(3),* 722-733, 1999.

Mellor, G.L. and T. Yamada, Development of a turbulence closure model for geophysical fluid problems, *Rev. Geophys. Spac. Phys, 20,* 851-875, 1982.

Mengesha, S., F. Dehairs, M. Fiala, M. Elskens, and L. Goeyens, Seasonal variation of phytoplankton community structure and nitrogen uptake regime in the Indian sector of the Southern Ocean, *Polar Biology, (4),* 259-272, 1998.

Metzl, N., B. Tilbrook, and A. Poisson, The annual fCO_2 cycle and the air-sea CO_2 flux in the sub-Antarctic Ocean, *Tellus, 51B,* 849-861, 1999.

Moore, J.K. and T.A. Villareal, Buoyancy and growth characteristics of three positively buoyant marine diatoms, *Marine Ecology-Progress Series, 132(1-3),* 203-213, 1996.

Nelson, D.M. et al. Vertical budgets for organic carbon and biogenic silica in the Pacific Sector of the Southern Ocean, 1996-1998. *Deep-Sea-Research,* submitted, 2001.

Niiler, P.P. and E.B. Kraus, One-dimensional models of the upper ocean, in Modelling and prediction of the upper layers of the ocean, edited by E.B. Kraus, pp. 143-172, Pergamon Press, 1975.

Nodder, S.D. and L.C. Northcote, Episodic particulate fluxes at southern temperate mid-latitudes (42-45 degrees S) in the Subtropical Front region, east of New Zealand, *Deep-Sea Research I, 48(3),* 833-864, 2001.

Ogawa, H., R. Fukuda, and I. Koike, Vertical distributions of dissolved organic carbon and nitrogen in the Southern Ocean, *Deep-Sea Research I, 46(10),* 1809-1826, 1999.

Pacanowski, R.C. and S.G.H. Philander, Parameterisation of vertical mixing in numerical models of tropical oceans, *J. Phys. Oceanogr., 11*, 1443-1451, 1981.

Parslow, J.S., P.W. Boyd, S.R. Rintoul, and F.B. Griffiths, A persistent sub-surface Chlorophyll maximum in the Inter-Polar Frontal Zone south of Australia: Seasonal progression and implications for phytoplankton – light – nutrient interactions, *J. Geophys. Res.,* in press, 2001.

Paulson, C. A. and J. J. Simpson, Irradiance measurements in the upper ocean. *J Physical Oceanography* 7, 952-956, 1977.

Pickard, G.L. and W.J. Emery (Eds), Descriptive physical oceanography: An introduction, 5th ed., 320 pp., Pergamon Press, Sydney, 1990.

Poisson, A., N. Metzl, C. Brunet, B. Schauer, B. Brès, D. Ruiz-Pino, and F. Louanchi, Variability of sources and sinks of CO_2 in the Western Indian and Southern Oceans in the year 1991, *J. Geophys. Res., 98,* 22759-22778, 1993.

Pollard, R.T., P.B. Rhines and R.O.R.Y. Thompson, The deepening of the wind mixed layer, *J. Geophys. Fluid Dyn., 3,* 381-404, 1973.

Pondaven, P., D. Ruiz-Pino, J.N. Druon, C. Fravalo, and P. Treguer, Factors controlling silicon and nitrogen biogeochemical cycles in high nutrient, low chlorophyll systems (the Southern Ocean and the North Pacific): Comparison with a mesotrophic system (the North Atlantic), *Deep-Sea Research I, 46(11),* 1923-1968, 1999.

Pondaven, P., D. Ruiz-Pino, C. Fravalo, P. Treguer, and C. Jeandel, Interannual variability of Si and N cycles at the time-series station KERFIX between 1990 and 1995 - A 1-D modelling study, *Deep-Sea Research I, 47(2),* 223-257, 2000.

Pondaven, P., C. Fravalo, S. Blain, E. Bucciarelli, and P. Tréguer, Role of iron limitation on phytoplankton growth and pelagic dynamics: A model simulation at the KERFIX site (51°S, 68°E) in the Indian sector of the Southern Ocean, *Deep-Sea Res. II,* Submitted, 2001.

Price, J.F., R.A. Weller, and R. Pinkel, Diurnal cycling: Observations and models of the upper ocean response to diurnal heating, cooling, and wind mixing, *J. Geophys. Res., 91,* 8411-8427, 1986.

Priddle, J., I.L. Boyd, M.J. Whitehouse, E.J. Murphy, and J.P. Croxall, Estimates of Southern Ocean primary production - constraints from predator carbon demand and nutrient drawdown, *J. Marine Systems, 17(1-4),* 275-288, 1998.

Queguiner, Biogenic silicate production in the Australian sector of the Sub-Antarctic Zone of the Southern Ocean at the end of summer, *J. Geophys. Res.,* in press, 2001.

Ragueneau, O. et al., A review of the Si cycle in the modem ocean: recent progress and missing gaps in the application of biogenic opal as a paleoproductivity proxy. *Global & Planetary Change* 26: 317-365, 2000.

Ribbe, J., On wind-driven mid-latitude convection in ocean general circulation models, *Tellus, 51(4),* 517-525, 1999.

Richardson, T.L. and J.J. Cullen, Changes in buoyancy and chemical composition during growth of a coastal marine diatom - ecological and biogeochemical consequences, *Marine Ecology-Progress Series, 128(1-3),* 77-90, 1995.

Rintoul, S. R., S. Sokolov, and J. A. Church, A six year record of austral summer baroclinic transport variability of the Antarctic Circumpolar Current at 140E, derived from XBT and altimeter measurements. *J. Geophys. Res.*, *submitted*, 2001.

Rintoul, S.R. and J.L. Bullister, A late winter hydrographic section from Tasmania to Antarctica, *Deep-Sea Res., 46,* 1417-1454, 1999.

Rintoul, S.R. and T. Trull, Mixed layer properties of the Subantarctic and Polar Frontal Zones south of Australia. *J. Geophys. Res.,* in press, 2001.

Rosenberg, M., S. Bray, N. Bindoff, R. Rintoul, N. Johnson, S. Bell and P. Towler, Aurora Australis marine cruise AU9501, AU9604 and AU9601 – oceanographic field measurements and analysis, inter-cruise comparisons and data quality notes, *Research report 12,* Antarctic Cooperative Research Centre, Hobart, Australia, 150 pp., 1997.

Rubin, S.I., T. Takahashi, D.W. Chipman, and J.G. Goddard, Primary productivity and nutrient utilization ratios in the Pacific Sector of the Southern Ocean based on seasonal changes in seawater chemistry, *Deep-Sea Res. I, 45(8),* 1211-1234, 1998.

Sarmiento, J. L and E. T. Sundquist, Revised budget for the oceanic uptake of anthropogenic carbon dioxide. *Nature 356*, 589-593, 1992.

Sarmiento, J.L., and C. Le Quere, oceanic carbon dioxide uptake in a model of century-scale global warming, *Science, (5291),* 1346-1350, 1996.

Schlitzer, R., Carbon export fluxes in the Southern Ocean: results from inverse modeling and comparison with satellite based estimates, *Deep-Sea Res. II,* in press, 2001.

Schopf, P.S. and M.A. Cane, On equatorial dynamics, mixed layer physics and sea surface temperature, *J. Phys. Oceanogr., 13,* 917-935, 1983.

Sedwick, P.N., G.R. DiTullio, D.A. Hutchins, P.W. Boyd, F.B. Griffiths, A.C. Crosslet, T.W. Trull, and B. Quéguiner, Limitation of algal growth by iron deficiency in the Australian Subantarctic region, *Geophys. Res. Letters, 26*, 2865-2868, 1999.

Six, K.D., and E. Maier-Reimer, Effects of plankton dynamics on seasonal carbon fluxes in an ocean general circulation model, *Global Biogeochem. Cycles, 10(4),* 559-583, 1996.

Smith, W.O. and V.L. Asper, The influence of phytoplankton assemblage composition on biogeochemical characteristics and cycles in the southern Ross Sea, Antarctica, *Deep-Sea Research I, 48(1),* 137-161, 2001.

Sweeney, C., D.A. Hansell, C.A. Carlson, L.A. Codispoti, L.I. Gordon, J. Marra, F.J. Millero, W.O. Smith, and T. Takahashi, Biogeochemical regimes, net community production and carbon export in the Ross Sea, Antarctica, *Deep-Sea Res. II 47(15-16),* 3369-3394, 2000a.

Sweeney, C., W.O. Smith, B. Hales, R.R. Bidigare, C.A. Carlson, L.A. Codispoti, L.I. Gordon, D.A. Hansell, F.J. Millero, M.O. Park, and T. Takahashi, Nutrient and carbon removal ratios and fluxes in the Ross Sea, Antarctica, *Deep-Sea Res. II 47(15-16),* 3395-3421, 2000b.

Takahashi, T., R.A. Feely, R.F. Weiss, R.H. Wanninkhof, D.W. Chipman, S.C. Sutherland, and T.T. Takahashi, Global air-sea flux of CO_2 - an estimate based on measurements of sea-air pCO_2 difference, *Proceedings of the National Academy of Sciences of the United States of America, (16),* 8292-8299, 1997.

Takeda, S., Influence of iron availability on nutrient consumption ratio of diatoms in oceanic waters, *Nature, 393(6687),* 774-777, 1998.

Trull, T., S.R. Rintoul, M. Hadfield, and E.R. Abraham, Circulation and seasonal evolution of polar waters south of Australia: Implications for iron fertilization of the Southern Ocean. *Deep Sea Res., II, 48, 2439-2466,* 2001a.

Trull, T., S. Bray, S. Manganini, S. Honjo, and R. Francois, Moored sediment trap measurements of carbon export in the Sub-Antarctic and Polar Frontal Zones of the Southern Ocean, south of Australia. *J. Geophys. Res.,* in press, 2001b.

Wang, X. and R.J. Matear, Modeling the upper ocean dynamics in the Subantarctic and Polar Frontal Zones in the Australian sector of the Southern Ocean. *J. Geophys. Res.,* in press, 2001.

Wang, X., R.J. Matear and T.W. Trull, Modeling seasonal phosphate export and resupply in the Subantarctic and Polar Frontal Zones in the Australian sector of the Southern Ocean. *J. Geophys. Res.,* in press, 2001.

Williams, R.G., and M.J. Follows, The Ekman transfer of nutrients and maintenance of new production over the north Atlantic, *Deep-Sea Res. I, 45 (2-3),* 461-489, 1998.

Yu, E.F., R. Francois, M.P. Bacon, S. Honjo, A.P. Fleer, S.J. Manganini, M.M. Rutgers van der Loeff, and V. Lttekot, Trapping efficiency of bottom-tethered sediment traps estimated from the intercepted fluxes of ^{230}Th and ^{231}Pa. *Deep-Sea Res. I, 48(3),* 865-889, 2001.